Layered Lanthanide Coinage-Metal Diarsenides: Syntheses, Commensurately and Incommensurately Modulated Structures, Electric and Magnetic Properties

D I S S E R T A T I O N

zur Erlangung des akademischen Grades
Doctor rerum naturalium
(Dr. rer. nat.)

vorgelegt an der
Fakultät Mathematik und Naturwissenschaften
der Technischen Universität Dresden

von

Dipl. Ing. Dieter Rutzinger
geb. am 03.11.1976 in Salzburg

Gutachter: **Prof. M. Ruck, TU Dresden**
Prof. D. Johrendt, LMU München

Eingereicht am: **13.07.2009**
Tag der Verteidigung: **13.11.2009**

Lanthan, ein neues Metall.

Mosander*) hat gefunden, dafs das Cerium überall, wo es vorkommt, von einem neuen zuvor unbekannten Metall begleitet wird, dessen Oxyd dem Ceroxyd im Ansehen so ähnlich ist, dafs es schwerlich durch seine äufseren Eigenschaften von diesem unterschieden werden kann. Das Cerium verhält sich also, wie z. B. das Kobalt, welches fast niemals ohne Nickel gefunden wird, oder wie das Tellur, welches selten von Selen frei ist u. s. w. Mosander hat dies neue Metall zuerst in dem Cerit von Bastnäs gefunden und ihm den Namen *Lanthan*, von λανθανειν verborgen seyn, gegeben.

aus: *Justus Liebigs Annalen der Chemie und Pharmacie*
1839, *32(2)*, 235–237

1 Introduction and Aim of Work

Compounds with layered type structures, essentially compounds with two-dimensional square nets of main group elements, are subject of intensive investigations due to both interesting structural features and physical properties. Under these, binary and ternary compounds of the compositions MT_4, MT_2X_2, MTX_2, $MT_{1\pm\delta}X_2$ and MX_2 [1–8] have been investigated (M = alkaline, alkaline earth or rare-earth element, T = *d*-block element, X = element of groups 13 – 15).

These compounds contain PbO-like layers and, in the case of the compositions MTX_2, $MT_{1-\delta}X_2$ and MX_2, planar square nets of X atoms. In some compounds, these layers have been found to be symmetry breaking due to local Peierls-like distortions and the respective compounds crystallize in lower symmetric crystal systems compared to their aristotypes with undistorted layers. The high temperature superconductors found most recently (LaOFeP, $LaFeAsO_{1-x}F_x$ and its derivatives) exhibit related structures [9–19].

The magnetism of the lanthanide copper arsenides and antimonides is complex: The compounds described until now are mainly paramagnetic and follow a Curie-Weiss law. At low temperatures, antiferromagnetic ordering is observed for most compounds with Neél temperatures well below 20 K [8, 20-27]. For individual compounds deviations of this behavior such as a ferromagnetic ordering [8] at low temperature, a metamagnetic transition at low temperature in low fields [24], or an incommensurate magnetic structure near the phase transition temperature [23] have been reported.

The electrical resistivity of the $LnCu_{1+\delta}As_2$ compounds ($0 \leq \delta \leq 0.25$) with undistorted square nets of As atoms is intensively studied in literature [22, 25–28]. A metallic behavior is concluded since the resistance decreases monotonically with the temperature. Anomalies indicating a Kondo-like behavior near the magnetic transition temperatures are reported [22, 25–28].

The aim of the present work is to extend the crystal structure determinations to the $LnAgAs_2$ and $LnAuAs_2$ compounds. Although a remarkable number of these compounds can be found in literature, only few of the structures of the silver compounds were determined by single-crystal diffraction experiments, the other ones are based on powder data. The structures obtained by single-crystal diffraction data exhibit an orthorhombic distortion of the unit cell, which is caused by the formation of cis-trans or zigzag chains of the planar layer of As atoms. From an electronic point of view (cf. level of knowledge, chapter 2), all $LnTAs_2$ compounds

should be prone to a distortion of the square nets of As atoms. Most of these compounds based on powder diffraction measurements exhibit immense thermal displacement parameters of the As atoms in the square net, which may be taken as a hint for a structural distortion, too. Since only small shifts of some atoms from the ideal positions may occur, single-crystal structure determinations are essential to verify a possible distortion. Especially the gold compounds and $LaAgAs_2$, described in the average structure of the aristotype, are based on powder diffraction data, only.

For the $LnCu_{1+\delta}As_2$ (*Ln* = La, Ce – Nd, Sm), non-stoichiometry ($0.05 \leq \delta \leq 0.25$) has been reported recently [8, 29]. It should therefore be checked, whether or not the non-stoichiometry persists over the whole series of coinage metals and, if so, how δ changes with *Ln* and *T*.

Furthermore, the investigation of physical properties such as magnetization and resistivity measurements of selected compounds should be carried out. In the case of undistorted layers of As atoms, metallic conductivity is expected. whereas distorted layers may be semiconductors. Band structure calculations are scheduled to accompany the experimental outcome.

2 Level of Knowledge

A considerable number of the MT_2X_2, MTX_2, $MT_{1\pm\delta}X_2$ and MX_2 compounds can be traced back to the $BaAl_4$ type (space group $I4/mmm$ (No. 139 [30]), a = 4.539(3) Å, c = 11.160(3) Å [31]), which contains PbO-like layers consisting of two crystallographically independent Al atoms, Al1 and Al2 (figure 2.1), and Ba atoms in the voids between these layers. Substitution of the Al atoms leads to a broad variety of compounds.

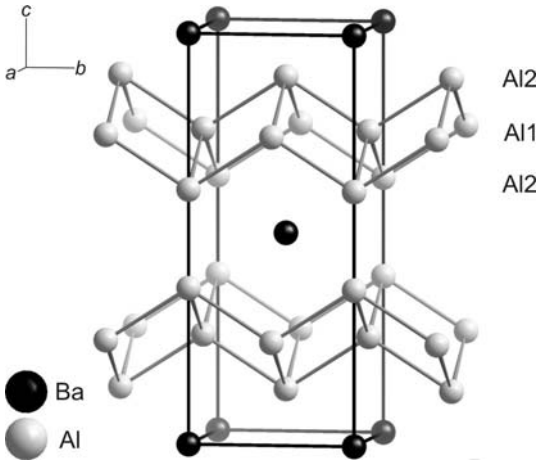

Figure 2.1: Structure of $BaAl_4$.

The ternary compounds MT_2X_2 are derived by substituting the Al1 atoms with T atoms and the Ba atoms with X atoms. These compounds crystallize in the so called $ThCr_2Si_2$ type (space group $I4/mmm$, a = 4.043(1) Å, c = 10.577(2) Å, figure 2.2 left) [32]. Substituting one half of the Al1 and Al2 atoms with T atoms and the other ones with X atoms, the $CaBe_2Ge_2$ type (space group $P4/nmm$ (No. 129), a = 4.020(2) Å, c = 9.920(2) Å, figure 2.2 right, [2, 4]) is derived.

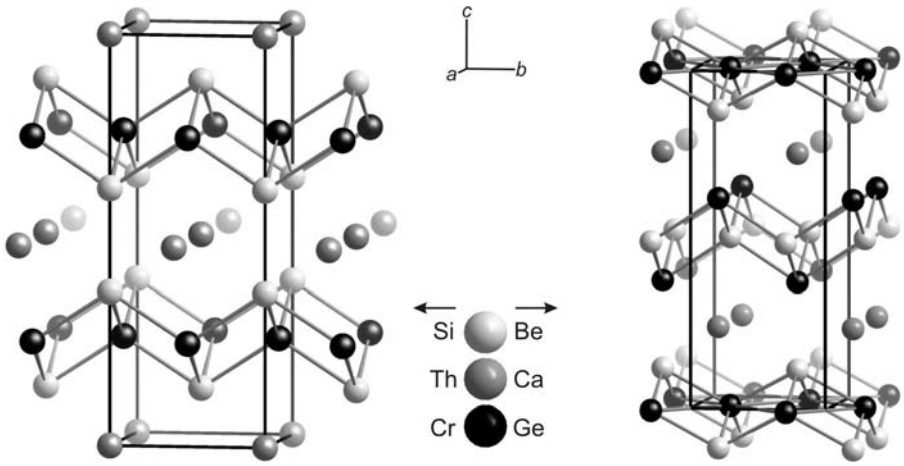

Figure 2.2: Structure of $ThCr_2Si_2$ (left) and $CaBe_2Ge_2$ (right).

Random removal of some of the *T* atoms leads to the defect structure $MT_{2-x}X_2$, which is commonly referred to as $MT_{1+\delta}X_2$ (figure 2.3 left) since *x* is usually 0.90±0.05. Smaller spheres were chosen to emphasize the fractional occupation of the *T* atoms in the figure. According to its formula, this type can also be denominated as a stuffed variant of the $HfCuSi_2$ type.

Removing one half of the *T* atoms results in the $HfCuSi_2$ type (space group *P*4/*nmm*, *a* = 3.732(1) Å, *c* = 8.99(2) Å, figure 2.3 right [33]), which is also referred to as $ZrCuSi_2$ or $CaMnBi_2$ type.

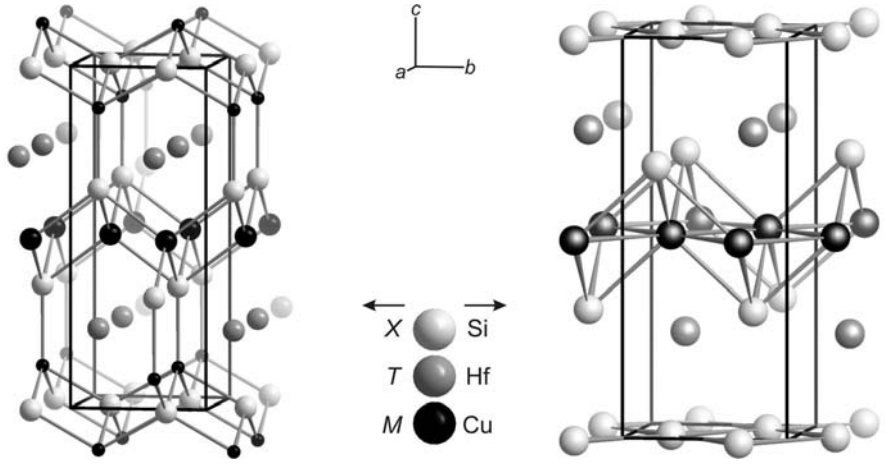

Figure 2.3: Structure of $MT_{1+\delta}X_2$ (left) and $HfCuSi_2$ (right).

Random removal of some more *T* atoms results in the defect structure $MT_{1-\delta}X_2$ (figure 2.4 left). Removing the residual *T* atoms, the PbFCl or ZrSSi type with the general composition MX_2 (space group *P*4/*nmm*, *a* ≈ 4 Å, *c* ≈ 8 Å, figure 2.4 right [31–36]) is derived. The latter one may be considered to be the aristotype of numerous binary polypnictides and polychalcogenides $MX_{2-\delta}$ ($0 \leq \delta \leq 0.5$).

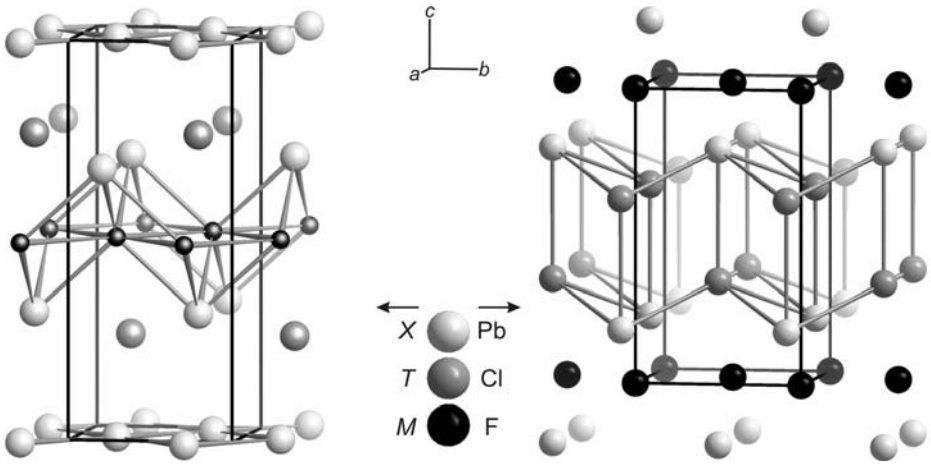

Figure 2.4: Structure of $MT_{1-\delta}X_2$ (left) and PbFCl (right).

Additionally to the compounds mentioned in the paragraphs above, several compounds have been found to crystallize in structures closely related to them: $SrZnBi_2$ (space group *I*4/*mmm*, $a = 4.64(1)$ Å, $c = 21.96(2)$ Å [37]) contains puckered double sheets consisting of Bi and Zn and planar 4^4-nets of Bi separated by Sr atoms in the voids of the PbO-like layer. This structure has been reported for $CeAg_{1.08}P_{1.9}$ [38], $LaAuAs_2$ [29], $LaCu_{1.23}As_2$ [8], $UCuP_2$ [39], and $CeCu_{1.09}P_{1.87}$ [40], too.

Numerous compounds of the general composition MTX_2 adopt the $HfCuSi_2$ type [8, 23, 33, 41–46] or one of its distorted variants [24, 29]. $HfCuSi_2$ crystallizes in the tetragonal space group *P*4/*nmm* (No. 129) [33] and contains eight atoms which occupy four twofold positions: Hf (*M*) on 2*c* (¼, ¼, *z*), Cu (*T*) on 2*b* (¼, ¾, ½), Si1 (*X*1) on 2*c* (¼, ¼, *z*) and Si2 (*X*2) on 2*a* (¼, ¾, 0). Characteristic features of the $HfCuSi_2$ structure are PbO-like layers formed by the *T* and *X*1 atoms and planar square nets of the *X*2 atoms. These motives are separated by *M* atoms, which are embedded in the voids of the PbO-like layer (figure 2.5). In the ternary lanthanide compounds $LnTAs_2$ the lanthanide atoms *Ln*, the coinage metal atoms *T* and arsenic atoms occupy the Hf, Cu and Si positions, respectively.

A similar structure is found in the recently published iron-based layered superconductors LaOFeP [9], $LaFeAsO_{1-x}F_x$ [10, 11] and its derivatives [12–19], which crystallize in the so called ZrCuSiAs structure type (space group *P*4/*nmm*, $a = 3.6736(2)$ Å, $c = 9.5712(9)$ Å) [47], which can be described as a stuffed PbFCl type (figure 2.5).

In this structure, Zr occupies the position of Hf, Cu those of Cu, Si those of Si2 and As those of the Si1 atoms of the $HfCuSi_2$ type, respectively. Contrary to the $HfCuSi_2$ type, Zr is shifted towards Si resulting in the formation of an additional PbO-like layer.

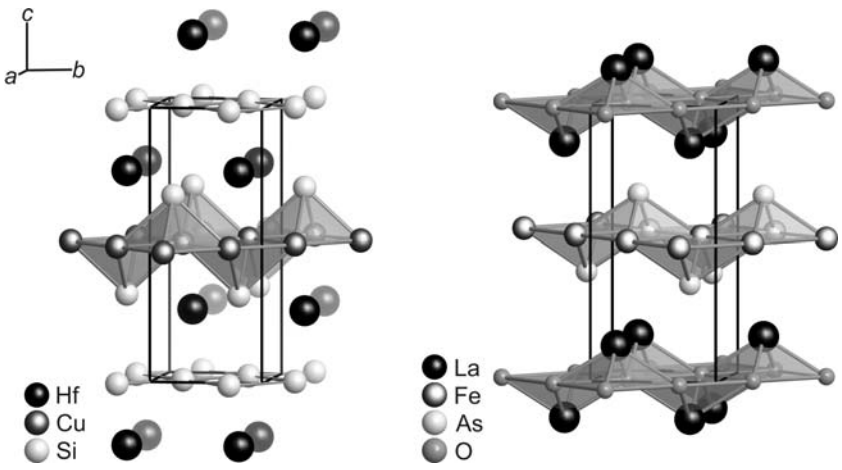

Figure 2.5: Structural relationship of the $HfCuSi_2$ type (left) and LaFeAsO (right, both in *P*4/*nmm*, No. 129).

Due to local Peierls-like distortions in the planar layers, these atoms have been found to be symmetry breaking and their positions cannot be described by tetragonal symmetry [21, 22, 24]. Consequently a reduction in symmetry is necessary.

The number of intra-arsenic bonds *b*(As–As) of the *LnT*As$_2$ compounds can be estimated according to the Zintl-Klemm principle with the valence electron concentration (*VEC*):

$$VEC(\mathrm{As}) = \frac{e(Ln) + e(T) + x \cdot e(\mathrm{As})}{x(\mathrm{As})} = \frac{3 + 1 + 2 \cdot 5}{2} = 7$$

For the As ions, *b*(As–As) is 1 using a *VEC* of 7:

$$b(\mathrm{As–As}) = 8 - VEC(\mathrm{As}) = 8 - 7 = 1$$

According to this calculation, two possible structural motives may be predicted for the planar layer: On the one hand, the arsenide ions may be considered as pseudoelements of group 17 and form As_2^{4-} dumbbells, on the other hand another motive is possible with regard to the crystal structure of the *LnT*As$_2$ compounds: Due to the two crystallographically different As atoms, a disproportion of the number of bonds as found for the lanthanide polychalcogenides [48] has to be considered. Therefore two types of As atoms arise: Isolated As^{3-} ions with *b*(As–As) = 0 in the PbO-like layer and chains or rings of As^- ions with *b*(As–As) = 2 in the planar layers.

According to the latter case, the four distortion variants of planar 4^4-nets, which are known today, are presented in the following:

- Zigzag chains of Sb atoms were found in the structure of SrZnSb$_2$ (space group *Pnma* (No. 62), *a* = 23.05(1) Å, *b* = 4.37(2) Å, *c* = 4.46(1) Å, figure 2.6 left) [49]. This structure can be derived from the SrZnBi$_2$ type (space group *I*4/*mmm*, *a* = 4.64(1) Å, *c* = 21.96(3) Å) [37], which contains square 4^4-nets of Bi atoms. Several binary and ternary compounds containing zigzag chains are known in literature: ZrSi$_2$ [50, 51], PdP$_2$ [52], HoSb$_2$ [53, 54], CeNiSi$_2$ [55], CeSAs [56, 57], SmSAs [56–58], LaP$_2$ [59], CaSb$_2$ [60, 61], *Ln*SeAs [62], LaTeSb [63], LaNiGe$_2$ [64], *Ln*TeAs [65] ErCuP$_2$ [21, 22, 66], CeTeSb [67] and *Ln*AgAs$_2$ [29].
- Cis-trans chains of P atoms were found in GdSP (space group *Pcmb* (No. 57), *a* = 5.401(1) Å, *b* = 5.362(1) Å, *c* = 16.742(2) Å [68, 69] figure 2.6 right), which is derived from the ZrSSi type (space group *P*4/*nmm*, *a* ≈ 4 Å, *c* ≈ 8 Å). The P–P distances between the chains are 3.222(1) Å, those in the chains 2.252(2) Å and

2.272 Å. The latter ones are similar to those in white phosphorous, which were determined to 2.186(1) Å [70].

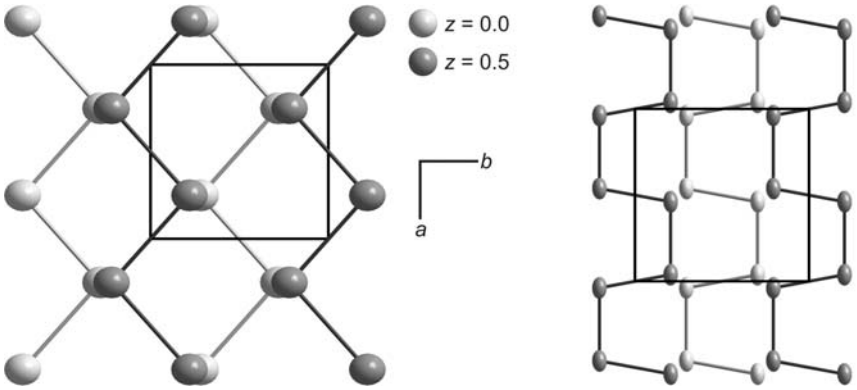

Figure 2.6: Zigzag chains of Sb atoms in $SrZnSb_2$ (left) and cis-trans chains of P atoms in GdSP (right). Light gray atoms at $z = 0.0$, dark gray atoms at $z = 0.5$.

- Dumb-bells of As atoms were found in NdSeAs (space group $P112_1/n$ (No. 14), $a = 4.035(1)$ Å, $b = 4.036(2)$ Å, $c = 17.645(1)$ Å, $\gamma = 90.0(1)$ °, figure 2.7 left) [70]. The distances are 2.700(1) Å in the dimers and 2.858(2) between them. For comparison, the As–As distances in gray As are 2.44(1) Å [71].
- Discrete four-membered rings were found for the P atoms in $SmCu_{1.15}P_2$ (space group *Cmmm* (No. 65), $a = 5.453(3)$ Å, $b = 19.512(1)$ Å, $c = 5.439(3)$ Å, figure 2.7 right) [21, 22, 66] with P–P distances of 2.266(6) Å and 2.584(6) Å.

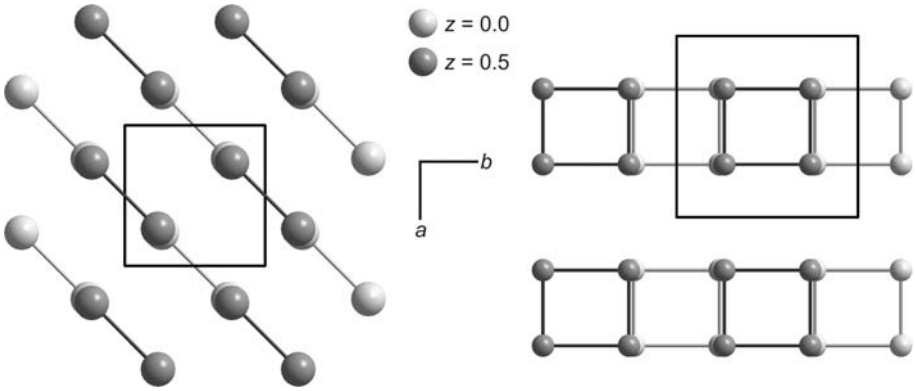

Figure 2.7: Dumb-bells of As atoms in NdSeAs (left) and isolated four-membered rings of P atoms in $SmCu_{1.15}P_2$ (right). Light gray atoms at $z = 0.0$, dark gray atoms at $z = 0.5$.

Structures of the $LnAgAs_2$ and $LnAuAs_2$ compounds (*Ln* = La, Ce – Nd, Sm, Gd, Tb) are already known from literature [24, 29, 44]. In 2001, *Demchyna* et al. [44] reported the crystal structures of the $LnAgAs_2$ compounds (*Ln* = La, Ce – Nd, Sm, Gd – Dy). $LaAgAs_2$ and $CeAgAs_2$ were described in $P4/nmm$ (No. 129, i.e. the structure of the aristotype), which contains no distortion in the As layer due to the fourfold axis. The other compounds were

refined in *Pmmn* (No. 59), which is a *translationengleiche* subgroup of *P*4/*nmm*. All results are based on powder diffraction data.

In 2003, *Eschen* and *Jeitschko* [29] published the crystal structures of the *Ln*$AgAs_2$ and *Ln*$AuAs_2$ compounds (*Ln* = La, Ce – Nd, Sm, Gd, Tb). $LaAgAs_2$, $CeAgAs_2$ and all gold compounds despite $LaAuAs_2$ were refined in space group *P*4/*nmm*. The other silver compounds are reported to crystallize in space group *Pnma* (No. 62), which is a twofold superstructure ($c' = 2c$) of the aristotype. In this case, the As atoms are arranged in zigzag chains. $LaAuAs_2$ crystallizes in *I*4/*nmm*, which is an additional stacking variant of the $HfCuSi_2$ type with undistorted layers of As atoms. Only the structures of $CeAgAs_2$, $PrAgAs_2$, $LaAuAs_2$ and $CeAuAs_2$ are based on single-crystal diffraction data of a four-circle diffractometer, the other structures are based on comparison of the powder diffraction patterns.

In 2004, *Demchyna* et al. [24] reported the structure of $CeAgAs_2$ in *Pmca* (No. 57), which is a fourfold superstructure of the $HfCuSi_2$ type with $a' = \sqrt{2}\,a$, $b' = \sqrt{2}\,b$, $c' = 2\,c$. In this orthorhombic cell, the As atoms are arranged in cis-trans chains.

The magnetism of the *Ln*$Cu_{1+\delta}As_2$ (*Ln* = La, Ce – Nd, Sm), *LnT*As_2 and *LnT*Sb_2 compounds is rather simple at a first glance. Most of the reported structures are paramagnetic following a Curie-Weiss law above 100 K and order antiferromagnetically at low temperatures [8, 20–24, 26, 27]. The transition temperatures vary from 2.5 K for $NdCu_{1.06}As_2$ [27] to 14 K for $GdAgSb_2$ [23]. Since $YCuAs_2$ was found to be diamagnetic and $LuCuAs_2$ is essentially a Pauli paramagnet, Cu^+ is diamagnetic and the magnetic behavior of the ternary compounds can be attributed to the lanthanide ions, only. The magnetic moments derived from the Curie-Weiss law are in general in good agreement with those for trivalent states of the respective lanthanide elements [27]. Analyzing the magnetic nature of these compounds more carefully, a deviation of the conclusion drawn above is evident for some of the compounds:

The devolution of the magnetization curve of $SmCu_{1.05}As_2$ does not follow the Curie-Weiss law, which is referred to the fact that the first excited state of the Hund's rule multiplet ($J = 7/2$) is very close to the ground state ($J = 5/2$) [27]. $CeCu_{1.10}As_2$ was found to be paramagnetic down to 1.72 K (lower limit of the measurement), whereas both $CeAgAs_2$ and $CeAuAs_2$ are antiferromagnetic at low temperatures ($T_N = 6$ K and 4K, respectively) [26]. A metamagnetic transition at low temperature and low magnetic fields is found for $CeAgAs_2$ [24, 26] and $CeAuAs_2$ [26]. For the latter compound, a structural change is predicted at

approximately 280 K due to an inflection and hysteresis in the magnetic susceptibility curves [26].

An incommensurately modulated magnetic structure with anisotropy in the *ab*-plane near the transition temperature is reported for $TbCuSb_2$ [23]. In the case of $CeAgSb_2$, weak ferromagnetism with $T_C < 12$ K is reported [20].

The electrical resistivity ρ of the lanthanide copper diarsenides is more consistent than the magnetic properties. The resistivity of all reported compounds decreases more or less monotonically revealing metallic properties. At the magnetic transition temperature an anomaly, which might be referred to as a Kondo-like behavior is found [22, 25–28]. This results from the 2D square nets of As atoms, which create partially filled bands at the Fermi level [21]. The Kondo-like behavior is reported for $CeAgAs_2$ and $CeAuAs_2$ as well [26]. One exception is $CeCuAs_2$, which reveals semiconducting behavior. Applying magnetic fields or pressure reduces the semiconducting properties and at pressures above 9 GPa, metallic temperature-dependent behavior including the before mentioned Kondo-like rise of ρ is found [28, 72]. For the Sm compound, ρ increases with T faster at temperatures beyond 150 K than the linearly extrapolated values of low temperatures, whereas for the Gd compound a decrease of ρ is reported [27].

3 Experimental

3.1 Synthesis

The preparations were carried out in an argon-filled glove box (M. Braun, $p(O_2) \leq 1$ ppm, $p(H_2O) \leq 1$ ppm, argon purification with molecular sieve and copper catalyst). The manufacturers and qualitites of the respective reaction educts are summarized in table 3.1. Pieces of lanthanum, cerium, praseodymium, neodymium, samarium, gadolinium or terbium freshly filed from rods of the respective rare earth metals, copper, silver or gold, and arsenic (As_2O_3 removed by sublimation prior to use) were mixed in the atomic ratio of 1:1:2. The reactions were carried out in a six-fold excess of a LiCl/KCl flux (dried at 410 K in dynamic vacuum prior to use) in glassy carbon crucibles, which were sealed in evacuated silica tubes. The samples were heated up to 1023 K for 48 hours, annealed for 96 hours, and cooled to 623 K during 192 hours. The flux was removed with water and the products were washed with ethanol. Air stable, shiny black platelets of the target compounds were obtained.

Table 3.1: Reaction educts for the synthesis of the *Ln*TAs_2 compounds.

substance	purity	supplier
La	99.9% metal based	Treibacher AG, Althofen
Ce	99.9% metal based	Treibacher AG, Althofen TBL Kelpin, Neuhausen
Pr	99.9% metal based	Treibacher AG, Althofen
Nd	99.9% metal based	Treibacher AG, Althofen
Sm	99.9% metal based	Chempur GmbH, Karlsruhe
Gd	99.9% metal based	ABCR, Karlsruhe
Tb	99.9% metal based	TBL Kelpin, Neuhausen
Cu	p.a.	Chemapol, Frankfurt/Main
Ag	99.9%	Chempur GmbH, Karlsruhe
Au	99.9+%	Chempur GmbH, Karlsruhe
As	99.997% metal based	Aldrich Chemical Company, Steinheim
LiCl	p.a.	Merck KGaA, Darmstadt
KCl	p.a.	Merck KGaA, Darmstadt
C_2H_5OH	96%	Merck KGaA, Darmstadt

3.2 X-ray Investigations

Powder samples of the reaction products were measured on a Stadi P diffractometer (Stoe & Cie., Darmstadt, Cu $K\alpha_1$, Ge monochromator) and characterized with the WinXPow program package [73]. Buerger precession photographs (Zr-filtered Mo radiation, imaging plate system) were taken in order to check the quality of the crystals and to determine the lattice parameters and the reflection conditions. Complete data sets for structure refinements were recorded on an imaging plate diffraction system (IPDS I or IPDS II, both Stoe & Cie., Darmstadt, Mo $K\alpha$ radiation, graphite monochromator). The descriptions of the shapes of the platelets were optimized using sets of symmetrically equivalent reflections [74, 75]. Numerical absorption corrections were applied using XRed32 [74] and the structure models were refined with the SHELX97 program package [76]. For incommensurately modulated structures, numerical absorption corrections were applied using the JANA2000 software package [77] and the structure models were refined with JANA2000, too.

3.3 Refinement Strategy of the Modulated Structures

Weak satellite reflections of 1st order were observed in every ($h0l$) layer. Since the modulation vector $\mathbf{q} = (\alpha 0 \gamma)$ is incompatible with tetragonal or orthorhombic symmetry, the symmetry had to be reduced to the monoclinic crystal system following the Bärnighausen formalism [78, 79]. The basic structure in $P12_1/m1$ (No. 11) was then refined using the SHELX program package.

Due to the reflection conditions for the satellites, the monoclinic super space group $P12_1/m1(\alpha 0 \gamma)00$ (No. 11.1) [80] was chosen for structure refinement. Using the atom positions of the basic structure, the modulated structure was refined with Jana2000.

One harmonic modulation wave for the positional modulation and for the displacement parameters of all atoms were introduced. Four twin fractions were considered due to two *translationengleiche* steps of index 2 in the respective Bärnighausen trees. A harmonic occupancy modulation wave was introduced for the Au atoms, which led to a considerable drop in the *R*-values.

3.4 Conductivity

The temperature dependent (20 K ≤ T ≤ 310 K) resistivity was studied by a four-probe method on pressed and sintered cylindrical samples (pellets) with 6 mm diameter and 2 mm height, approximately. Silver paste was used as contacting agent to prepare four contacts in linear geometry. Since the samples were sintered at 523 K from ground polycrystals, the density of the material is not known exactly and therefore the geometry coefficient could be estimated only. After preparation, all measurements were performed under vacuum conditions in a two-stage Gifford-McMahon refrigerator with a temperature sweep rate of 2 K min^{-1}. Dependent on the resistivity of the sample at room temperature, a measuring current between 10 μA for compounds with semiconducting character and 100 mA for those with metallic behavior was chosen.

3.5 Band Structure Calculations

Density functional band structure calculations using a full potential all-electron local orbital code FPLO (version fplo8.00–31) [81, 82] within the local (spin) density approximation (L(S)DA) were performed including spin-orbit coupling when needed. The Perdew-Wang [83] parameterization of the exchange-correlation potential was employed. Density of states (DOS) and band structures were calculated after convergence of the total energy on a dense k-mesh with 12×12×12 points. The strong Coulomb repulsion in the Pr 4f orbitals are treated on a mean field level using the LSDA+U approximation in the atomic-limit double counting scheme [84, 85]. The presented results use the LSDA+U method [86] in the rotationally invariant form [87], as a representative value, U = 8 eV was chosen. A variation of U between 6 and 10 eV does not significantly influence the relevant valence states. The experimental structural parameters have been used throughout the calculations.

3.6 Magnetization

Powders of randomly oriented small crystallites were loosely embedded into a cylindrical form with diluted glue. The samples were measured in a Quantum Design physical properties measurement system (PPMS) with vibrating magnetometer (VSM) option in fields up to 9 T and in a temperature range from 2 K to 300 K. Hysteresis loops were conducted with a field sweep rate of 0.02 T min^{-1} and temperature dependent magnetization measurements were performed at a fixed field of $\mu_0 H$ = 0.25 T with a temperature sweep rate of 2 K min^{-1}.

4 Commensurately Modulated Structures

4.1 Powder Patterns

Powder diffraction data of the reaction products revealed that the La, Ce, Pr, Nd and Sm compounds were obtained as single-phase samples at a reaction temperature of 1023 K, $GdAgAs_2$ and $TbAgAs_2$ were accompanied with a considerable amount of the respective binary lanthanide arsenide *Ln*As and elemental silver. The X-ray powder diffraction patterns are shown in figure 4.1 for $SmAuAs_2$ as representative for the compounds crystallizing in a twofold superstructure and in figure 4.2 for $LaAgAs_2$ representing a compound crystallizing in a fourfold superstructure of the $HfCuSi_2$ type. The cell parameters and the volume obtained from the powder data are summarized in table 4.1 Crystals of $GdAgAs_2$ and $TbAgAs_2$ for single-crystal X-ray investigations could be selected manually from the multiphase reaction mixtures.

Table 4.1: Lattice parameters (Å) and unit cell volumes (Å^3) of the *LnT*As$_2$ compounds

compound	*a*	*b*	*c*	*V*
$LaAgAs_2$	5.801(2)	5.814(2)	21.219(4)	715.5(3)
$CeAgAs_2$	5.771(2)	5.775(2)	21.081(4)	702.6(2)
$PrAgAs_2$	4.017(1)	4.062(1)	21.027(4)	343.1(1)
$NdAgAs_2$	4.032(1)	4.032(1)	20.977(4)	341.0(1)
$SmAgAs_2$	3.995(1)	4.013(1)	20.872(1)	333.1(1)
$GdAgAs_2$	3.973(1)	3.976(1)	20.841(3)	329.3(1)
$TbAgAs_2$	3.956(1)	3.955(1)	20.748(1)	324.6(1)
$PrAuAs_2$	5.766(2)	5.757(2)	20.458(4)	679.1(2)
$NdAuAs_2$	4.058(1)	4.059(1)	20.435(4)	336.6(1)
$SmAuAs_2$	4.019(1)	4.049(1)	20.331(4)	330.9(1)

The powder diffractograms show broadening or splitting of some reflections at higher diffraction angles, e.g. reflections 020 and 200 at $2\theta \approx 45\,°$ or reflections 134 and 314 at $2\theta \approx 77\,°$ for $SmAuAs_2$, and reflections 424 and 244 at $2\theta \approx 75\,°$ for $LaAgAs_2$. This indicates a distortion of the tetragonal cell of the aristotype for both types of superstructures.

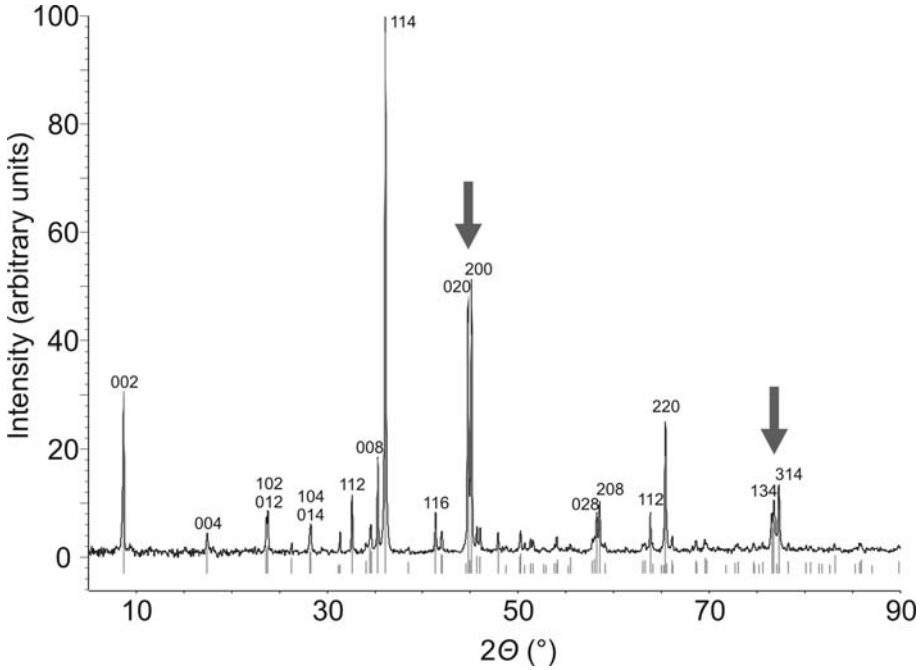

Figure 4.1: X-ray powder diffraction pattern of $SmAuAs_2$ and calculated peaks in space group *Pmcn* (No. 62, zigzag chains). The arrows indicate the split reflections 020/ 200 and 134/ 314.

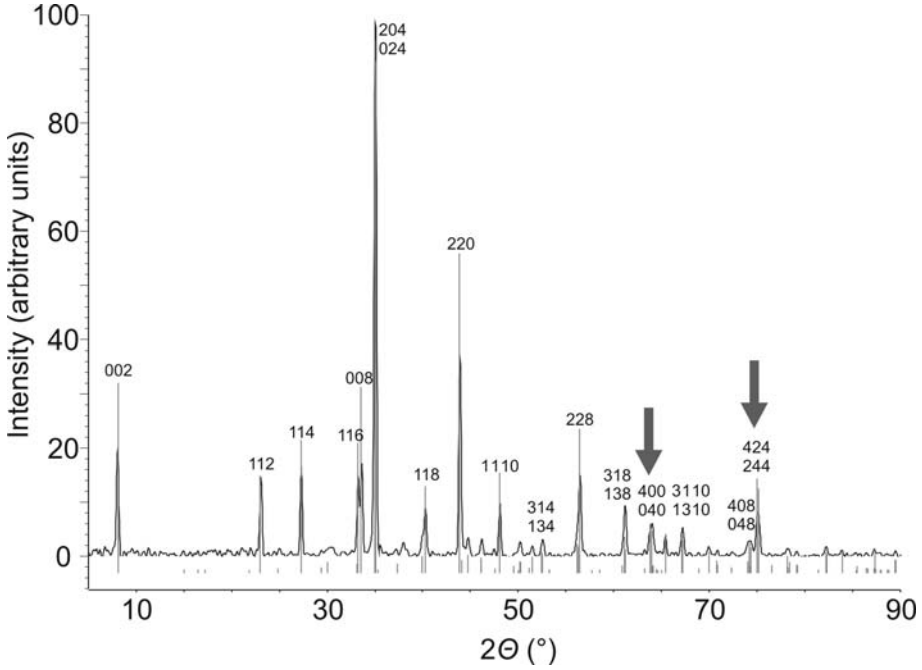

Figure 4.2: X-ray powder diffraction pattern of $LaAgAs_2$ and calculated peaks in space group *Pmca* (No. 57, cis-trans chains). The arrows indicate the broadened reflection 400/ 040 and 424/ 244

4.2 Single-Crystal Structure Determinations

Precession photographs of $PrAgAs_2$, $NdAgAs_2$, $SmAgAs_2$, $GdAgAs_2$, $TbAgAs_2$, $NdAuAs_2$ and $SmAuAs_2$ show a (pseudo-)tetragonal unit cell with $a \approx b \approx 4$ Å and $c \approx 20.5$ Å (figure 4.3). Photographs of $LaAgAs_2$, $CeAgAs_2$ and $PrAuAs_2$ revealed a (pseudo-)tetragonal unit cell with $a \approx b \approx 5.8$ Å ($= \sqrt{2} \cdot 4$ Å) and $c \approx 21$ Å (figure 4.4). Due to the better contrasts, reciprocal layers simulated of the diffractometer data sets of the respective compounds are presented in figures 4.3 and 4.4.

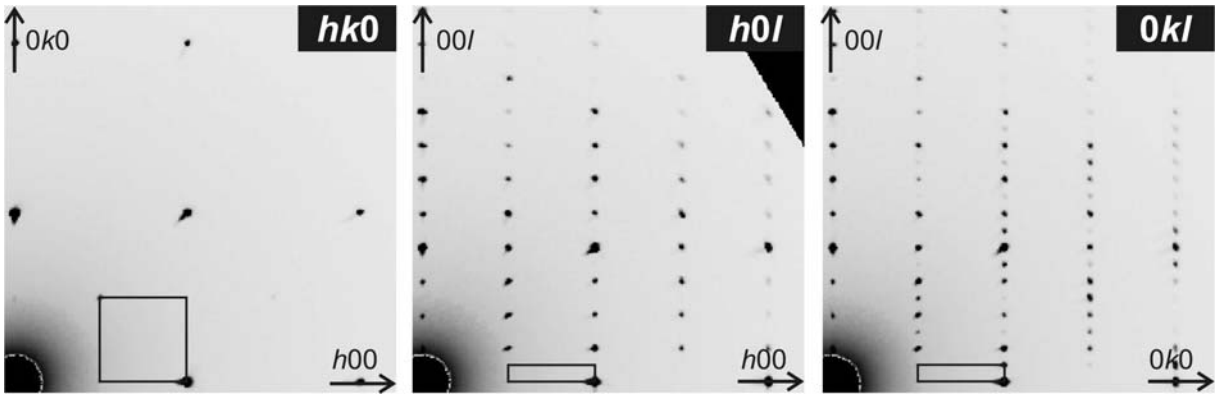

Figure 4.3: Simulated reciprocal layers *hk*0, *h*0*l*, 0*kl* of $SmAuAs_2$ as an example for a pseudo-tetragonal unit cell with $a \approx b \approx 4$ Å and $c \approx 20.5$ Å (twofold superstructure). The unit cell is emphasized in the images.

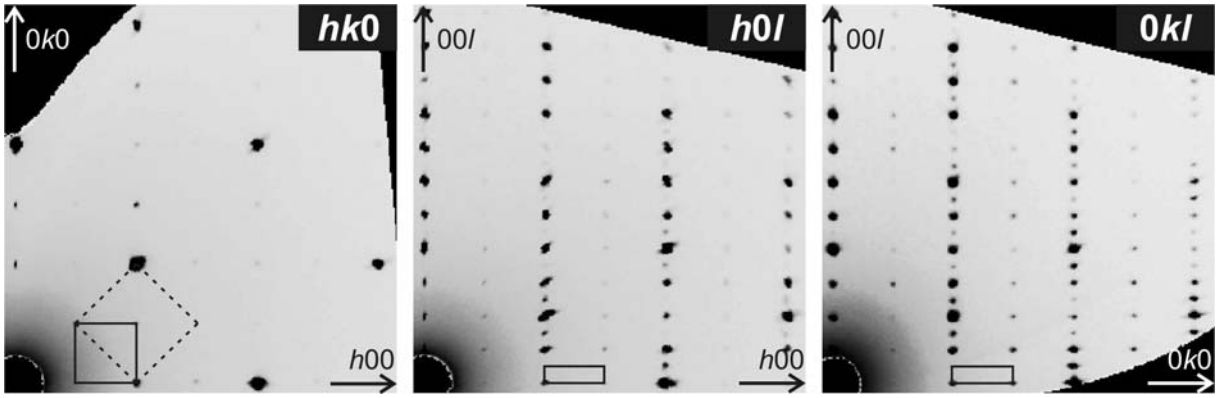

Figure 4.4: Simulated reciprocal layers *hk*0, *h*0*l*, 0*kl* of $PrAuAs_2$ as an example for a pseudo-tetragonal unit cell with $a \approx b \approx 5.8$ Å ($\sqrt{2} \cdot 4$ Å) and $c \approx 21$ Å (fourfold superstructure). The unit cell is emphasized in the images. The dashed line in the *hk*0 layer emphasizes a twofold superstructure with $a \approx b \approx 4$ Å.

Based on the main reflections of the single-crystal diffraction data, a model of the average structure was developed for $SmAuAs_2$ in *P*4/*nmm* (No. 129, figure 4.5) using the atomic positions of the $HfCuSi_2$ type as a starting point. In this structure, the results of the refinement match those obtained by *Eschen* and *Jeitschko* [29]. The most striking part of the structure are the exceptional large thermal displacement parameters observed for the As2 atoms in the arsenic layers.

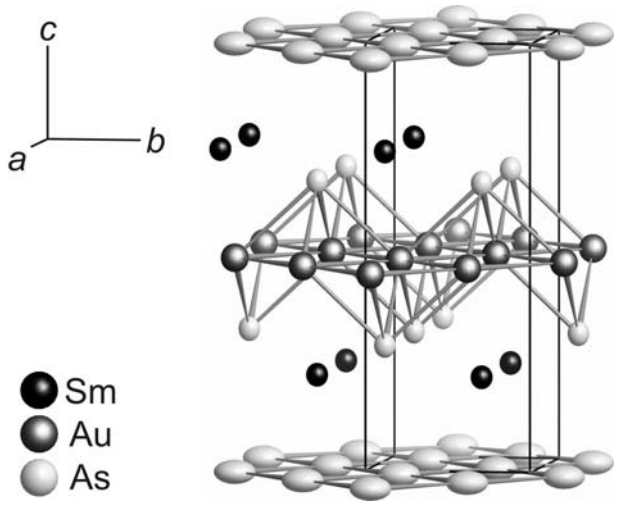

Figure 4.5: Average structure for $SmAuAs_2$ in *P*4/*nmm*, ellipsoids at the 99% probability level.

Analysis of the single-crystal data revealed for $PrAgAs_2$, $NdAgAs_2$, $SmAgAs_2$, $GdAgAs_2$, $TbAgAs_2$, $NdAuAs_2$ and $SmAuAs_2$ a twofold superstructure ($a' = a_0$, $b' = b_0$, $c' = 2\,c_0$) of the aristotype with Laue symmetry *mmm*. Space group *Pmcn* (No. 62, non-standard setting of *Pnma*) was identified following the Bärnighausen formalism [78, 79] stated in figure 4.6. Non-standard settings were chosen to emphasize the structural relationship with the tetragonal aristotype (stacked layers along [001]). The Wyckoff positions, atomic coordinates, displacement parameters, final results of the refinements, relevant crystallographic data as well as interatomic distances can be found in the tables of the respective compounds in the annex.

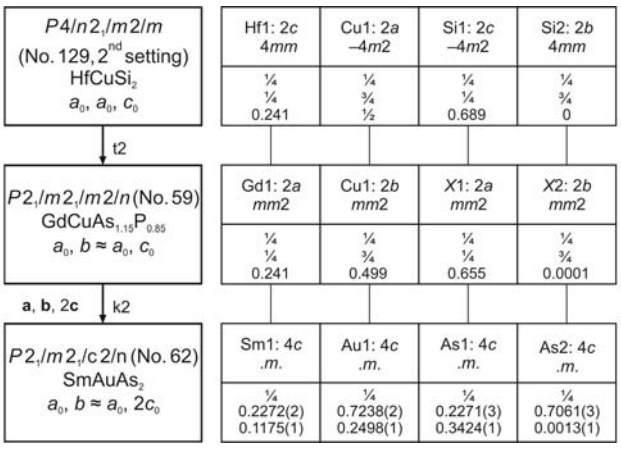

Figure 4.6: Bärnighausen tree for the symmetry relation between the $HfCuSi_2$ (*P*4/*nmm*) and the $SmAuAs_2$ structure (*Pmcn*). Note that the atomic positions of the $HfCuSi_2$ type are shifted by z+½ with respect to the data given in the original publication [33].

In an analogous way, space group *Pmca* (No. 57, non-standard setting of *Pbcm*) was identified for the fourfold superstructures of $LaAgAs_2$, $CeAgAs_2$ and $PrAuAs_2$ following the Bärnighausen formalism stated in figure 4.7. The Wyckoff positions, atomic coordinates,

displacement parameters, final results of the refinements, relevant crystallographic data as well as interatomic distances can be found in the tables of the crystallographic data sheets of the respective compounds in the annex.

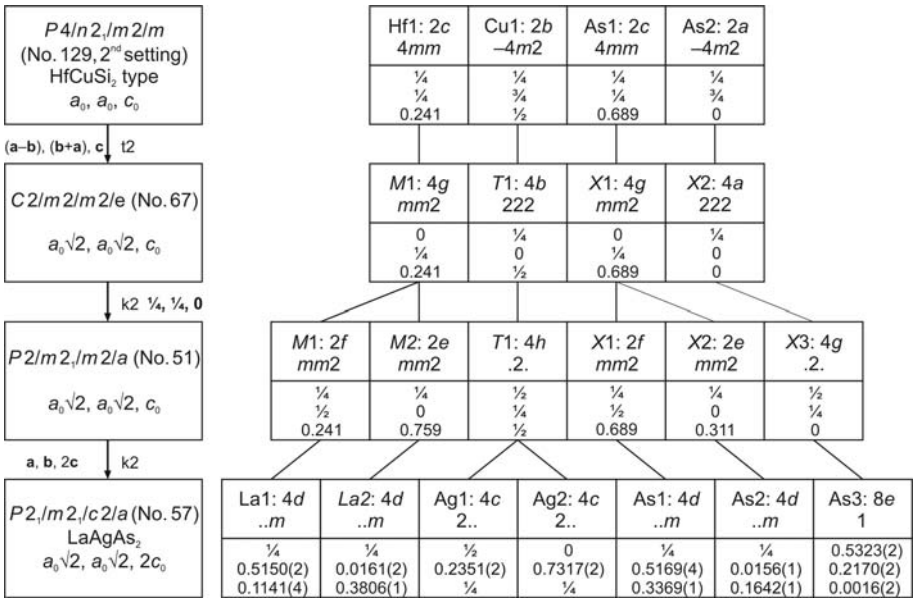

Figure 4.7: Bärnighausen tree for the symmetry relation between the $HfCuSi_2$ (*P*4/*nmm*) and the $LaAgAs_2$ structure (*Pmca*). Note that the atomic positions of the $HfCuSi_2$ type are shifted by z+½ with respect to the data given in the original publication [33].

Contrary to the respective early *Ln*$CuAs_2$ (*Ln* = La, Ce, Pr, Nd, Sm), which have been reported in literature to crystallize with an excess of copper (from $LaCu_{1.25}As_2$ to $SmCu_{1.05}As_2$) [8, 45] and an undistorted arsenic layer, the silver and gold compounds investigated here crystallize in an 1:1:2 ratio or, in the case of $CeAu_{1-\delta}As_2$, with a slight deficiency of gold.

In both types of superstructures, the *Ln* atoms are surrounded by square antiprisms of As atoms of the PbO-like layer and As atoms of the distorted planar layers leading to three different *Ln*–As distances. The As atoms of the planar layers are surrounded by a square antiprism of *Ln* and *T* atoms, the As atoms of the arsenic layer by four As atoms and four *Ln* atoms. The latter motive can be described as a (4+4) coordination, set up by a compressed tetrahedron of *Ln* atoms and a rectangle of As atoms around the central As atom (figure 4.8 left). A (4+4+4) coordination is realized for the *T* atoms consisting of two interpenetrating elongated tetrahedra of *Ln* or As atoms and a square of *T* atoms (figure 4.8 right).

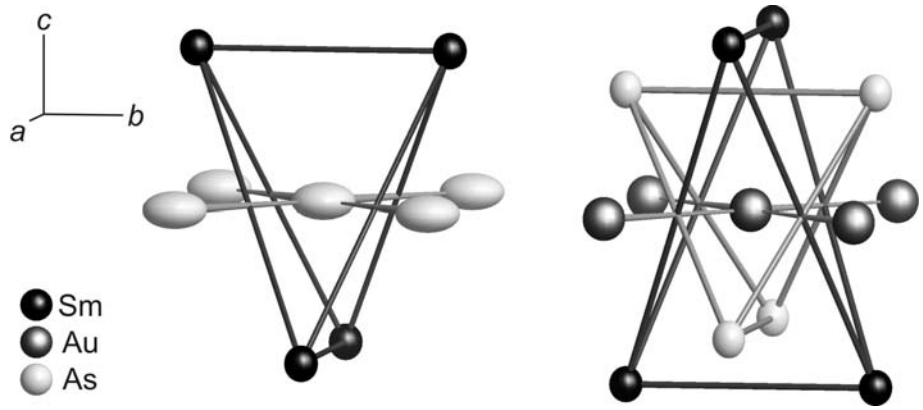

Figure 4.8: Coordination polyhedra for the As2 atom (left) and the Au atom (right) of $SmAuAs_2$ in *P*4/*nmm*, ellipsoids at the 99% probability level.

The main difference between the undistorted aristotype and the distorted compounds is found in the planar layer of the main group elements Si and As, respectively. In accordance with crystal structure and magnetic data (*vide infra*), the formula of the title compounds can be re-written as $Ln^{3+}T^{+}As^{3-}As^{-}$, where the As^{3-} are found in the puckered [*Ln*As] slabs and the As^{-} atoms in the planar layers. Following the Zintl-Klemm concept the As^{-} should be two-bonded due to their pseudo-chalcogen character. This is realized in the $LnTAs_2$ compounds by the formation of planar As chains.

The assignment of the wrong space groups for numerous $LnAgAs_2$ and $LnAuAs_2$ compounds in literature [29, 44] may be traced back to the fact that all crystals (despite $SmAuAs_2$ in this study) are twinned along [001] due to the pseudo-tetragonal cell. Consequently, the zonal reflection conditions *h*0*l*: $l = 2n$ for space group *Pmcn* and *h*0*l*: $l = 2n$, *hk*0: $h = 2n$ for space group *Pmca* [30] are violated (cf. figures 4.3 and 4.4) and the determination of the correct space group is hampered. In fact, it can best be accomplished following the Bärnighausen formalism.

In the case of the twofold superstructures, infinite zigzag chains of the As2 atoms along [010] are found (figure 4.9). This comes along with an orthorhombic deformation of the $HfCuSi_2$ structure. The doubling of the *c*-axis is due to a shift of $\Delta x = \Delta y = 0.5$ of the As2 atoms in alternating layers in $z \approx 0$ and $z \approx 0.5$. The superposition of both shifts is the origin of the exceptional large anisotropic displacement parameters of the As2 atoms in the *P*4/*nmm* average structure.

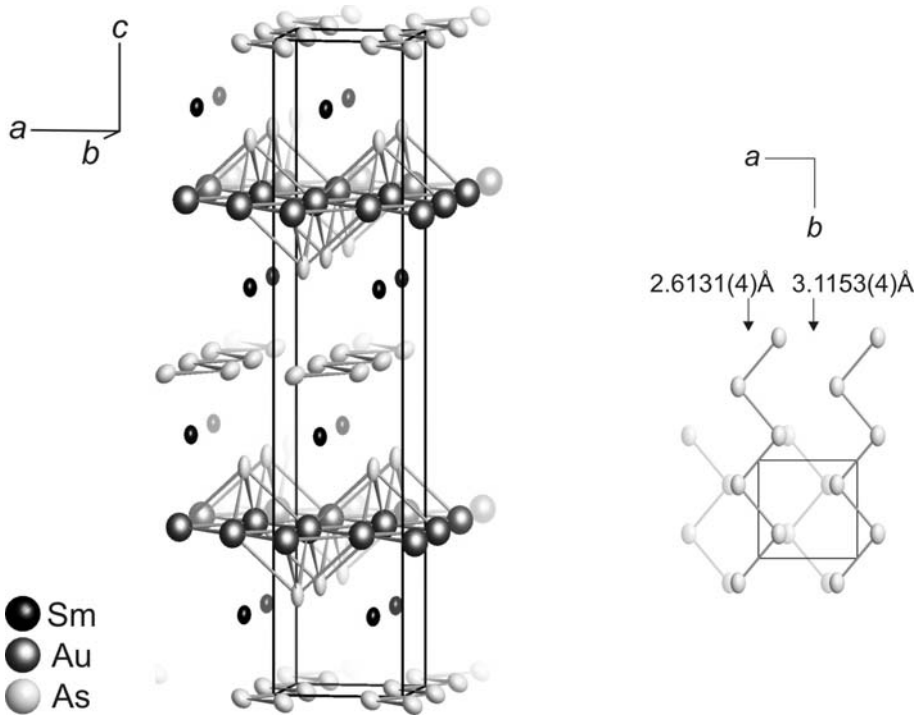

Figure 4.9: Structure of $SmAuAs_2$ in *Pmcn* (No. 62), ellipsoids at the 99.9% probability level. Left: detail of the structure with emphasized unit cell, right: As2 layers along [001] including distances in and between chains.

In the case of the fourfold superstructures, infinite cis-trans chains of the As3 atoms along [010] are found (figure 4.10), which results in the formation of the $\sqrt{2}a \cdot \sqrt{2}b$ enlargement of the unit cell. The doubling of the *c*-axis is in this case caused by a shift of $\Delta y = 0.5$, which corresponds to an inverse orientation of the cis-trans chains in $z \approx 0$ and $z \approx 0.5$.

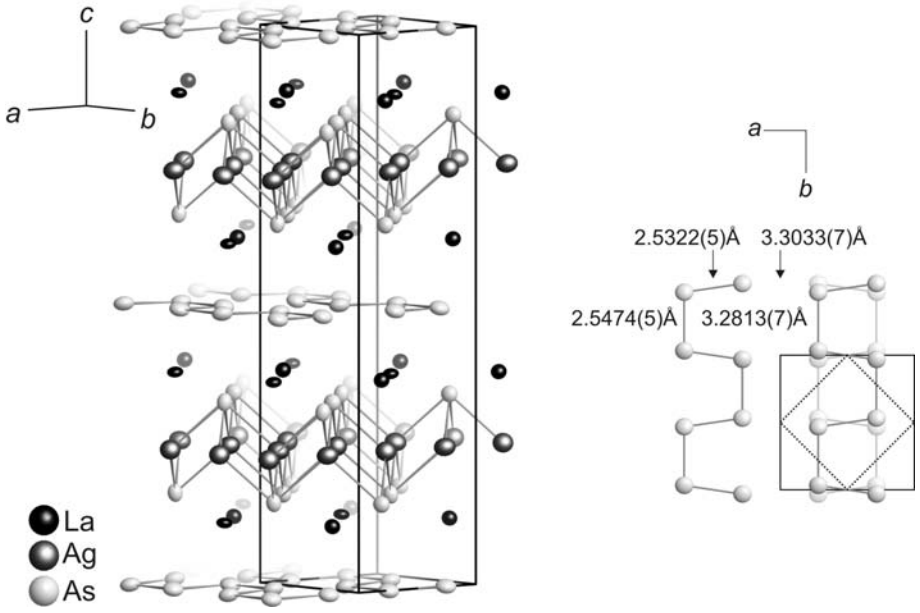

Figure 4.10: Structure of $LaAgAs_2$ in *Pmca* (No. 57), ellipsoids at the 99.9% probability level. Left: detail of the structure with emphasized unit cell, right: As3 layers along [001] including distances in and between chains.

5 Incommensurately Modulated Structures

5.1 $GdCuAs_2$, $GdAu_{1-\delta}As_2$ and $TbCu_{1-\delta}As_2$

Note: The title compounds were obtained in the composition $GdCuAs_2$, $GdAu_{0.973(3)}As_2$ and $TbAu_{0.966(6)}As_2$. To improve the readability in the text, the two latter compounds are denominated as $GdAuAs_2$ and $TbAuAs_2$, respectively. The crystallographic tables in the annex contain the proper compositions.

5.1.1 Powder Patterns

Powder diffraction data of the reaction products (figure 5.1) revealed that only $GdCuAs_2$ was obtained as a single-phase sample under the conditions stated in the experimental section. As can be seen from the diffractograms, $GdAuAs_2$ and $TbAuAs_2$ were accompanied with considerable amounts of the respective binary lanthanide arsenide *Ln*As and elemental gold at a reaction temperature of 1123 K. The reduction of the reaction temperature to 1023 K led to a lower but still detectable amount of the by-products. Crystals of the target compounds for X-ray investigations were selected manually.

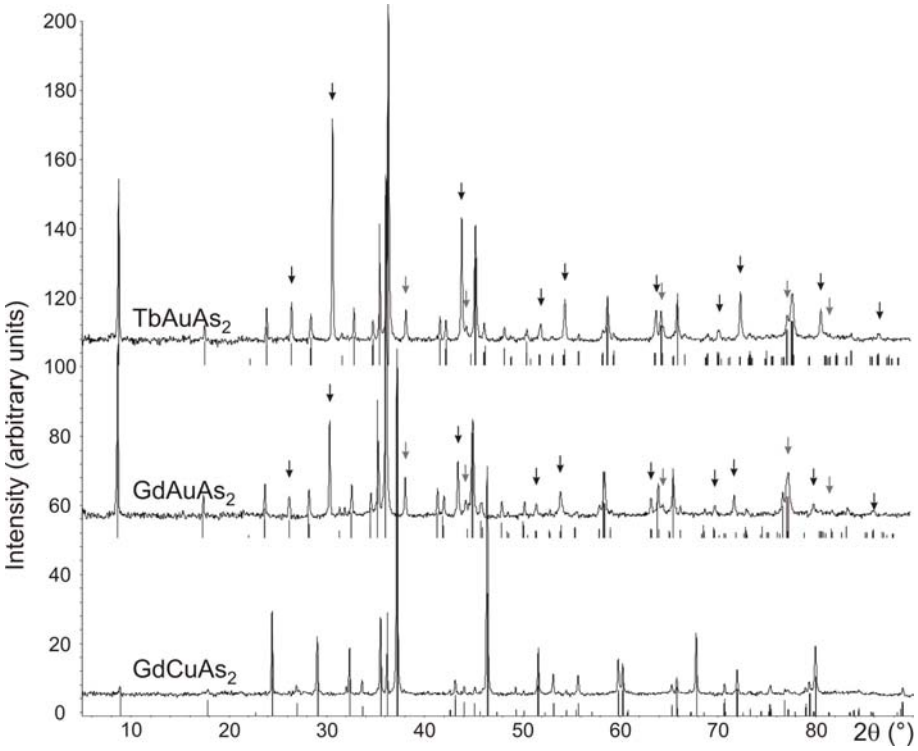

Figure 5.1: X-ray powder diffraction patterns of $TbAuAs_2$ (top), $GdAuAs_2$ (center) and $GdCuAs_2$ (bottom); reflections of the respective ternary compounds are indicated with black lines, reflections of by-products are highlighted (lanthanide arsenide black arrow, elemental gold gray arrow).

Applying the restrictions for the monoclinic crystal system (*vide infra*), the lattice parameters of the basic structures determined from powder diffraction data at 293(2) K were determined (table 5.1).

Table 5.1: Lattice parameters of the basic structures of $GdCuAs_2$, $GdAuAs_2$ and $TbAuAs_2$ determined from powder diffraction data (293(2) K).

	a_b (Å)	b_b (Å)	c_b (Å)	β_b (°)
$GdCuAs_2$	3.904(1)	3.902(1)	9.908(2)	90.05(3)
$GdAuAs_2$	3.957(1)	4.060(2)	10.135(2)	90.01(3)
$TbAuAs_2$	3.933(2)	3.986(1)	10.080(2)	90.00(3)

5.1.2 Average Structures

Precession photographs of $GdCuAs_2$, $GdAuAs_2$ and $TbAuAs_2$ revealed a (pseudo-)tetragonal unit cell with $a \approx b \approx 4$ Å and $c \approx 10$ Å. The satellite reflections were visible as blurred spots only. As the monoclinic angles determined from powder data do not differ from 90° within an uncertainty interval of 3σ, the orthorhombic space group *Pmmn* (No. 59) was deduced for the average structures in accordance with lattice parameters and diffraction images of the main reflections. Models for the average structures were then developed. The average structure of $TbAuAs_2$ in *Pmmn* with lattice parameters of $a = 3.933(2)$ Å, $b = 4.089(2)$ Å and $c = 10.1350(14)$ Å is shown in figure 5.2.

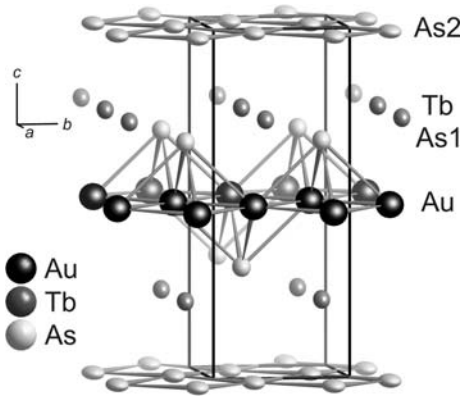

Figure 5.2: Average structure for $TbAuAs_2$ in *Pmmn* (No. 59), ellipsoids at the 99% probability level.

The Wyckoff positions, atomic coordinates and displacement parameters of the average structures of $GdCuAs_2$, $GdAuAs_2$ and $TbAuAs_2$ are summarized in the data sheet for each compound in the annex. The quite large anisotropic displacement parameters of the As2 atoms can be taken as the result of the modulation.

5.1.3 Modulated Structures

Reciprocal layers, simulated from the diffractometer data sets, revealed satellites with $l \pm \gamma$ (for the values of α and γ, see table 5.2) of low intensities. Due to the positions of these additional reflections and a constant splitting of their intensity maxima (figure 5.3), commensurate superstructures and twinning of 3D structures can be excluded as the origin for the additional reflections. In fact, we deal with incommensurate modulations here.

Analysis of the fractional indices of the satellite reflections showed that they could be indexed with four integer indices *h k l m* according to:

$$\mathbf{H}_i = h \cdot \mathbf{a}_1^* + k \cdot \mathbf{a}_2^* + l \cdot \mathbf{a}_3^* + m \cdot \mathbf{q},$$

with

$$\mathbf{q} = \alpha \cdot \mathbf{a}^* + \beta \cdot \mathbf{b}^* + \gamma \cdot \mathbf{c}^*.$$

The structures were thus treated as one-dimensional modulated structures employing the superspace formalism [88–90]. Atomic positions are described as the sum of the average positions and the modulation functions. The latter are given as a truncated Fourier series, where the Fourier coefficients are used as independent parameters in the refinement:

$$u_i(\bar{x}_{s_4}) = \sum_{n_1=0}^{\infty} A_i^{n_1} \cos(2\pi n_1 \bar{x}_{s_4}) + B_i^{n_1} \sin(2\pi n_1 \bar{x}_{s_4}),$$

where $i = 1, 2, 3$ or (x, y, z) and $A_i^{n_1}$ and $B_i^{n_1}$ are the structural parameters. The fourth superspace coordinate is defined by

$$\bar{x}_{s_4} = t - \mathbf{q} \cdot \mathbf{r}^0,$$

with $\cdot\mathbf{r}^0$ denoting the average position of the atoms and t defining the section of superspace or the initial phase of the modulation functions. Similar modulation functions were used for the temperature factors. The translational parts of the modulation wave vectors $\mathbf{q} = \alpha \cdot \mathbf{a}^* + \beta \cdot \mathbf{b}^* + \gamma \cdot \mathbf{c}^*$ are summarized in table 5.2.

Table 5.2: Refined translational parts α and γ of the modulation vector $\mathbf{q} = \alpha \cdot \mathbf{a}^* + \beta \cdot \mathbf{b}^* + \gamma \cdot \mathbf{c}^*$ for $GdCuAs_2$, $GdAuAs_2$ and $TbAuAs_2$ (β is zero by symmetry) [91].

	$GdCuAs_2$	$GdAuAs_2$	$TbAuAs_2$
α	0.04(1)	0.03(1)	0.02(1)
γ	0.48(1)	0.48(1)	0.46(1)

Refinement and characteristic structural features are discussed in detail for $TbAuAs_2$ in the following, differences of $GdCuAs_2$ and $GdAuAs_2$ are highlighted afterwards.

A section of the reciprocal layer $h\ 2\ l$ displays the area around the main reflection 0 2 0 in figure 5.3 (left). Two of the satellites can be attributed to the modulation vector **q** with $\alpha = 0.02(1)$ and $\gamma = 0.46(1)$ and **–q**, respectively. These satellites, 0 2 0 1 and 0 2 0 –1, are marked by solid lines. Obviously, two further satellites — indicated by dotted lines in the figure — are found around the main reflection 0 2 0, which can either be the result of a second modulation vector or of twinning of the crystal. As no cross terms, i. e. satellites attributed to the modulation vectors $\mathbf{q_1} + \mathbf{q_2}$ and $\mathbf{q_1} - \mathbf{q_2}$ with $\mathbf{q_1} = (\alpha 0 \gamma)$ and $\mathbf{q_2} = (-\alpha 0 \gamma)$ were detected, a two-dimensional modulation was excluded. Moreover the section of the reciprocal layer $h\ k$ 0.46, depicted in figure 5.3, right, shows a pattern of four satellite maxima, one being $h\ k\ l\ m$ = 0 2 0 1 again, emphasized by a black dot in the figure. This satellite pattern can only be the result of a multiple twin due to the loss of the fourfold axis in the course of the symmetry reduction, cf. paragraph below.

The structures have hence been refined as fourfold twins, the fractions of the twin components are presented in table 5.3.

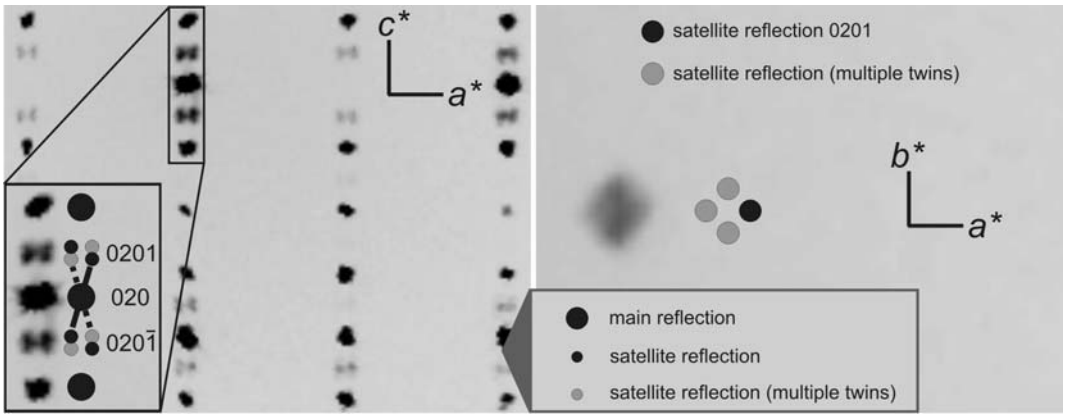

Figure 5.3: Satellite pattern in the diffraction image of $TbAuAs_2$, left: area around main reflection 0 2 0 (section of the reciprocal layer $h\ 2\ l$); right: satellite reflection 0 2 0 1 with satellites due to multiple twinning in a section of the reciprocal layer $h\ k$ 0.46.

Table 5.3: Twinning matrices **T** of the twinning laws $(h_n k_n l_n) = (h_1 k_1 l_1)\cdot\mathbf{T}$ and fractions of the twin components for $GdCuAs_2$, $GdAuAs_2$ and $TbAuAs_2$

T	$GdCuAs_2$	$GdAuAs_2$	$TbAuAs_2$
$\begin{vmatrix} 1 & 0 & 0 \\ 0 & 1 & 0 \\ 0 & 0 & 1 \end{vmatrix}$	0.091(6)	0.240(7)	0.170(5)
$\begin{vmatrix} 0 & \bar{1} & 0 \\ 1 & 0 & 0 \\ 0 & 0 & 1 \end{vmatrix}$	0.344(2)	0.195(2)	0.187(0)
$\begin{vmatrix} \bar{1} & 0 & 0 \\ 0 & \bar{1} & 0 \\ 0 & 0 & 1 \end{vmatrix}$	0.075(9)	0.387(8)	0.327(1)
$\begin{vmatrix} 0 & 1 & 0 \\ \bar{1} & 0 & 0 \\ 0 & 0 & 1 \end{vmatrix}$	0.488(4)	0.177(3)	0.315(4)

Since the modulation vector $\mathbf{q} = \alpha\cdot\mathbf{a}^* + \beta\cdot\mathbf{b}^* + \gamma\cdot\mathbf{c}^*$ with the observed translational parts $\alpha = 0.02(1)$ and $\gamma = 0.46(1)$ is incompatible with tetragonal or orthorhombic symmetry, the symmetry had to be reduced to the monoclinic crystal system. Due to the reflection conditions for the satellites, the monoclinic super space group $P12_1/m1(\alpha 0 \gamma)00$ (No. 11.1) [80] with $\beta = 90.0(3)$ ° was chosen for structure refinement. Based on the parent $HfCuSi_2$-type in space group $P4/nmm$ (No. 129) a three dimensional model in this superspace group was developed following the Bärnighausen formalism stated in figure 5.4 [78, 79]. The reduction in symmetry via two *translationengleiche* steps of index 2 reflects the loss of the fourfold axis. Note that the space group and the atomic positions of commensurately modulated $LnAgAs_2$ (*Ln* = Pr – Sm, Gd, Tb), $NdAuAs_2$ and $SmAuAs_2$ (chapter 4, figure 4.6) can be obtained in a similar way. The only difference lies in the last step of symmetry reduction from *Pmmn* (No. 59) to *Pmcn* (*Pnma*, No. 62) for $PrAgAs_2$ by a *klassengleiche* step of index 2 accompanied by the doubling of the *c*-axis for the commensurate superstructures.

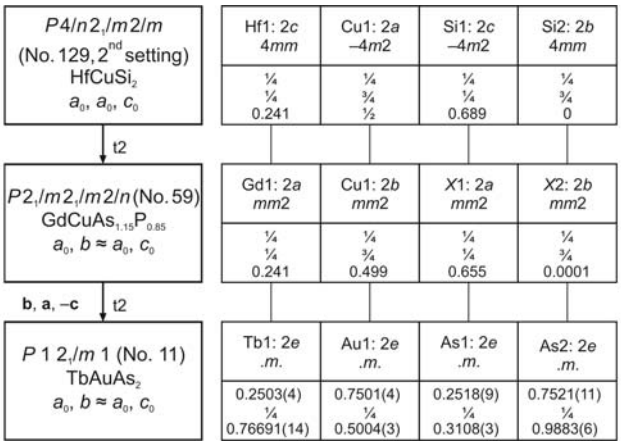

Figure 5.4: Bärnighausen tree for the symmetry relation between the $HfCuSi_2$ (*P*4/*nmm*) and the $TbAuAs_2$ structure ($12_1/m1$). Note that the atomic positions of the $HfCuSi_2$ type are shifted by $z+½$ with respect to the data given in the original publication [33].

In accordance with the results of the commensurate superstructure of the $LnTAs_2$ compounds (chapter 4), the displacement of the arsenic atoms of the planar layers was found to be the predominant effect of the modulation. One harmonic modulation wave for the positional modulation and for the displacement parameters of all atoms (higher modulation waves were not considered as only first order satellites were observed in the diffraction data) were introduced. The occupancy of the gold atoms was refined to 0.973(3) for $GdAuAs_2$ and 0.966(6) for $TbAuAs_2$, which led to a considerable drop in the *R*-values compared with full occupancies. No occupancy modulation was observed. Note that the gold deficiency has no impact on the distortion since stoichiometric $GdCuAs_2$ crystallizes with the same structural motives.

Transition metal deficiency in $HfCuSi_2$ related structures have also been found for some antimonides [37, 92]. The final results of the refinements as well as relevant crystallographic data, atomic parameters and interatomic distances are summarized in the data sheet for each compound in the annex.

The refined atomic positions are displayed within the respective Fourier maps in figure 5.5. Since the modulation is only visible along x_1, only the maps for x_1–x_4 are shown. As the As2 atoms are displaced along [100] resulting in the formation of zigzag chains with enlarged gaps between the chains, the distortion within the As layers also influences the other atoms as can be seen in the *t*-plots for *Ln*, *T* and As1 (figure 5.6; *t* is a real space coordinate associated with **q**). The formation of the As2 zigzag chains leads to enlarged voids between the chains causing a dislocation of the *Ln* atoms in the opposite direction along x_1 in turn. Transferred by the *Ln* atoms the As1 and *T* atoms of the PbO-like layers are shifted opposite to As2 along x_1 as well (figure 5.6).

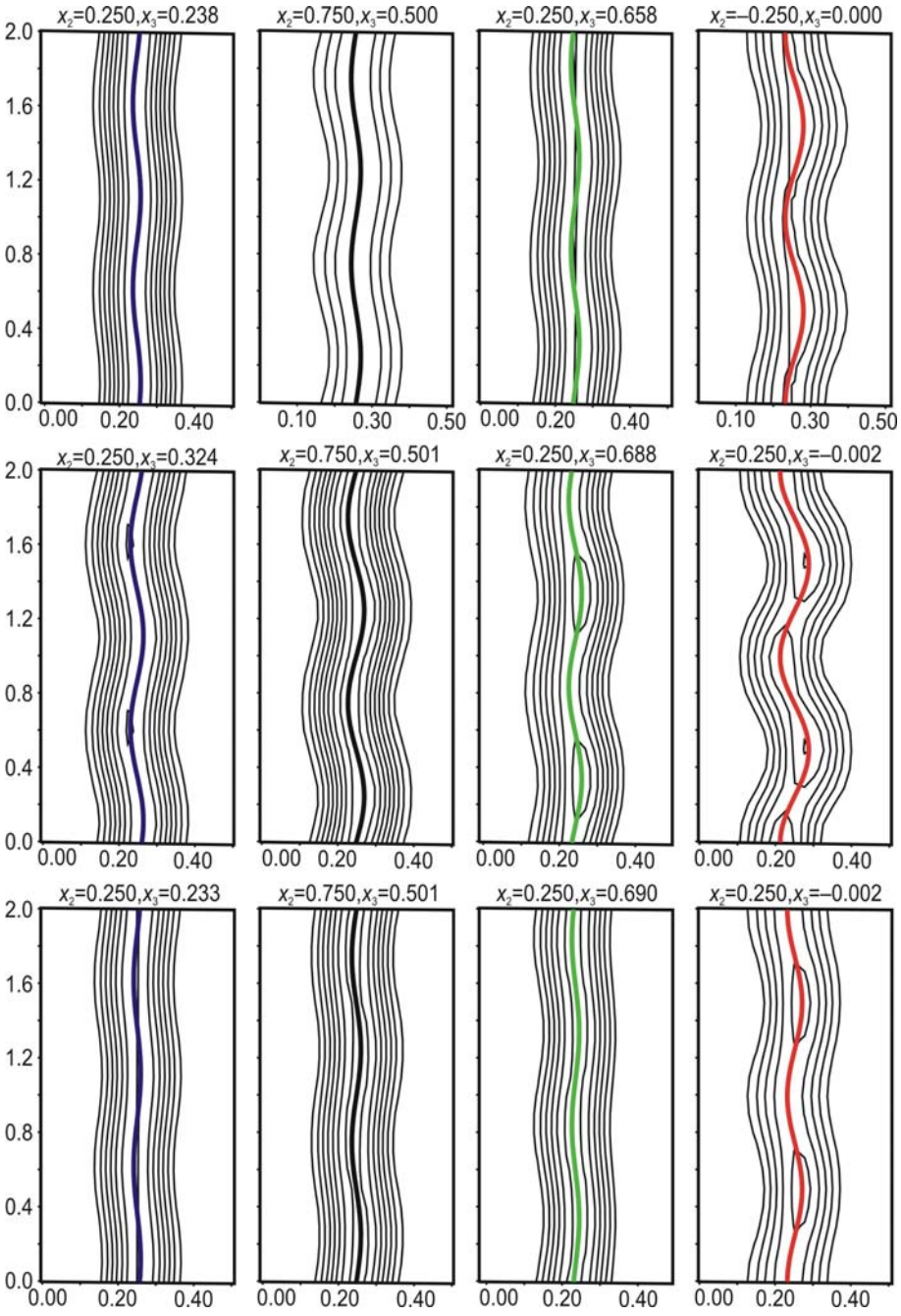

Figure 5.5: Fourier maps of the electron densities for $x_1 - x_4$ (x_1 corresponds to the crystallographic direction a and x_4 to the direction of **q**) for $GdCuAs_2$ (top), $GdAuAs_2$ (center) and $TbAuAs_2$ (bottom), bold lines: calculated atom positions for lanthanide metal (blue), coinage metal (black), As1 (green) and As2 (red); electron densities: 40 e^- per line for Gd, Tb, Au, 20 e^- per line for Cu, As.

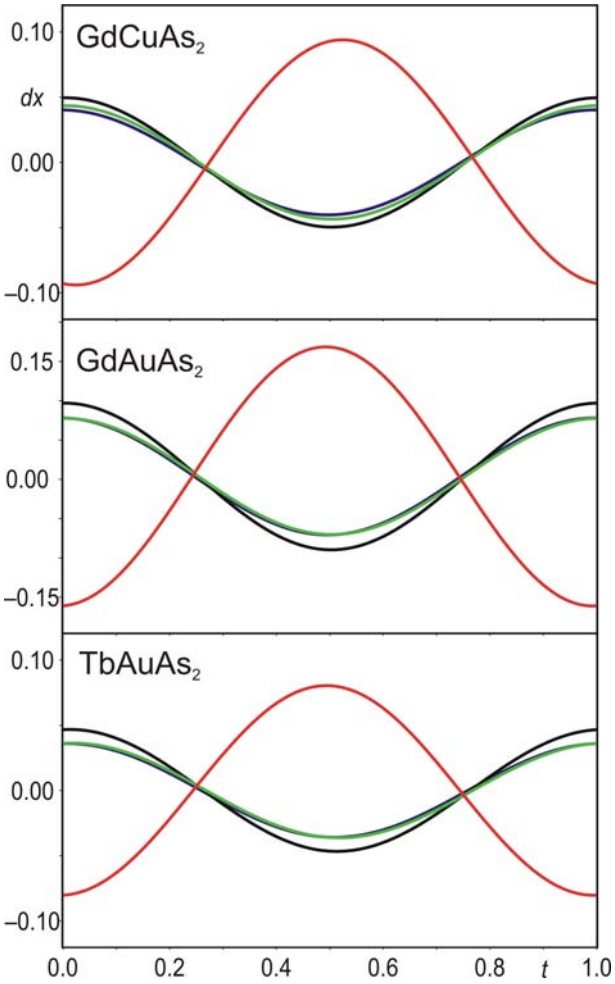

Figure 5.6: *t*-plot of the positional modulations (lanthanide metal blue lines, coinage metal black lines, As1 green lines, As2 red lines) along [001] for $GdCuAs_2$ (top), $GdAuAs_2$ (center) and $TbAuAs_2$ (bottom).

Choosing 2.828 Å as the upper limit to generate only two-bonded As2 atoms in $TbAuAs_2$, three different motives can be identified: zigzag chains in *in-phase* or in *anti-phase* orientation (*in-phase* orientation is defined as the orientation of the majority of the chains), and isolated As2 atoms on the border between *in-phase* and *anti-phase* chains.

For these motives, rod groups were determined according to International Tables Vol. E [93]. The propagation direction of the zigzag chains and consequently of the isolated As2 atoms is along [010]. Both zigzag chains and isolated As2 atoms possess monoclinic/rectangular symmetry, the zigzag chains have $p12_1/m1$ symmetry (No. 12, left in figure 5.7) whereas the row of isolated atoms comprises $p12/m1$ symmetry (No. 11, right in figure 5.7).

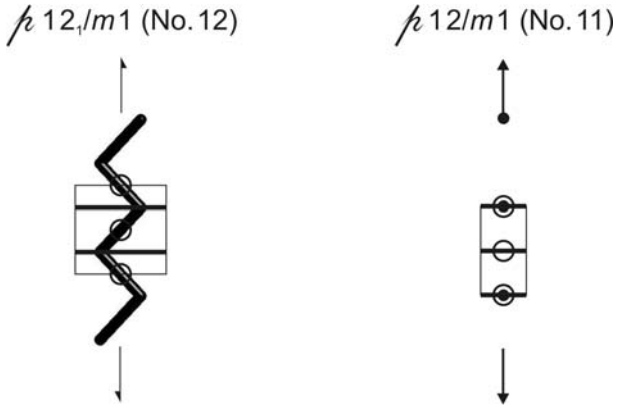

Figure 5.7: Rod groups of the different motives: zigzag chains in rod group $p12_1/m1$ (No. 12, left) and isolated atoms in rod group $p12/m1$ (No. 11, right), both monoclinic/rectangular.

For $TbAuAs_2$, the As2–As2 intrachain distances vary between 2.719(6) Å and 2.828(1) Å as a result of the positional modulation. The blocks of the majority case contain 26 *in-phase* chains of the same orientation (purple in figure 5.8), whereas those of the minority case contain 23 chains with an *anti-phase* orientation (shift by $\Delta y = 0.5$, green) with respect to those of the majority blocks. The different blocks are, due to the modulation, alternately arranged and separated by isolated As2 atoms. This centrosymmetric layer exhibits orthorhombic layer group symmetry $p2/b2_1/m2/m$ (No. 40, figure 5.8).

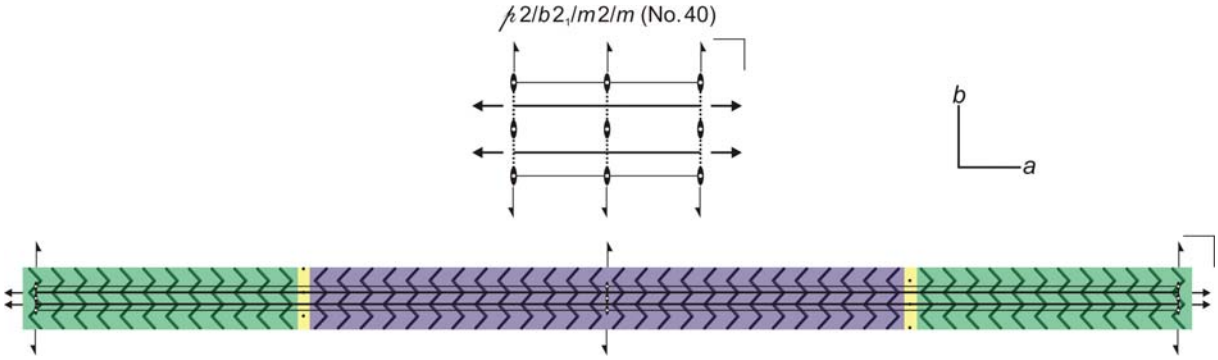

Figure 5.8: Top: sketch of layer group $p2/b2_1/m2/m$ (No. 40), bottom: layer group $p2/b2_1/m2/m$ applied to the structure.

Looking on a larger section of the modulated structure another level of hierarchy becomes visible (figure 5.9). The layers exhibit a periodicity of $a_l = 50\ a_b$ (cf. figure 5.8), which are identical with the above presented layer group in this case. The layers are stacked along [001] with an offset of $\Delta a_b = 23$ basic unit cells. Along [010], twofold screw axes are located in the center of each block. Additional twofold rotation axes are shifted by $\Delta a = 11.5 a_b$ and $\Delta c = 0.5 c_b$ (cf. figure 5.8) relative to those in the center of the blocks. In accordance with these symmetry operations, the periodic tiling of the modulated structure in a monoclinic

super-cell with space group $P12_1/m1$ and $a' = 25.66$ Å, $b' = 4.089$ Å, $c' = 77.78$ Å and $\beta' = 92.84$ ° can be modeled (black lines in figure 5.9).

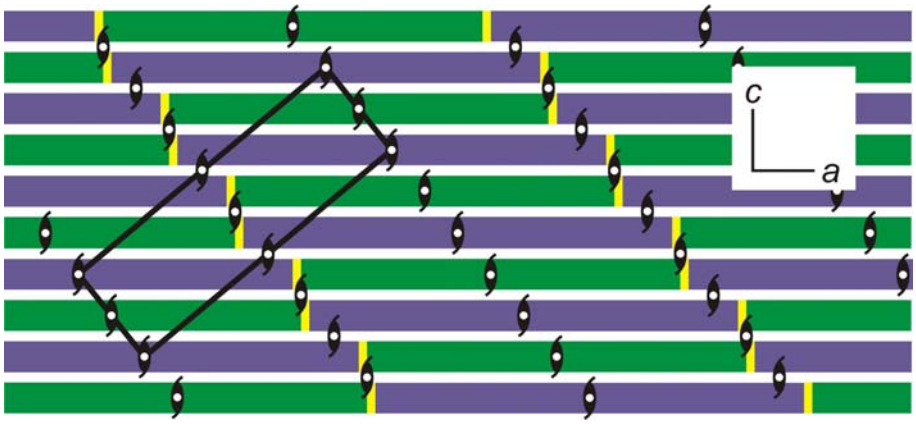

Figure 5.9: Section of the structure of $TbAuAs_2$, view along [010], color code according to figure 5.8. The positions of the twofold screw axes are highlighted, the approximant ($a' = 25.66$ Å, $b' = 4.089$ Å, $c' = 77.78$ Å, $\beta' = 92.84$ °) is emphasized with bold black lines.

The modulation of $GdCuAs_2$ (figure 5.10) is more difficult to describe since blocks of different widths with the same orientation are found. The As2–As2 intra-chain distances vary between 2.593(7) Å and 2.751(8) Å.

Choosing 2.751 Å as the upper limit for two-bonded As2, the chains are grouped in four blocks of different width and orientation always separated by isolated As2 atoms. Two different sequences (layers) can be identified with $a_1 = 28\ a$ for both. This is achieved by the combination of the block consisting of 16 *in-phase* chains (purple in figure 5.10) and the block formed by eleven *anti-phase* chains (green) separated by isolated As2 atoms (yellow) (layer A), or the combination of the block consisting of 15 *in-phase* chains (blue) and the block set up of 12 *anti-phase* chains (red) separated by isolated As2 atoms (layer B). Both layers exhibit orthorhombic layer group symmetry $p2/b2_1/m2/m$ (No. 40, figure 5.10).

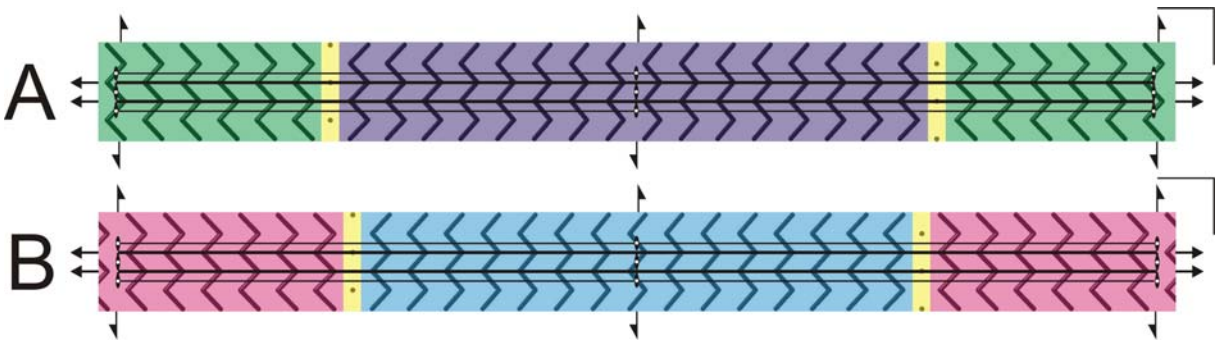

Figure 5.10: Layer group $p2/b2_1/m2/m$ (No. 40) applied to the two layers of $GdCuAs_2$. Top: layer A consisting of 16 *in-phase* chains and eleven *anti-phase* chains, bottom: layer B containing 15 *in-phase* chains and 12 *anti-phase* chains.

For $GdAuAs_2$, the As2–As2 intra-chain distances vary between 2.631(5) Å and 2.822(2) Å. The same blocks as in $GdCuAs_2$ are observed, however grouped into one single type of layer with $a_r = 100\ a$. The layer group is $p2/b2_1/m2/m$ (No. 40, figure 5.11) again.

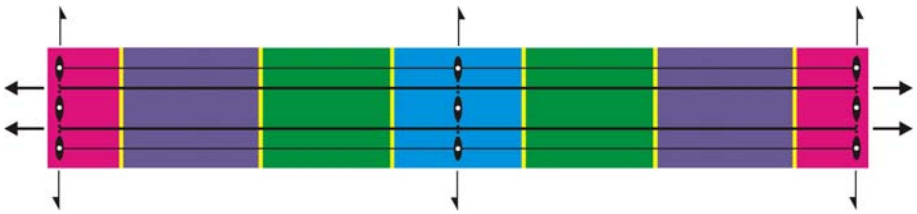

Figure 5.11: Layer group $p2/b2_1/m2/m$ (No. 40) applied to the layer of $GdAuAs_2$. For explanation of the blocks, see text.

The view on a larger section of the modulated structure of $GdCuAs_2$ reveals that the approximant is formed by four layers A and one layer B (figure 5.12). The periodic tiling of the modulated structure can be modeled with a monoclinic approximant (bold black lines in figure 5.12) with space group $P12_1/m1$ and $a' = 65.56$ Å, $b' = 3.9016$ Å, $c' = 82.82$ Å and $\beta' = 94.18$ °.

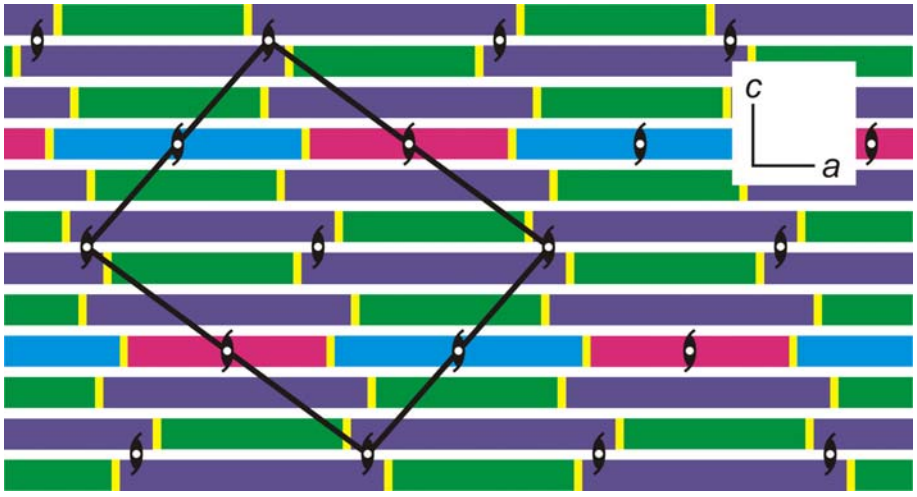

Figure 5.12: Section of the structure of $GdCuAs_2$, view along [010], color code according to figure 5.10. The positions of the twofold screw axes are highlighted, the approximant ($a' = 65.56$ Å, $b' = 3.9016$ Å, $c' = 82.82$ Å, $\beta' = 94.18$ °) is emphasized with bold black lines.

For $GdAuAs_2$, the layers with 100 basic unit cells along [100] are stacked along [001] with an offset of 18 chains. According to a monoclinic super-cell approximant (bold black lines in figure 5.13) with space group $P12_1/m1$ and $a' = 62.84$ Å, $b' = 4.060$ Å, $c' = 64.12$ Å and $\beta' = 95.49$ °, the periodic tiling of the modulated structure can be modeled for this compounds.

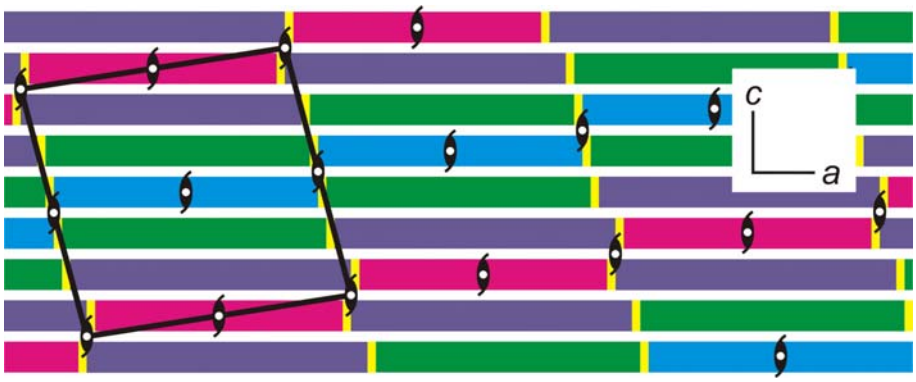

Figure 5.13: Section of the structure of $GdAuAs_2$, view along [010], color code according to figure 5.11. The positions of the twofold screw axes are highlighted, the approximant ($a' = 62.84$ Å, $b' = 4.060$ Å, $c' = 64.12$ Å, $\beta' = 95.49$ °) is emphasized with bold black lines.

The final results of the refinements, relevant crystallographic data as well as interatomic distances, Wyckoff positions, atomic coordinates, displacement parameters of both the average and modulated structures can be found in the crystallographic data sheets of the respective compounds in the annex.

5.2 Other Incommensurately Modulated Cu Compounds

Satellite reflections indicating incommensurately modulated structures were also found for $CeCuAs_2$, $NdCuAs_2$, $SmCuAs_2$, $TbCuAs_2$ and $HoCuAs_2$ (table 5.4). Since this work is focused on $LnAgAs_2$ and $LnAuAs_2$ compounds, structure models are presented for $LaCuAs_2$ (chapter 4) and $GdCuAs_2$ (chapter 5.1), only.

Table 5.4: Translational parts α and γ of the modulation vector $\mathbf{q} = (\alpha 0 \gamma)$ for $CeCuAs_2$, $NdCuAs_2$, $SmCuAs_2$, $TbCuAs_2$ and $HoCuAs_2$

	$CeCuAs_2$	$NdCuAs_2$	$SmCuAs_2$	$TbCuAs_2$	$HoCuAs_2$
α	0.054(8)	0.036(2)	0.012(4)	0.028(3)	0.035(5)
γ	0.475(2)	0.462(6)	0.479(1)	0.473(7)	0.286(7)

5.3 $CeAu_{1-\delta}As_2$

Note: The title compound was obtained in the composition $CeAu_{0.986(2)}As_2$. To improve the readability in the text, it is denominated as $CeAuAs_2$ in the text. The crystallographic tables in the annex contain the proper composition.

5.3.1 Powder Pattern

The X-ray powder diffraction pattern of $CeAuAs_2$ is shown in figure 5.14. The lines represent the calculated peaks based on the three-dimensional basic structure model in space group $P12_1/m1$ (No. 11), which has been deduced as average space group. Additional diffraction maxima that could be attributed to by-products were detected. A careful examination shows a broadening of some reflections at higher diffraction angles, e.g. reflections 040 and 400 at $2\theta \approx 64\,°$ or reflections 242 and 422 at $2\theta \approx 75\,°$. This is as a strong indication for an orthorhombic distortion of the tetragonal cell of the aristotype at least. The lattice parameters at 293(2) K have been determined to $a = 5.804(1)$ Å, $b = 5.814(1)$ Å, $c = 10.179(1)$ Å from powder data.

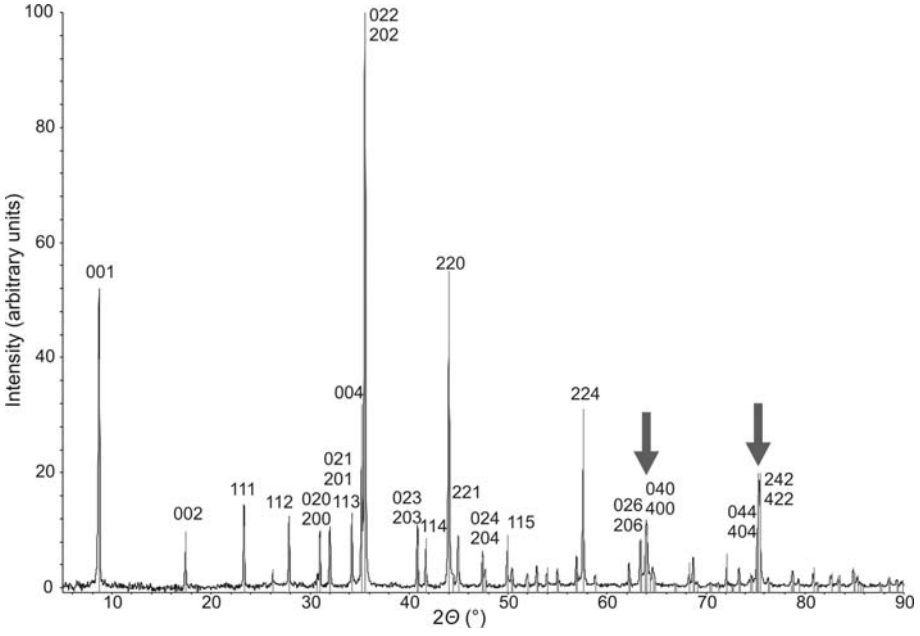

Figure 5.14: X-ray powder diffraction pattern of $CeAuAs_2$ (black) with calculated peaks according to the basic structure in space group $P12_1/m1$ (No. 11). The arrows indicate the broadened reflection 040/ 400 and 242/ 422.

5.3.2 Average Structure

Precession photographs of $CeAuAs_2$ revealed a (pseudo-)tetragonal unit cell with $a \approx b \approx 5.8$ Å and $c \approx 10$ Å. The satellite reflections were visible as blurred spots only. According to the reflection conditions and the symmetry of the main reflections, the orthorhombic space group *Cmme* (No. 67) was deduced for the average structure. Based on single-crystal diffraction data a structure model of the average structure was developed. PbO-like layers consisting of square nets of the Au atoms, alternately capped by As1 atoms, as well as planar square nets of As3 atoms are stacked along [001]. The Ce atoms occupy positions between these two building blocks. The average structure of $CeAuAs_2$ in *Cmme* is shown in figure 5.15. The lattice parameters of $a = 5.803(1)$Å, $b = 5.813(1)$ Å and $c = 10.179(1)$ Å are in good agreement with those determined from powder data.

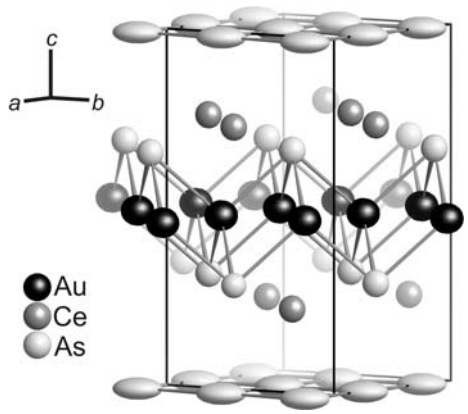

Figure 5.15: Average structure for $CeAuAs_2$ in *Cmme* (No. 67), ellipsoids at the 99% probability level.

The Wyckoff positions, atomic coordinates and displacement parameters of the average structure of $CeAuAs_2$ are summarized in the respective data sheet in the annex. The quite large anisotropic displacement parameters of the As3 atoms can be taken as the result of the modulation.

5.3.3 Modulated Structure

Reciprocal layers, simulated from the diffractometer data sets, revealed satellites of low intensities in reciprocal layers $l \pm 0.39$. Due to the position of the additional reflections and a constant splitting of their intensity maxima (figure 5.16), commensurate superstructures and twinning of 3D structures can be excluded as reasons for the additional reflections. In fact, we deal with an incommensurate modulation again.

A section of the reciprocal layer $h\ 2\ l$ displays the area around the main reflection 4 2 1 in figure 5.16 (left). Two of the satellites can be attributed to the modulation vector **q** and –**q**, respectively. The translational parts of **q** were refined to $\alpha = 0.08(1)$ and $\gamma = 0.39(1)$, respectively [91]. These satellites, 4 2 1 1 and 4 2 1 –1, are marked by solid lines. Obviously, two further satellites, indicated by dotted lines, are found around the main reflection 4 2 1, which can either be the result of a second modulation vector or of twinning of the crystal. As no cross terms, i. e. satellites attributed to the modulation vectors $\mathbf{q_1} + \mathbf{q_2}$ and $\mathbf{q_1} - \mathbf{q_2}$ with $\mathbf{q_1} = (\alpha 0 \gamma)$ and $\mathbf{q_2} = (-\alpha 0 \gamma)$ were detected, a two-dimensional modulation can be excluded. Moreover the section of the reciprocal layer $h\ k$ 1.39, depicted right in figure 5.16, shows a pattern of four satellite maxima, one being 4 2 1 1 again (emphasized by a black dot in the figure). This satellite pattern can only be the result of multiple twinning due to the loss of the fourfold axis in the course of the symmetry reduction, cf. paragraph below.

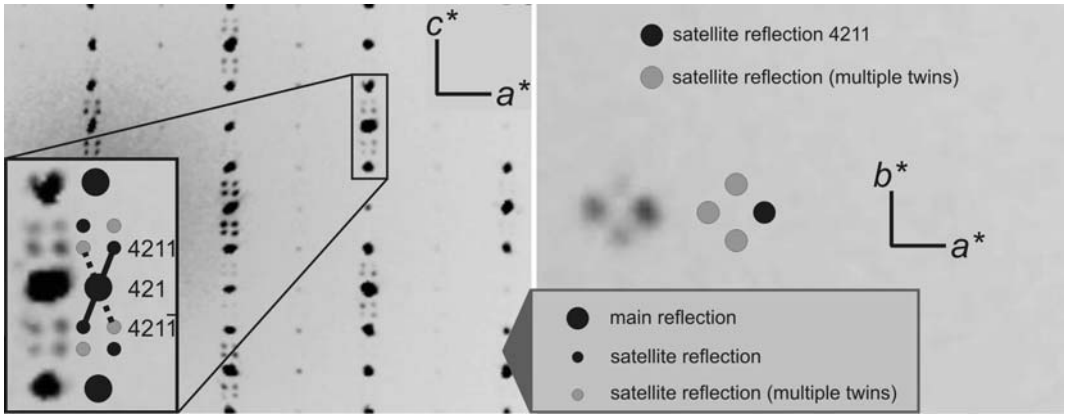

Figure 5.16: Satellite pattern in the diffraction image of $CeAuAs_2$, left: area around main reflection 4 2 1 (section of the reciprocal layer $h\ 2\ l$); right: satellite reflection 4 2 1 1 with satellites due to multiple twinning in a section of the reciprocal layer $h\ k$ 1.39.

The structure has hence been refined as a fourfold twin. However, due to correlations in the refinement, it was necessary to keep the twin fractions fixed during the refinement procedure. The twin fractions given in table 3 were determined during several runs by assuming arbitrary values and keeping them fixed. The goodness of the fits was judged be respective *R*-factors, the best fit was obtained with twin fractions 0.052, 0.451, 0.029 and 0.468.

As can also be seen from figure 5.16, some of the main reflections show anomalies, like a tendency to splitting or streaking. The origin is not yet clear, but an explanation might be that the crystals undergo several phase transitions upon cooling from 1123 K to room temperature, which leads to twinning, anti-phase domains and hence mechanical stress. Upon cooling the crystals below room temperature on the diffractometer, the splitting of some main reflections becomes more pronounced. This is taken as further evidence for this assumption.

Since the modulation wave vector **q** = 0.08(1) **a*** +0.39(1) **c*** is incompatible with tetragonal or orthorhombic symmetry, the symmetry had to be reduced to the monoclinic crystal system. Due to the reflection conditions for the satellites, the monoclinic super-space group $P12_1/m1(\alpha 0\gamma)00$ (No. 11.1) with $\beta = 90.09(8)°$ was chosen for structure refinement. Note, that the same superspace group symmetry has been found for the incommensurately modulated compounds $GdCuAs_2$, $GdAuAs_2$ and $TbAuAs_2$ (cf. chapter 5.1), although both types of modulated structures differ substantially in their structural motives.

Based on the parent $HfCuSi_2$ type structure in space group *P*4/*nmm* (No. 129) a three dimensional model in this superspace group was developed following the Bärnighausen formalism stated in figure 5.17. The reduction in symmetry via two *translationengleiche* and one *klassengleiche* steps of index 2 reflects the $\sqrt{2}\cdot\sqrt{2}$ superstructure in the first step, the loss of the *C*-centering in the second, and the removal of mirror planes in the last. Note, that the space group and the atomic positions of commensurately modulated $CeAgAs_2$ [24] can be obtained in a similar way.

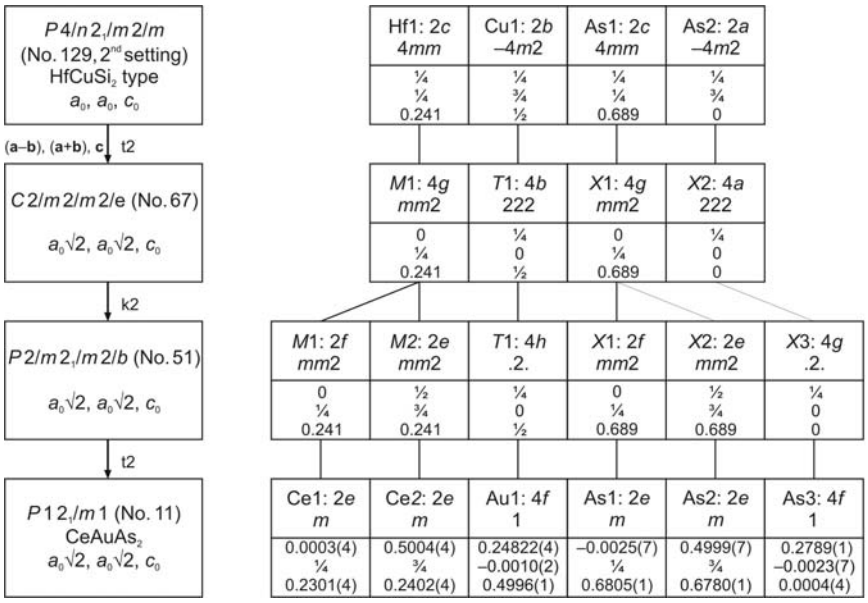

Figure 5.17: Bärnighausen tree for the symmetry reduction from *P*4/*nmm* to $P12_1/m1$, note that the atomic positions of the $HfCuSi_2$ type are shifted by (z+½) with respect to the data given in the original publication [33]; atomic coordinates of $CeAuAs_2$ as results of the structure refinement.

In accordance with the results of the commensurate superstructure of $CeAgAs_2$, the displacement of the As3 atoms was found to be the predominant effect of the modulation. After introduction of one harmonic modulation wave for the positional modulation and the displacement parameters of all atoms (higher modulation waves were not considered as only first order satellites were observed in the diffraction data), the Fourier maps around the Au

atom indicated a modulation of the electron density distribution for this site as well. Consequently, a harmonic occupancy modulation wave was introduced for the Au atom, which led to a considerable drop in the *R*-values. The Au occupancy was refined to 0.986(2). Transition metal deficiency in $HfCuSi_2$ related structures have also been found for some antimonides [37, 92]. No occupancy modulations have been observed for the Ce and As atoms. The final results of the refinements as well as relevant crystallographic data, atomic parameters and interatomic distances are listed in the data sheet of $CeAuAs_2$ in the annex.

The refined atomic positions are displayed within the respective Fourier maps in figure 5.18. As can clearly be seen from these maps, the As3 atoms are mainly displaced in [010] resulting in the formation of cis-trans chains with enlarged gaps between the chains. The distortion within the arsenic layers also influences the other atoms as can be seen in the *t*-plots (*t* is a real space coordinate associated with **q**, figure 5.19) for Ce1, Ce2, Au, As1 and As2. The positional modulation of the As3 atoms along x_2 causes a dislocation of the Ce atoms along x_1 and — transferred by the latter — the As1, As2 and Au atoms of the PbO-like layers along x_1 as well.

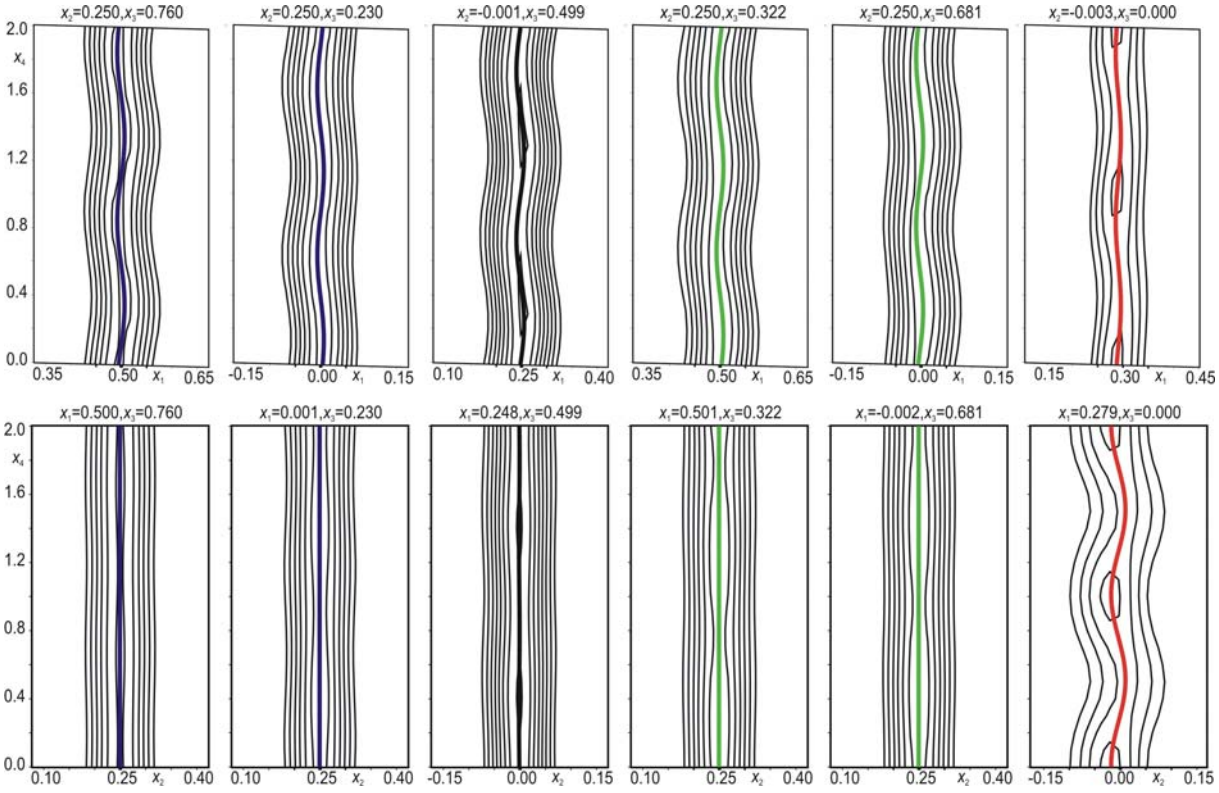

Figure 5.18: Fourier maps $x_1 - x_4$ (top) and $x_2 - x_4$ (bottom), bold lines: calculated atom positions (left to right) for Ce1, Ce2 (both blue), Au (black), As1, As2 (both green) and As3 (red); steps of electron densities 40 $e^-/Å^3$ per line for Ce, Au, 20 $e^-/Å^3$ per line for As.

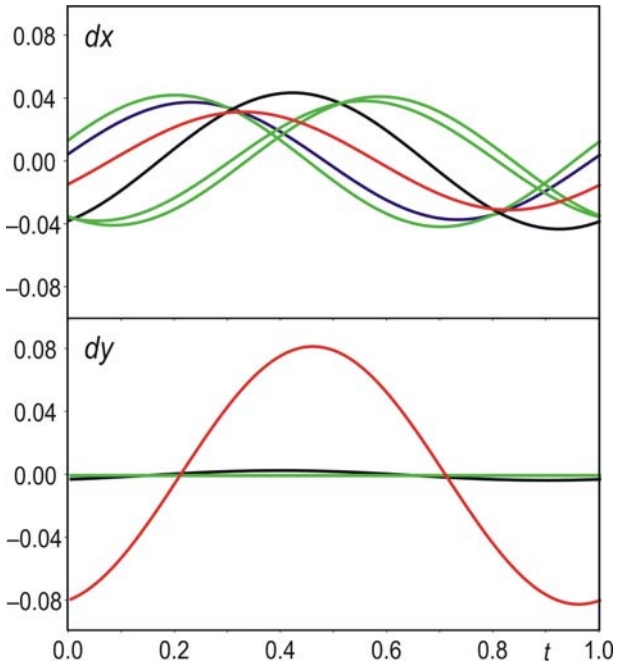

Figure 5.19: *t*-plots of the positional modulations for $CeAuAs_2$ (Ce blue lines, Au black line, As1 and As2 green lines, As3 red line) along [100] (*dx*) and [010] (*dy*).

Due to contributions of α and γ of the **q**-vector, the modulation has effects along [100] as well as along [001]. As has been mentioned above, the primary result of the modulation is the formation of cis-trans chains of As3 atoms running along [010]. The As3–As3 intra-chain distances change from about 2.528(1) Å to 2.616(1) Å along [100], and 2.716(2) Å to 2.906(2) Å along [010] as a result of the positional modulation.

Choosing 2.907 Å as the upper limit for two-bonded As3 atoms, three different motives can be identified: cis-trans chains in *in-phase* or in *anti-phase* orientation (*in-phase* orientation is defined as the orientation of the chains of the majority case), and As_4 rectangles on the border between *in-phase* and *anti-phase* chains. The rod groups of these motives were determined according to International Tables Vol. E [93]. The propagation direction of the cis-trans chains and consequently the long edges of the rectangles are along [010]. The chains comprise monoclinic/rectangular $p12_1/m1$ (No. 12) symmetry whereas the rectangles possess orthorhombic $p2/m2/m2/m$ (No. 20) symmetry, cf. figure 5.20.

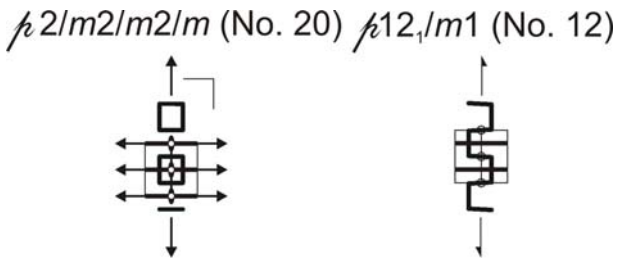

Figure 5.20: Rod groups of the different motives: rectangles in rod group $p2/m2/m2/m$ (No. 20, left) and cis-trans chains in rod group $p12_1/m1$ (No. 12, right)

The cis-trans chains are grouped in blocks of different length: Blocks consisting of seven (blue in figure 5.21) or six (grey) chains in *in-phase* orientation, and six (green) or five (red) chains in *anti-phase* orientation are found. The modulation of the As3–As3 intrachain distances causes also a sudden change between the majority and the minority blocks at the border of the blocks. As explained above, the direct *in-phase – anti-phase* change is mediated in some cases by a row of rectangles of As3 atoms. The sequence of the blocks forms a complicated pattern.

Four different arrangements with 25 basic unit cells along [100] (hereafter denominated as layers, figure 5.21) were identified. Since layer $\overline{\text{B}}$ reveals the same sequence but the inverse order of B, only layer B is shown in the figure. The centro-symmetric layers A and C exhibit orthorhombic layer group symmetry $p2_1/m2/a2/m$ (No. 40), whereas the acentric layers B and $\overline{\text{B}}$ reveal monoclinic/rectangular symmetry $p1m1$ (No. 11).

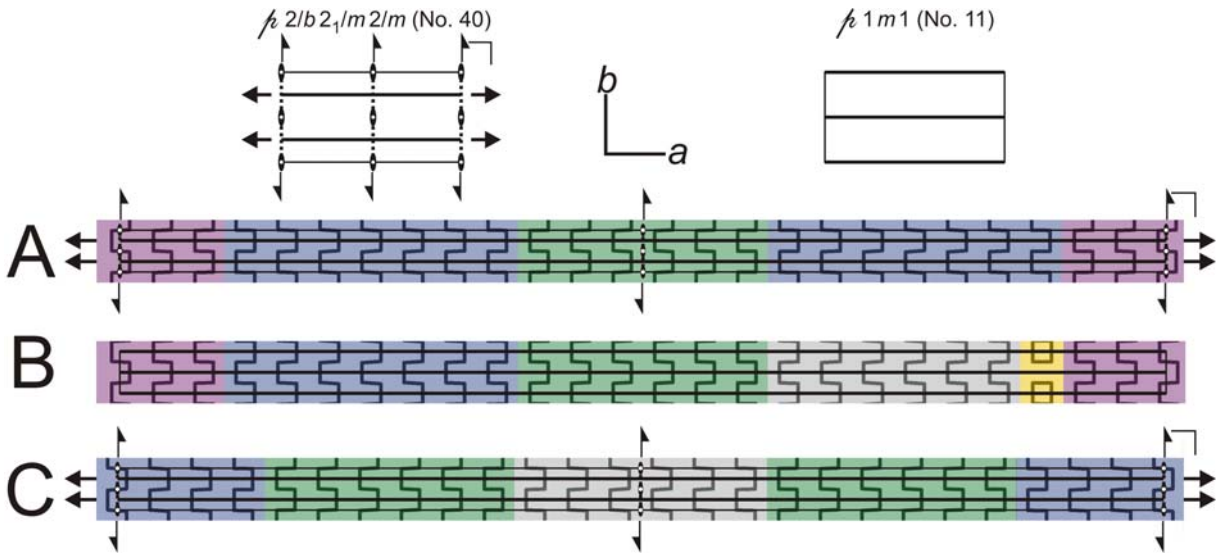

Figure 5.21: Top: sketches of the different layer groups: left: $p2/b2_1/m2/m$ (No. 40), right: $p1m1$. Bottom: layers A, B and C – layers A and C possess $p2/b2_1/m2/m$ symmetry, B and $\overline{\text{B}}$ (not shown; inverse sequence of layer B along *a*) $p1m1$ symmetry. The orthorhombic symmetry is broken due to the rectangles (averaged cis-trans chains of *in-phase* and *anti-phase* orientation).

Looking on a larger section of the modulated structure, another level of hierarchy becomes visible (figure 5.22). The layers are grouped in a monoclinic super-cell with $a' = 25\ a_b$, $b' = 1\ b_b$, $c' = 18\ c_b$ and $\beta' = \beta_b$. This approximant consists of 13 layers A, two layers B, two layers $\overline{B}$ and one layer C, which are arranged in the sequence $CAAABAA\overline{B}AAABAA\overline{B}AAA$. The different layers are shifted along [100] for either $-5a_0$ or $+8a_0$.

Like the basic structure, the approximant has the symmetry of space group $P12_1/m1$ (No. 11). The number of *anti-phase* chains in the minority blocks divided by the number of *in-phase* chains tends to the value of 0.39 and hence reflects the value of γ of the modulation vector.

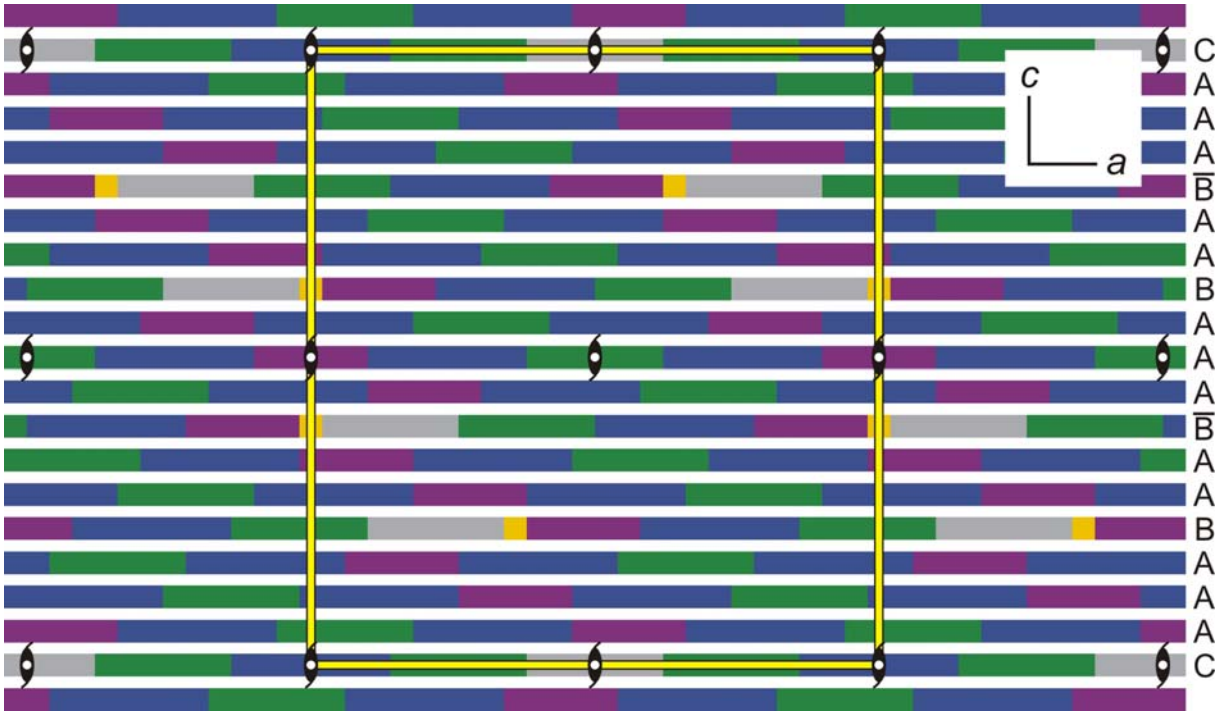

Figure 5.22: The approximant (projection along [010]) of $CeAuAs_2$ consists of $25 \times 1 \times 18$ basic unit cells and contains 13 layers A, two layers B, two layers $\overline{B}$ and one layer C stacked in the sequence $CAAABAA\overline{B}AAABAA\overline{B}AAA$. The screw axes and centers of symmetry of space group $P12_1/m1$ are emphasized.

The final results of the refinements, relevant crystallographic data as well as interatomic distances, Wyckoff positions, atomic coordinates, displacement parameters of both the average and modulated structure can be found in the crystallographic data sheet of $CeAuAs_2$ in the annex.

6 Determination of Physical Properties

6.1 Conductivity and Band Structure Calculation

The electrical conductivity of a number of isostructural *Ln*$AgAs_2$ and *Ln*$AuAs_2$ compounds gives an impression of the influence of the crystal or electronic structure on the macroscopic properties. The character of conductivity varies from metallic to (small gap) semiconducting. Therefore the resistivity curves of $CeAgAs_2$, $CeAuAs_2$ and $PrAgAs_2$ were measured (figures 6.1 – 6.3). This selection is mainly motivated by the special behavior of $CeCuAs_2$, for which semiconducting behavior connected with a partial Kondo character of the Ce^{3+} ion was reported in contrast to a metallic character of all other *Ln*$CuAs_2$ compounds [92]. In this study, $CeAgAs_2$ and $CeAuAs_2$ (figures 6.1 and 6.2) are characterized by a negative temperature coefficient of the resistivity. This behavior is in contrast to data found in literature [26], which show an increase with the temperature. Nevertheless, it agrees well with the reported properties of $CeCuAs_2$. Taking into account the thermal activation of charges, following the Boltzmann factor as dominant process for the temperature dependence of resistivity, i.e. $\rho \propto \exp(E_g/2kT)$, the gap energy can be estimated. The $\rho(T^{-1})$ curves are presented as insets of figures 6.1 and 6.2. Both compounds are intrinsic semiconductors, their gaps are rather small and depend strongly on the temperature (1 meV at low temperatures and 60 meV at high temperatures for $CeAgAs_2$, 0.2 meV at low temperatures and 8 meV at high temperatures for $CeAuAs_2$). The absolute values of the resistivity are, especially in the case of $CeAuAs_2$, small, too. This is an indication for a more or less indifferent character of electrical transport near a change to a metallic system. Additionally, the small kink in the resistivity curve of $CeAuAs_2$ at $T \approx 100$ K may indicate a structural change as proposed in [26]. The properties of grain boundaries in the investigated pellets may influence the measured resistivity values.

The conductivity of two silver compounds increase linearly with increasing temperature indicating metallic behavior for $PrAgAs_2$ (figure 6.3). This behavior is most probably of general character for the *Ln*$AgAs_2$ compounds (except $LaAgAs_2$ and $CeAgAs_2$) and comparable to the *Ln*$CuAs_2$ compounds [92].

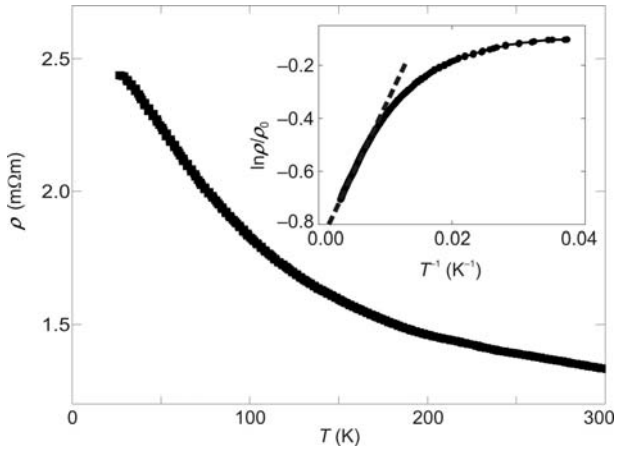

Figure 6.1: Temperature dependence of the electrical resistivity of polycrystalline $CeAgAs_2$. The data are an average of one cooling and one heating run (no hysteresis). The inset shows the logarithmic behavior in order to analyze energy scales.

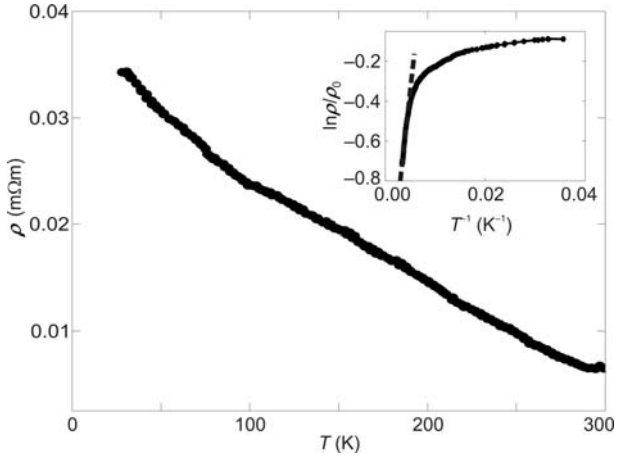

Figure 6.2: Temperature dependence of the electrical resistivity of polycrystalline $CeAuAs_2$. The data are an average of one cooling and one heating run (no hysteresis). The inset shows the logarithmic behavior in order to analyze energy scales.

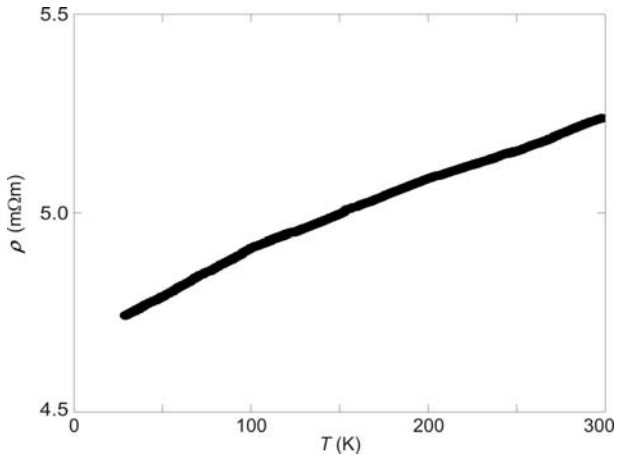

Figure 6.3: Temperature dependence of the electrical resistivity of polycrystalline $PrAgAs_2$. The data are an average of one cooling and one heating run (no hysteresis) and show a linear change with temperature.

Both total (grey area) and partial (black and grey lines) calculated electronic densities of states (DOS) of $LaAgAs_2$ (representative for a fourfold superstructure with cis-trans chains) and $PrAgAs_2$ (representing a twofold superstructure with zigzag chains) are presented in figure 6.4. The computed valence DOS is similar for both compounds, although the DOS for $LaAgAs_2$ is more structured due to the additional band splitting caused by the As distortion. Contrary to the experimental observation, both compounds should exhibit metallic behavior. On the other hand, a low DOS (pseudo gap) is found at the Fermi level for both compounds. The pseudo gap for $LaAgAs_2$ is a little more pronounced compared to the Pr system, reflecting the small additional lattice distortion. At the Fermi level, mainly contributions from As 4*p* electrons are found. The Ag 4*d* shell is mostly filled and rather low in energy (between –6 eV and –4 eV).

The band structures for both systems are shown in figure 6.5. Like in the DOS, the strong similarity of the compounds is reflected in their band structure. Since Pr has magnetic moments due to unpaired 4*f* electrons, the bands are spin split (solid and dotted lines). Due to the localized character of the 4*f* electrons, this spin splitting is very small and negligible with respect to the band dispersion.

The presented measured resistivity data can be understood in connection to the crystal structure and the electronic band structure. Probably, the semiconducting behavior is favored in the *Pmca* compounds with cis-trans chains of As atoms, whereas the *Pmcn* systems with As zigzag chains exhibit metallic conductivity. The results of the band structure calculations show that mainly the As states contribute to the (small) density of states at the Fermi level. In connection with the fact that the interatomic As–As distances within the chains are small, it can be concluded that the electronic transport is favored along the As chains. The character and size of the rare-earth ions influence the transport properties.

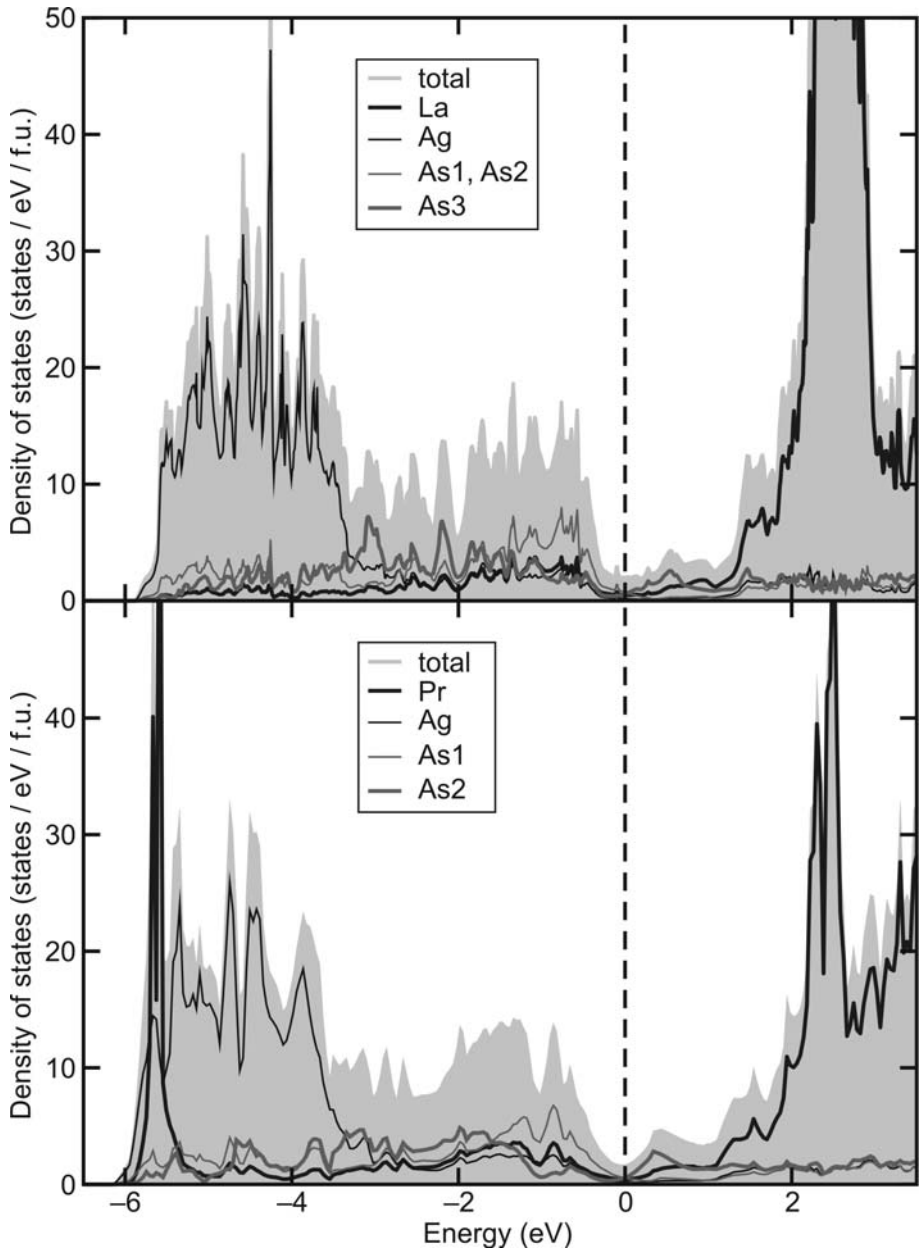

Figure 6.4: Total and partial electronic DOS for $LaAgAs_2$ (upper panel) and $PrAgAs_2$ (lower panel). The Fermi level is set to zero.

In the DOS curves, the main difference between the two compounds $LaAgAs_2$ and $PrAgAs_2$ concerns the 4*f* contribution. In both compounds, the unoccupied 4*f* states are found at about 2.5 eV, whereas the occupied 4*f* states of Pr are at about –5.5 eV. This is consistent with the applied *U* of 8 eV, which should be a measure for the split between the occupied and the unoccupied the 4*f* states.

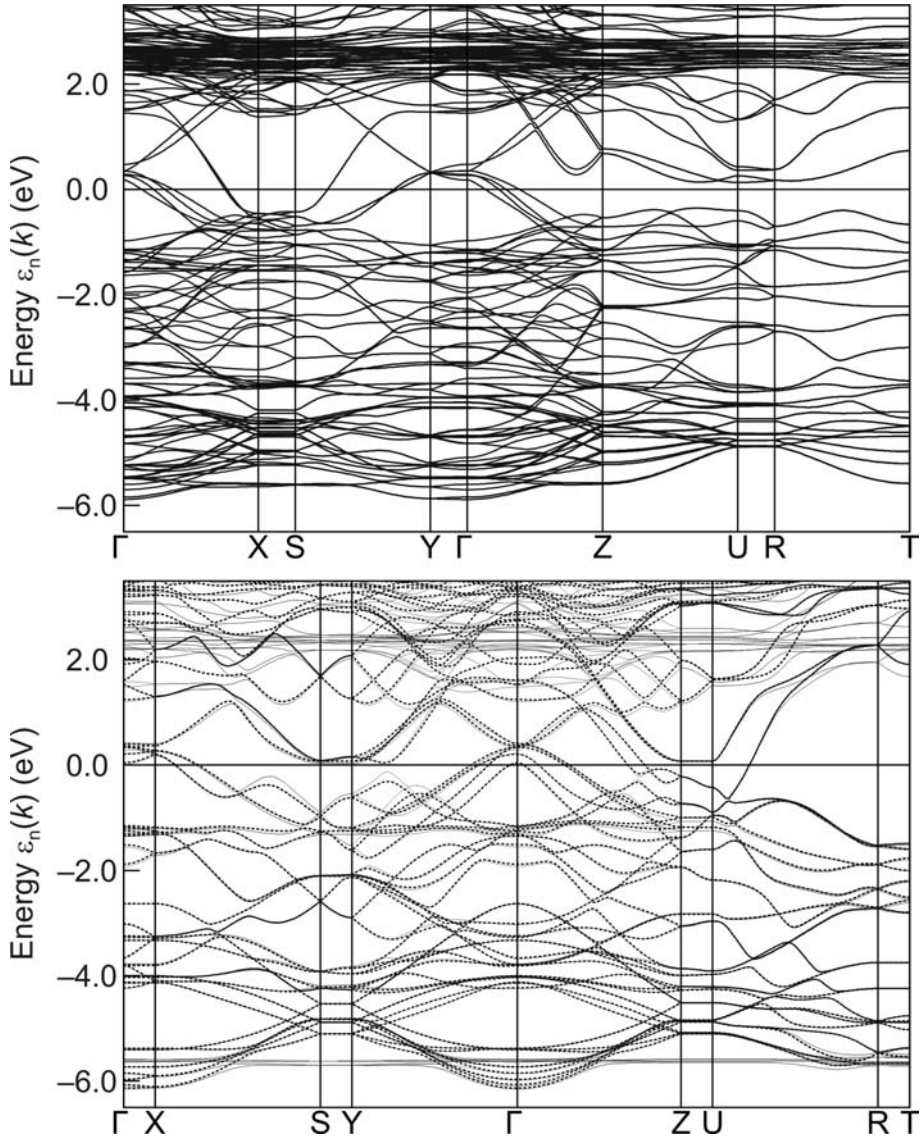

Figure 6.5: Band structure of $LaAgAs_2$ (upper panel) and $PrAgAs_2$ (lower panel). For $PrAgAs_2$, the two spin directions are indicated by full and dashed lines, respectively. The Fermi level is set to zero.

For the band structures, the bands crossing the Fermi level and being responsible for the metallic character have a typical band width of about 2 eV. This rather large band width is most likely also the reason, why no insulating behavior despite the additional lattice distortion is found for the La compound. Only in one part of the *k*-space, between Z and T (figure 6.5), the bands split around the Fermi level.

6.2 Magnetization Experiments

All compounds obtained as single-phase samples (LnAgAs$_2$ with Ln = La, Ce – Nd, Sm, LnAuAs$_2$ with Ln = Ce – Nd, Sm) were studied for their magnetic behavior. For comparison, the copper samples PrCuAs$_2$ and SmCuAs$_2$, prepared under identical conditions as outlined in the experimental part, were included in this study. Hysteresis measurements at room temperature confirm the paramagnetic nature for most of the compounds as found for the respective LnCuAs$_2$. Most samples develop an antiferromagnetic ordering at low temperature. For each compound, the normalized temperature dependent magnetic moment $m(T)$ in a field of 0.25 T and the normalized field dependent magnetic moment $m(H)$ at 2.5 K were measured. In the figures, $m(T)$ is displayed on the left and $m(H)$ on the right. For all but the Sm compounds, the curves of the inverse susceptibility χ^{-1} is presented as an inset in the $m(T)$ curve. The investigated compounds are presented in detail in the following:

LaAgAs$_2$ (figure 6.6) reveals a paramagnetic behavior down to a temperature of 2 K, seen in both the $m(T)$ and $m(H)$ measurements. The inverse susceptibility χ^{-1} is only straight below 100 K as expected for paramagnetic ordering. A non-linear plot of χ^{-1} vs. T is known from earlier studies for SmCuAs$_2$ [27].

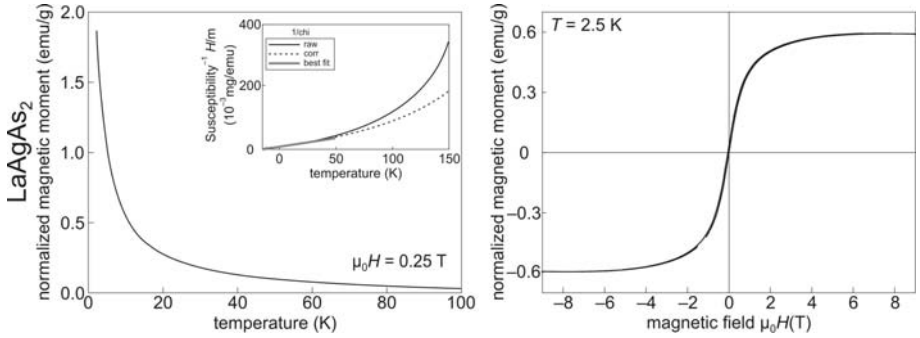

Figure 6.6: Magnetic properties of LaAgAs$_2$. Left: normalized temperature dependent magnetic moment m measured at a fixed field of $\mu_0 H$ = 0.25 T together with the inverse susceptibility $\chi^{-1} = \mu_0 H/m$ as a function of temperature (inset). Right: normalized magnetic moment m as a function of applied field for constant temperature T = 2.5 K.

CeAgAs$_2$ (figure 6.7, top) was already subject of investigation [24, 26] and is included here for comparison reasons, only. It orders antiferromagnetically at $T_N \approx 5$ K, which shows up in the peak of the *m(T)* curve. The irreversible susceptibility (inset) is linear between 25 K and 300 K and intersects the temperature axis at $\theta = -15$ K. A field dependent measurement at 2.5 K (i.e. below T_N), however, reveals a kinked hysteresis at a field of approximately 0.3 T. This metamagnetic transition (a field induced transition into a ferromagnetically ordered state) is known from the previous investigations.

$CeAuAs_2$ (figure 6.7, bottom) reveals a paramagnetic behavior down to a temperature of 2 K, seen in both the $m(T)$ and $m(H)$ measurements. The inverse susceptibility χ^{-1} is not perfectly straight as expected for paramagnetic ordering, therefore antiferromagnetic coupling below 2 K cannot be excluded. The negative extrapolated intersection of χ^{-1} with the temperature axis supports this assumption. The effective magnetic moments ($\mu_{eff,meas}$ = 2.88 μ_B for $CeAgAs_2$ and $\mu_{eff,meas}$ = 1.96 μ_B for $CeAuAs_2$) differ slightly from the magnetic configuration of the isolated Ce^{3+} ions ($\mu_{eff,theor}$ = 2.54 μ_B)

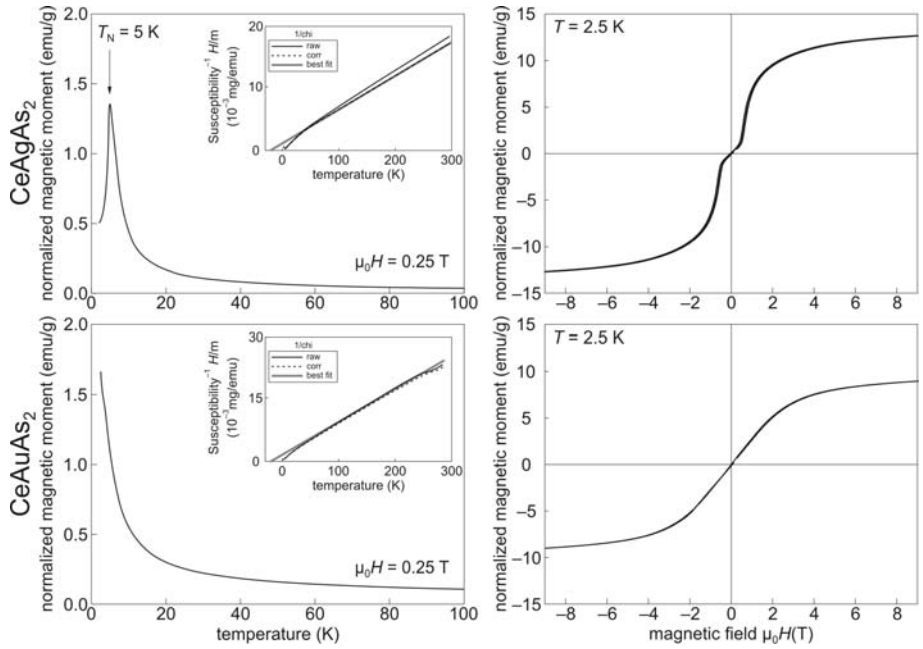

Figure 6.7: Magnetic properties of the CeTAs$_2$ compounds (T = Ag, Au). Left: normalized temperature dependent magnetic moment m measured at a fixed field of $\mu_0 H$ = 0.25 T together with the inverse susceptibility $\chi^{-1} = \mu_0 H/m$ as a function of temperature (inset). Right: normalized magnetic moment m as a function of applied field for constant temperature T = 2.5 K.

For $PrCuAs_2$ (figure 6.8, top), an antiferromagnetic ordering at $T_N \approx 4.5$ K is found in the $m(T)$ curve, which shows up in the peak of the $m(T)$ curve (figure 6.8, top). The inverse susceptibility (inset) is perfectly linear between 10 K and 300 K and intersects the temperature axis at $\theta = -5$ K. A field dependent measurement at 2.5 K (below T_N) reveals a slightly kinked hysteresis, characteristic of a metamagnetic transition at a critical field of about 0.3 T. Such a field induced transition into a ferromagnetically ordered state has already been observed for $CeAgAs_2$, cf. preceding paragraphs and references therein.

$PrAgAs_2$ (figure 6.8, center) shows a ferromagnetic characteristic in the measurement of the normalized temperature dependent magnetic moments at 0.25 T, with an ordering temperature T_{Curie} = 3 – 4 K. Also here, the hysteresis at 2.5 K (below T_C) shows a small kink close to zero that could be taken as an indication for an antiferromagnetic ground state, which

is lifted in a small external field. The inverse susceptibility (inset) is non linear. Therefore no final statement towards a ferromagnetic or antiferromagnetic ground state is possible.

$PrAuAs_2$ (figure 6.8, bottom) is purely paramagnetic down to 2 K, seen in both the $m(T)$ and $m(H)$ measurements. χ^{-1} is again perfectly straight as expected for paramagnetic ordering. Antiferromagnetic coupling below 2 K cannot be excluded, which is supported by the negative extrapolated intersection of χ^{-1} with the temperature axis.

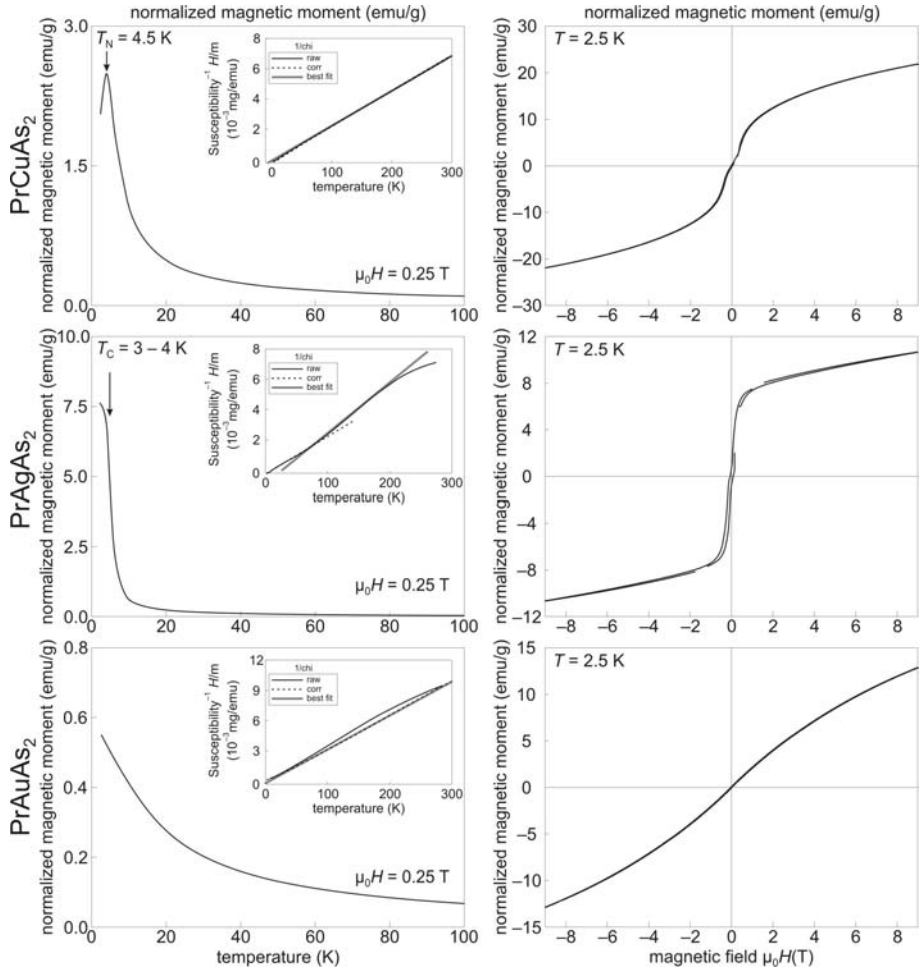

Figure 6.8: Magnetic properties of the PrTAs$_2$ compounds (T = Cu, Ag, Au). Left: normalized temperature dependent magnetic moment m measured at a fixed field of $\mu_0 H = 0.25$ T together with the inverse susceptibility $\chi^{-1} = \mu_0 H/m$ as a function of temperature (inset). Right: normalized magnetic moment m as a function of applied field for constant temperature $T = 2.5$ K.

The experimentally found values of $\mu_{\mathrm{eff,meas}} = 3.42\ \mu_B$ for $PrCuAs_2$ and $\mu_{\mathrm{eff,meas}} = 3.31\ \mu_B$ for $PrAuAs_2$ fit well with the expected value of $\mu_{\mathrm{eff,theor}} = 3.58\ \mu_B$ calculated these compounds. These results confirm that the magnetism in these samples is dominated by the localized moments of the Pr^{3+} ion, which is in consistence with data found in literature [27].

Both $NdAgAs_2$ (figure 6.9, top) and $NdAuAs_2$ (figure 6.9, bottom) reveal antiferromagnetic ordering without metamagnetic transitions and with Neél temperatures of $T_N = 2.7$ K and $T_N = 3.4$ K, respectively. For both compounds, a linear decrease of χ^{-1} with the temperature is observed. Contrary to $PrAuAs_2$, the effective moment of $NdAuAs_2$ in the paramagnetic state differs obviously from the magnetic configuration of the isolated Nd^{3+} ions ($\mu_{eff,meas} = 2.88\ \mu_B$, $\mu_{eff,theor} = 3.62\ \mu_B$).

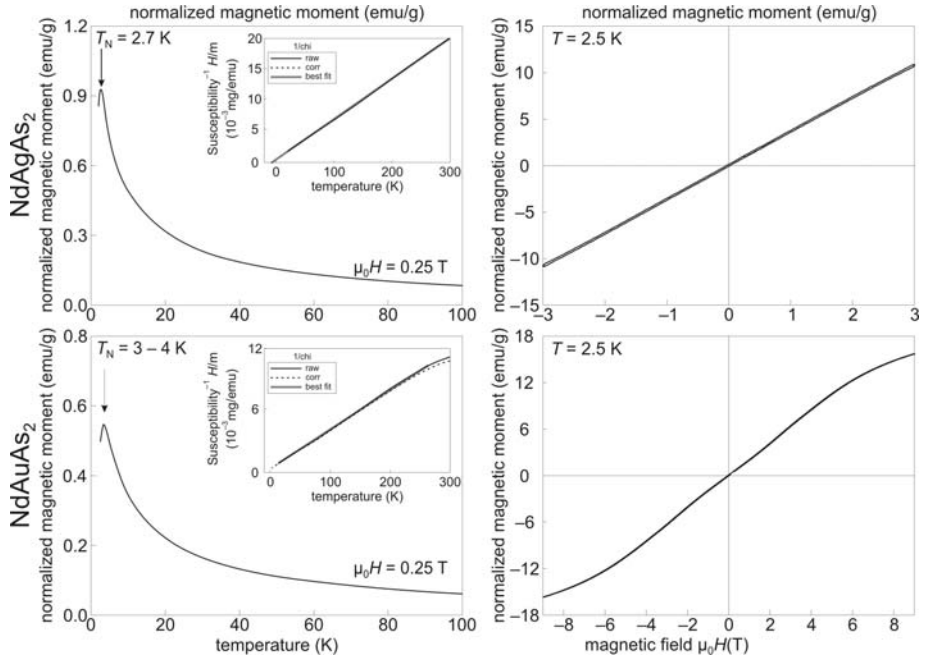

Figure 6.9: Magnetic properties of the $NdTAs_2$ compounds (T = Ag, Au). Left: normalized temperature dependent magnetic moment m measured at a fixed field of $\mu_0 H = 0.25$ T together with the inverse susceptibility $\chi^{-1} = \mu_0 H/m$ as a function of temperature (inset). Right: normalized magnetic moment m as a function of applied field for constant temperature $T = 2.5$ K.

Figure 6.10 displays the temperature dependent, normalized magnetic moments for $SmCuAs_2$ (top in the figure), $SmAgAs_2$ (center) and $SmAuAs_2$ (bottom). Due to the small total angular momentum number $J = 5/2$ and Landé factor $g_L = 2/7$ of the trivalent Sm^{3+}, the normalized moments are considerably smaller compared to the other studied compounds. All three curves show distinct peaks indicating antiferromagnetic ordering at low temperatures. The field dependent hysteresis loops at 2.5 K do not exhibit any sign of a metamagnetic transition. Contrary to the other studied compounds, $SmAuAs_2$ reveals two transitions temperatures, which coincide with the individual ordering temperatures of $SmCuAs_2$ ($T_N = 12.4$ K) and $SmAgAs_2$ ($T_N = 17$ K), respectively. For all three compounds, χ^{-1} (not shown here) was found to be non-linear as observed for $LaAgAs_2$. Contrary to this compound, no straight part was found to determine an ordering at low temperature.

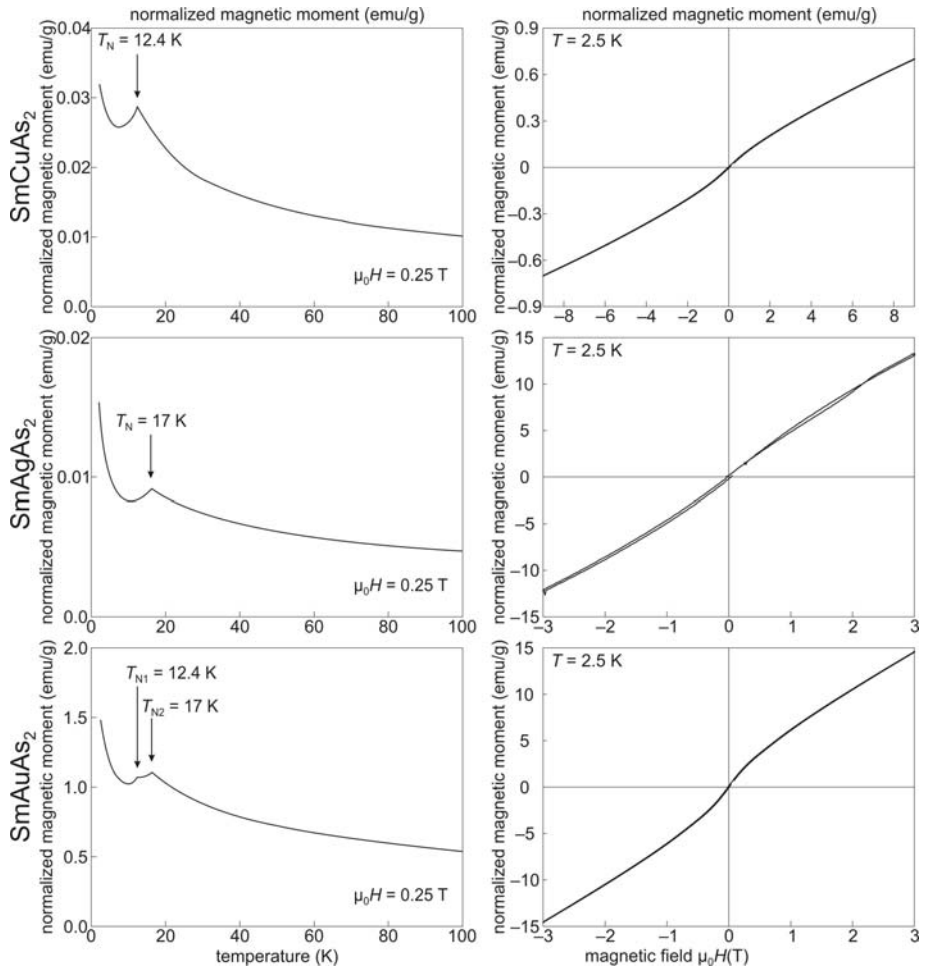

Figure 6.10: Magnetic properties of the SmTAs$_2$ compounds (T = Cu, Ag, Au). Left: normalized temperature dependent magnetic moment m measured at a fixed field of $\mu_0 H = 0.25$ T together with the inverse susceptibility $\chi^{-1} = \mu_0 H/m$ as a function of temperature (inset). Right: normalized magnetic moment m as a function of applied field for constant temperature $T = 2.5$ K.

7 Conclusions and Path Forward

7.1 Conclusions

The crystal structures of the *Ln*$AgAs_2$ and *Ln*$AuAs_2$ compounds were reinvestigated by single-crystal diffraction experiments. Contrary to the respective copper compounds, no stuffed variant of the $HfCuSi_2$ type was found. For $CeAuAs_2$, $GdAuAs_2$ and $TbAuAs_2$, a slight under-occupation of the gold position was determined, the other compounds crystallize in a 1:1:2 ratio. Additionally, $LaCuAs_2$ was synthesized for the first time in a 1:1:2 ratio.

Due to the fact that imaging plate diffraction systems were used instead of four-circle diffractometers, satellite reflections could be observed for most of the *Ln*$CuAs_2$ compounds (*Ln* = Ce, Nd, Sm, Gd, Tb, Ho), $CeAuAs_2$, $GdAuAs_2$ and $TbAuAs_2$. Structure models of $GdCuAs_2$, $CeAuAs_2$, $GdAuAs_2$ and $TbAuAs_2$ were developed, rod and layer groups of the respective structural motives were determined and approximants were presented.

The cell parameters, volumes and the volume per formula unit are summarized in table 7.1. Outlining the devolution of the volume per formula unit with the ionic radii of the respective lanthanide elements, a linear drop of the volumes according to the lanthanide contraction becomes visible (figure 7.1).

Table 7.1: Cell parameters (Å), volumes (Å^3), number of formula units per unit cell and volume per formula unit (Å^3) of the *LnT*As_2 compounds

compound	*a*	*b*	*c*	*V*	*Z*	*V* / *Z*
$LaCuAs_2$	4.013(1)	4.027(1)	20.480(4)	331.0(1)	4	82.75
$GdCuAs_2$	3.904(1)	3.902(1)	9.908(2)	150.9(1)	2	75.46
$LaAgAs_2$	5.801(2)	5.814(2)	21.219(4)	715.5(3)	8	89.44
$CeAgAs_2$	5.771(2)	5.775(2)	21.081(4)	702.6(2)	8	87.82
$PrAgAs_2$	4.017(1)	4.062(1)	21.027(4)	343.1(1)	4	85.85
$NdAgAs_2$	4.032(1)	4.032(1)	20.977(4)	341.0(1)	4	85.26
$SmAgAs_2$	3.995(1)	4.013(1)	20.872(1)	333.1(1)	4	83.64
$GdAgAs_2$	3.973(1)	3.976(1)	20.841(3)	329.3(1)	4	82.32
$TbAgAs_2$	3.956(1)	3.955(1)	20.748(1)	324.6(1)	4	81.15
$CeAuAs_2$	5.804(1)	5.814(1)	10.179(1)	343.5(1)	4	85.87
$PrAuAs_2$	5.766(2)	5.757(2)	20.458(4)	679.1(2)	8	84.88
$NdAuAs_2$	4.058(1)	4.059(1)	20.435(4)	336.6(1)	4	84.15
$SmAuAs_2$	4.019(1)	4.049(1)	20.331(4)	330.9(1)	4	82.72
$GdAuAs_2$	3.597(1)	4.060(2)	10.135(2)	162.8(1)	2	81.41
$TbAuAs_2$	3.993(1)	3.986(1)	10.080(2)	163.4(1)	2	80.21

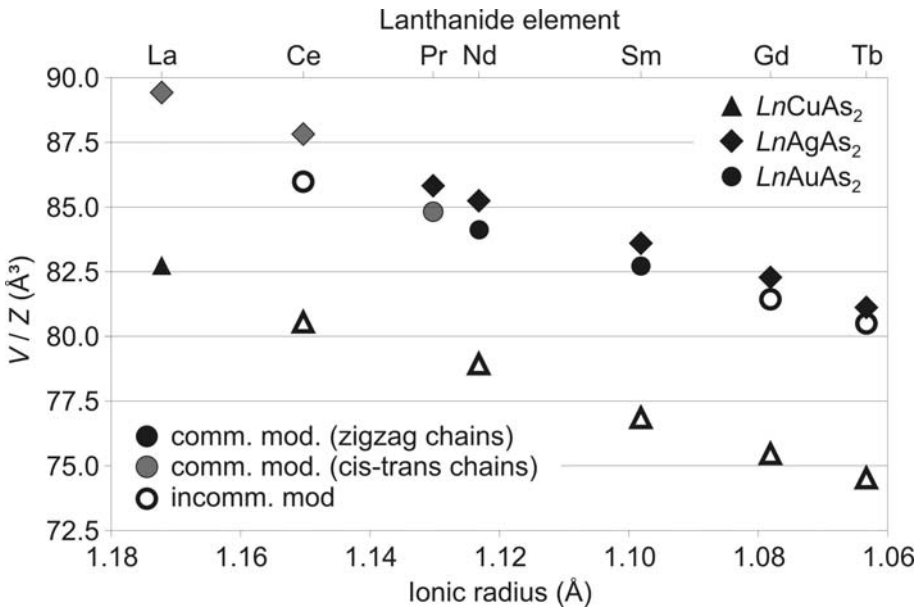

Figure 7.1: Devolution of *V*/*Z* with the ionic radius of the respective lanthanide element. Note: $PrCuAs_2$ was not studied yet, *V*/*Z* of $CeCuAs_2$, $NdCuAs_2$, $SmCuAs_2$ and $TbCuAs_2$ was taken from preliminary results and are included for comparison reasons only.

The assignment of the wrong space groups for numerous $LnAgAs_2$ and $LnAuAs_2$ compounds in literature [8, 29] may be traced back to the fact that all crystals (despite $SmAuAs_2$ in this work) are twinned along [001] due to the pseudo-tetragonal cell. Consequently, the zonal reflection conditions $h0l$: $l = 2n$ for space group *Pmcn* and $h0l$: $l = 2n$, $hk0$: $h = 2n$ for space group *Pmca* [30] are violated and the determination of the correct space group is hampered. The determination of the correct space group is verified in this study by group-subgroup relations following the Bärnighausen formalism for all distortion variants.

The resistivity data reveal a different behavior of compounds crystallizing with cis-trans chains (small-gap semiconductors) and those containing zigzag chains (metals), which is in contradiction to the band structure calculations, whereby both distortion variants should exhibit conducting behavior. One possible explanation for the difference between experimental outcome and calculation might be a segregation of arsenic in the grain boundaries of the pellets during the compression or sintering, which could account for the measured semiconducting behavior of some compounds. Additionally, it should be emphasized that the results of the band structure calculations of $LaAgAs_2$ are compared to the experimental outcome of $CeAgAs_2$, which crystallize in the same structure. Band structure calculations of $CeAgAs_2$ were executed but no convergence was accomplished. Therefore structural related compounds were compared.

The LnTAs$_2$ compounds exhibit different magnetic ordering depending on the lanthanide and coinage-metal species. At room temperature all samples are paramagnetic and all studied compounds despite PrAuAs$_2$ show magnetic ordering between 2 and 20 K. In most cases the effective moment in the paramagnetic state can be explained by the magnetic configuration of the trivalent lanthanide ion.

NdTAs$_2$ (T = Ag, Au) and SmTAs$_2$ (T = Cu, Ag, Au) order antiferromagnetically without a hint for a metamagnetic transition, whereas CeAgAs$_2$ and PrTAs$_2$ (T = Cu, Ag) adopt ferromagnetic ordering above a small critical field. Even for fixed lanthanide species and crystal structure, the ordering temperature depends on the coinage-metal species, suggesting an influence of interatomic distances on the coupling strength of the lanthanide moments. The outcome of the magnetization experiments is summarized in table 7.2.

Table 7.2: Summary of the magnetization experiments (with CeAgAs$_2$ and PrCuAs$_2$ for comparison reasons)

system	mass (mg)	magnetic order	characteristic temperature	$\mu_{eff,theor}$ (μ_B) for RE^{3+}	$\mu_{eff,meas}$ (μ_B f.u.$^{-1}$)	inverse susceptibility
LaAgAs$_2$	7.2	PM	—	—	—	only linear χ^{-1} below 100 K
CeAgAs$_2$	10.2	AF (metamag. trans.)	T_N = 5 K	2.54	2.88	rather linear χ^{-1}
CeAuAs$_2$	31.2	PM, maybe AF below 2 K	Θ = –17 K	2.54	1.96	rather linear χ^{-1}
PrCuAs$_2$	13.8	AF	T_N = 4.5 K	3.58	3.42	kinked χ^{-1}
PrAgAs$_2$	9.1	AF (metamag. trans.) or FM	T_C = 3–4 K	—	—	kinked χ^{-1}
PrAuAs$_2$	13.4	PM, maybe AF below 2 K	Θ = –7 K	3.58	3.31	linear χ^{-1}
NdAuAs$_2$	16.5	AF	T_N = 3.4 K	3.62	2.88	rather linear χ^{-1}
SmAgAs$_2$	7.7	AF	T_N = 17 K	—	—	curved χ^{-1}, too small signal
SmAuAs$_2$	21.7	AF	T_{N1} = 12.4 K; T_{N2} = 17 K	—	—	curved χ^{-1}, too small signal

with C = Curie constant, PM = paramagnetic, AF = antiferromagnetic, FM = ferromagnetiç, Θ = Weiss constant, T_C = Curie temperature, T_N = Neél temperature, χ^{-1} = inverse susceptibility

7.2 Path Forward

In a preliminary study, raw diffraction data revealed satellite reflections for $Ln\mathrm{Cu}_{1+\delta}\mathrm{As}_2$ (Ln = Ce, Nd, Sm, Tb, Ho, $0 \leq \delta \leq 0.11$). Due to the dimensions of their unit cells, structures related to the ones presented in chapter 5.1 may be expected. It is desirable to extend this study and develop structure models and approximants.

In the case of LaCuAs_2 (prepared by the flux method) and $\mathrm{LaCu}_{1.25}\mathrm{As}_2$ (obtained by chemical transport reactions), it is still unclear if the additional Cu position of the latter compound is caused by the different preparation methods. It is also not clear yet if $\mathrm{LaCu}_{1.25}\mathrm{As}_2$ crystallizes in a distorted (e.g. incommensurately modulated) structure.

Due to the fact that LaCuAs_2 in a 1:1:2 ratio is presented in this work, the question arises whether or not the $Ln\mathrm{Cu}_{1+\delta}\mathrm{As}_2$ compounds (Ln = Ce – Nd, Sm) exist in a 1:1:2 ratio as well. All published structures are based on crystals obtained by chemical transport reactions. Therefore a systematic study is highly desirable on the influence of the preparation method on the Cu content of the early $Ln\mathrm{CuAs}_2$ (Ln = La, Ce – Nd, Sm). It is expected, that different volatilities of the two species relevant for the transport, $(\mathrm{CuI})_{3(g)}$ and $Ln\mathrm{I}_{3(g)}$, cause an enrichment of Cu in the deposited crystals at the sink.

According to the reported crystal structures of the respective $Ln T\mathrm{Sb}_2$ (Ln = La, Ce –Nd, Sm, Gd –Tm; T = Cu, Ag, Au) [20], it would be of interest to re-investigate these compounds since the data collection of the only structure based on single-crystal diffraction methods, CeAgSb_2, was performed on a four-circle diffractometer. An under-occupation of the coinage metal in CeAgSb_2 — as found in this work for the incommensurately modulated Au compounds — was reported and the structures of the other compounds were derived by comparison of powder patterns, only. The published structures of the $Ln T\mathrm{Sb}_2$ are related to those, which were the starting point for the $Ln\mathrm{AuAs}_2$ presented in this work. Therefore distorted structures may be taken into account for the $Ln T\mathrm{Sb}_2$ as well.

The inconsistencies between the results of the resistivity measurements and the band structure calculations require additional measurements with differently compacted samples. Ideally, single-crystals of appropriate size may be synthesized. Additional efforts regarding the band structure calculations of CeAgAs_2 are desirable.

8 References

[1] B. Eisenmann, N. May, W. Müller, H. Schäfer, A. Weiss, J. Winter, G. Ziegleder, Z. Naturforsch. 25 (1970) 1350–1352.

[2] B. Eisenmann, N. May, W. Müller, H. Schäfer, Z. Naturforsch. 27b (1972) 1155–1157.

[3] E. Brechtel, G. Cordier, H. Schäfer, Z. Naturforsch. 35b (1979) 1–3.

[4] C. Zheng, R. Hoffmann, J. Am. Chem. Soc. 108 (1986) 3078–3088.

[5] G. Venturini, B. Malaman, B. Roques, J. Solid State Chem. 79 (1989) 126–135.

[6] G. Venturini, B. Malaman, B. Roques, J. Solid State Chem. 79 (1989) 136–145.

[7] S. I. Chykhrij, G. V. Loukasouk, S. V. Oryshchyn, Yu. Kuz'ma, J. Alloys Comp. 248 (1997) 224–232.

[8] M. Wang, B. McDonald, A. Mar, J. Solid State Chem. 147 (1999) 140–145.

[9] Y. Kamihara, H. Hiramatsu, M. Hirano, R. Kawamura, H. Yanagi, T. Kamiya, H. Hosono, J. Am. Chem. Soc. 128 (2006) 10012–10013.

[10] Y. Kamihara, T. Watanabe, M. Hirano, H. Hosono, J. Am. Chem. Soc. 130 (2008) 3296–3297.

[11] F. Hunte, J. Jaroszynski, A. Gurevich, D. C. Larbalestier, R. Jin, A. S. Sefat, M. A. McGuire, B. C. Sales, D. K. Christen, D. Mandrus, D. ArXiv.org, e-Print Archive, Condens. Matter (2008) 0804.0485.

[12] G. F. Chen, Z. Li, D. Wu, G. Li, W. Z. Hu, J. Dong, P. Zheng, J. L. Luo, N. L. Wang, ArXiv.org, e-Print Archive, Condens. Matter (2008) 0803.3790.

[13] Z. A. Ren, W. Lu, J. Yang, W. Yi, X. L. Shen, Z. C. Li, G. C. Che, X. L. Dong, L. L. Sun, F. Zhou, Z. X. Zhao, ArXiv.org, e-Print Archive, Condens. Matter (2008) 0803.2053.

[14] Z. A. Ren, J. Yang, W. Lu, W. Yi, X. L. Shen, Z. C. Li, G. C. Che, X. L. Dong, L. L. Sun, F. Zhou, Z. X. Zhao, ArXiv.org, e-Print Archive, Condens. Matter (2008) 0803.4234.

[15] Z. A. Ren, J. Yang, W. Lu, W. Yi, G. C. Che, X. L. Dong, L. L. Sun, Z. X. Zhao, ArXiv.org, e-Print Archive, Condens. Matter (2008) 0803.4283.

[16] Z. A. Ren, G. C. Che, X. L. Dong, J. Yang, W. Lu, W. Yi, X. L. Shen, Z. C. Li, L. L. Sun, F. Zhou, Z. X. Zhao, ArXiv.org, e-Print Archive, Condens. Matter (2008) 0804.2582.

[17] T. Watanabe, H. Yanagi, T. Kamiya, Y. Kamihara, H. Hiramatsu, M. Hirano, H. Hosono, Inorg. Chem. 46 (2007) 7719–7721.

[18] H. H. Wen, G. Mu, L. Fang, H. Yang, X. Zhu, ArXiv.org, e-Print Archive, Condens. Matter (2008) 0803.3021.

[19] M. Tegel, S. Johansson, V. Weiss, I. Schellenberg, W. Hermes, R. Pöttgen, D. Johrendt, ArXiv.org, e-Print Archive, Condens. Matter (2008) 0810.2120.

[20] O. Sologub, K. Noël, A. Leithe-Jasper, P. Rogl, O. I. Bodak, J. Solid State Chem. 115 (1995) 441–446.

[21] Yu. Mozharivskyj, D. Kaczorowski, H. F. Franzen, J. Solid State Chem. 155 (2000) 259–272.

[22] Yu. Mozharivskyj, D. Kaczorowski, H. F. Franzen, Z. Anorg. Allg. Chem. 627 (2001) 2163–2172.

[23] M. Kolenda, A. Oles, A. Szytula, J. Alloys Comp. 322 (2001) 55–58.

[24] R. Demchyna, J. P. F. Jemetio, Yu. Prots, Th. Doert, L. G. Akselrud, W. Schnelle, Yu. Kuz'ma, Yu. Grin, Z. Anorg. Allg. Chem. 630 (2004) 635–641.

[25] E.V. Sampathkumaran, K. Sengupta, S. Rayaprol, K. K. Iyer, Th. Doert, J. P. F. Jemetio, Phys. Rev. Lett. 91 (2003) 036603.

[26] M. Szlawska, D. Kaczorowski, J. Alloys Comp. 451 (2008) 464–466.

[27] K. Sengupta, S. Rayaprol, E.V. Sampathkumaran, Th. Doert, J.P.F. Jemetio, Physica B: Condensed Matter 348 (2004) 465-474.

[28] M. Abliz, T. Nakano, E. V. Sampathkumaran, J. P. F. Jemetio, Th. Doert, M. Hedo, Y. Uwatoko, J. Phys. Soc. Japan 78 (2005) 508–510.

[29] M. Eschen, W. Jeitschko, Z. Naturforsch. 58b (2003) 399–409.

[30] T. Hahn, A.J.C. Wilson, (Eds.), International Tables for Crystallography, Vol. A, Kluwer Academic Publishers, Dordrecht, 4th ed. 1996.

[31] K. R. Andress, E. Alberti, Zeitschrift für Metallkunde 27 (1935) 126–128.

[32] Z. Bau, M. Sikirica, Acta Crystallogr. 18 (1965) 594–599.

[33] L. S. Andrukhiv, L. A. Lysenko, Ya. P. Yarmolyuk, E. I. Gladyshevskii, Dop. Akad. Nauk Ukr. RSR, Ser. A (1975) 645–648.

[34] H. Onken, K. Vierheilig, H. Hahn, Z. Anorg. Allg. Chem. 333 (1964) 267–279.

[35] F. Jellinek, H. Hahn, Naturwissenschaften 49 (1962) 103.

[36] W. Nieuwenkamp, J. M. Bijvoet, Z. Kristallogr. 81 (1932) 469–474.

[37] G. Cordier, B. Eisenmann, H. Schäfer, Z. Anorg. Allg. Chem. 426 (1976) 205–214.

[38] R. O. Demchyna, H. Borrmann, S. I. Chykhrij, Yu. B. Kuz'ma, Yu. Grin, Z. Kristallogr. NCS 217 (2002) 161–162.

[39] H. Nöel, Z. Zolnierek, D. Kaczorowski, R. Troc, J. Less-Common Metals 132 (1987) 327–332.

[40] S. I. Chykhrij, G. V. Loukashouk, S. V. Oryshchyn, Yu. B. Kuz'ma, J. Alloys Comp. 248 (1997) 224–232.

[41] O. Sologub, K. Hiebl, P. Rogl, H. Noël, O. I. Bodak, J. Alloys. Comp. 210 (1994) 153–157.

[42] M. Brylak, M. H. Möller, W. Jeitschko, J. Solid State Chem. 115 (1995) 305–308.

[43] Yu. Mozharivskyj, V. K. Pecharsky, H. F. Franzen, J. Alloys Comp. 345 (2002) 100–104.

[44] R. O. Demchyna, Yu. B. Kuz'ma, V. S. Babizhetsky, J. Alloys Comp. 315 (2001) 158–163.

[45] J. P. Jemetio, Th. Doert, O. Rademacher, P. Böttcher, J. Alloys Comp. 338 (2002) 93–98.

[46] J. P. Jemetio, Th. Doert, P. Böttcher, Z. Kristallogr. NCS 217 (2002) 455–457.

[47] V. Johnson, W. Jeitschko, J. Solid State Chem. 11 (1974) 161–166.

[48] W. Urland, P. Plambeck-Fischer, M. Grupe, Z. Naturforsch. 44b (1989) 261–264.

[49] E. Brechtel, G. Cordier, H. Schäfer, Z. Naturforsch. 34b (1979) 251–255.

[50] P. G. Cotter, P. A. Kohn, R. A. Potter, J. Am. Cer. Soc. 39 (1956) 11–12.

[51] H. Schachner, H. Nowotny, H. Kudielka, Monatsh. Chem. 85 (1954) 1140–1153.

[52] W. H. Zachariasen, Acta Crystallogr. 16 (1963) 1253–1255.

[53] Q. Johnson, Inorg. Chem. 10 (1971) 2089–2090.

[54] N. L. Eatough, H. T. Hall, Inorg. Chem. 8 (1969) 1439–1445.

[55] O. P. Bodak, E. I. Gladyshevskii, Kristallografiya 14 (1969) 990–994.

[56] G. Sfez, C. Adolphe, Bull. Soc. Fr. Miner. Cristallogr. 95 (1972) 553–557.

[57] R. Ceolin, N. Rodier, P. Khodadad, J. Less-Common Metals 53 (1977) 137–140.

[58] L. H. Strauss, C. M. Delp, J. Alloys Comp. 353 (2003) 143–145.

[59] H. G. von Schnering, W. Wichelhaus, M. Schulze Nahrup, Z. Anorg. Allg. Chem. 412 (1975) 193–201.

[60] K. Deller, B. Eisenmann, Z. Anorg. Allg. Chem. 425 (1976) 104–108.

[61] F. Hulliger, R. Schmelczer, J. Solid State Chem. 26 (1978) 389–396.

[62] R. Schmelczer, D. Schwarzenbach, F. Hulliger, Z. Naturforsch. 36b (1981) 463–469.

[63] E. Dimasi, B. Foran, M. C. Aronson, S. Lee, Phys. Rev. B 54 (1996) 13587–13596.

[64] D. M. Proserpio, G. Chacon, C. Zheng, Chem. Mater. 10 (1998) 1286–1290.

[65] F. Q. Huang, P. Brazis, C. R. Kannewurf, J. A. Ibers, Inorg. Chem. 39 (2000) 3176–3180.

[66] Yu. Mozharivskyj, A. O. Pecharsky, S. Bud'ko, H. F. Franzen, Z. Anorg. Allg. Chem. 628 (2002) 1619–1630.

[67] Y. C. Wang, K. M. Poduska, R. Hoffmann, F. J. Disalvo, J. Alloys Comp. 314 (2001) 132–139.

[68] F. Hulliger, Nature 219 (1968) 373–374.

[69] F. Hulliger, R. Schmelczer, D. Schwarzenbach, J. Solid State Chem. 21 (1977) 371–374.

[70] A. Simon, H. Borrmann, H. Craubner, Phosphorus and Sulfur and the Related Elements 30 (1987) 507–510.

[71] A. F. Wells, Structural Inoganic Chemistry, Clarendon Press, Oxford, 5th ed., 1984.

[72] E. V. Sampathkumaran, T. Ekino, R. A. Ribeiro, K. Sengupta, T. Nakano, M. Hedo, N. Fujiwara, M. Abliz, Y. Uwatoko, S. Rayaprol, Th. Doert, J. P. F. Jemetio, Physica B (2005) 108–110.

[73] WinXPow, Program for the Collection and the Evaluation of X-ray Powder Data, Stoe & Cie. GmbH, Darmstadt, 1999.

[74] XRed32, Data Reduction Program, Stoe & Cie. GmbH, Darmstadt, 2001.

[75] XShape, Crystal Optimisation for Numerical Absorption Correction Program, Stoe & Cie. GmbH, Darmstadt, 1999.

[76] SHELX97, Program for Crystal Structure Determination, G. M. Sheldrick, University of Göttingen, 1997.

[77] JANA2000, Crystallographic Computing System for Standard and Modulated Structures, V. Petříček, N. Dušek, L. Palatinus, Prague, 2000.

[78] H. Bärnighausen, Match 9 (1980) 139–175.

[79] H. Wondratschek, U. Müller (Eds.), International Tables for Crystallography Vol. A1, Kluwer Academic Publishers, Dordrecht, 1st ed., 2006.

[80] T. Janssen, A. Janner, A. Looijenga-Vos, P. M. de Wolff, E. Prince, International Tables for Crystallography, Vol. C, 1st online ed., 2006.

[81] K. Koepernik, H. Eschrig, Phys. Rev. B59 (1999) 1743–1757.

[82] I. Ophale, K. Koepernik, H. Eschrig, Phys. Rev. B60 (1999) 14035–14041.

[83] J. P. Perdew, Y. Wang, Phys. Rev. B45 (1992) 13244–13249.

[84] M. T. Czyzyk, G. A. Sawatzky, Phys. Rev. B49 (1994) 14211–14228.

[85] H. Eschrig, K. Koepernik, I. Chaplygin, J. Solid State Chem. 176 (2003) 482–495.

[86] V. I. Anisimov, J. Zaanen, O. K. Andersen, Phys. Rev. B44 (1991) 943–954.

[87] A. I. Liechtenstein, V. I. Anisimov, J. Zaanen, Phys. Rev. 52 (1995) R5467–R5470.

[88] P. M. de Wolff, T. Janssen, A. Janner, Acta Cryst. A37 (1981), 625–636.

[89] S. van Smaalen, Crystallogr. Rev. 4 (1995), 79–202.

[90] S. van Smaalen, Incommensurate Crystallography, Oxford University Press, Oxford, 2007.

[91] X-Area, IPDS 2 Software Package, Stoe & Cie. GmbH, Darmstadt, 2006

[92] M. J. Ferguson, R. W. Hushagen, A. Mar, Inorg. Chem. 35 (1996) 4505–4512.

[93] Kopsky, V., Litvin, D. B. International Tables for Crystallography Vol. E, 1st online ed., 2006

[94] P. Becker, P. Coppens, Acta Cryst. A30 (1974) 129–147.

9 Appendix

9.1 Crystallographic Data

$LaCuAs_2$

Table 9.1: Crystallographic and refinement data of $LaCuAs_2$

chemical formula	$LaCuAs_2$
formula weight (g mole^{-1})	352.29
space group	*Pnma*
a (Å)	4.013(1)
b (Å)	4.027(1)
c (Å)	20.480(4)
V (Å^3)	331.0(1)
Z	4
ρ_x (g cm^{-3})	7.070
crystal size (mm^3)	0.143 × 0.120 × 0.004
radiation, λ	Mo $K\alpha$, 0.71073 Å
diffractometer	IPDS I
T_{min}, T_{max}	0.156, 0.870
θ range (°)	$1.99 \leq \theta \leq 25.77$
range of h; k; l	$-4 \leq h \leq 4$, $-4 \leq k \leq 4$, $-24 \leq l \leq 25$
number of measured reflections	3362
number of independent reflections	390
number of observed reflections	349
number of parameters	27
refinement	SHELXL97, full matrix least squares, against F^2
R_{int}	0.0566
R_1	0.0262
wR_2 ($I > 3\sigma$)	0.0602
S (all I)	1.096
$\Delta\rho_{max}$, $\Delta\rho_{min}$ (e$^-$ Å^{-3})	1.07, –1.59
twin fractions	0.26, 0.74

Table 9.2: Wyckoff sites, atomic coordinates and coefficients U_{ij}* of the tensors of the anisotropic displacement parameter (Å^2) for $LaCuAs_2$

atom	site	x	y	z	U_{11}	U_{22}	U_{33}	U_{23}
La	4*c*	¼	0.7253(2)	0.12149(3)	0.0062(5)	0.0043(4)	0.0041(3)	0.0001(2)
Cu	4*c*	¼	0.2246(3)	0.2500(1)	0.0116(9)	0.0105(8)	0.0066(7)	0.0005(6)
As1	4*c*	¼	0.7246(3)	0.32330(4)	0.0059(7)	0.0044(7)	0.0064(5)	0.0002(4)
As2	4*c*	¼	0.2029(3)	0.00152(8)	0.0120(7)	0.0089(6)	0.0039(6)	0.0000(5)

* $U_{12} = U_{23} = 0$

Table 9.3: Selected interatomic distances (Å) of $LaCuAs_2$

La1–As1 $^{i, ii}$	3.057(1)	La1–Cu1 ^{viii}	3.315(2)
La1–As1 $^{iii, iv}$	3.061(1)	Cu1–As1 $^{i, ii}$	2.506(2)
La1–As2 ^{v}	3.120(2)	Cu1–As1 ^{v}	2.512(2)
La1–As2 $^{vi, vii}$	3.234(1)	Cu1–As1	2.512(2)
La1–As2	3.234(2)	Cu1–Cu1 $^{i, ii, iii, iv}$	2.842(1)
La1–Cu1 $^{iii, iv}$	3.310(2)	As2–As2 $^{ix, x}$	2.589(1)
La1–Cu1	3.312(2)		

symmetry codes: (i) = $-x+1$, $y+1/2$, $-z+1/2$; (ii) = $-x$, $y+1/2$, $-z+1/2$; (iii) = $-x$, $y-1/2$, $-z+1/2$; (iv) = $-x+1$, $y-1/2$, $-z+1/2$; (v) = x, $y+1$, z; (vi) = $-x$, $-y-1$, $-z$; (vii) = $-x+1$, $-y-1$, $-z$; (viii) = x, $y-1$, z; (ix) = $-x$, $-y-2$, $-z$; (x) = $-x+1$, $-y-2$, $-z$;

$LaAgAs_2$

Table 9.4: Crystallographic and refinement data of $LaAgAs_2$

chemical formula	$LaAgAs_2$
formula weight (g mole^{-1})	396.62
space group	*Pmca*
a (Å)	5.801(2)
b (Å)	5.814(2)
c (Å)	21.219(4)
V (Å^3)	715.5(3)
Z	8
ρ_x (g cm^{-3})	7.36
crystal size (mm^3)	0.130 × 0.108 × 0.005
radiation, λ	Mo *K*α, 0.71073 Å
diffractometer	IPDS I
T_{min}, T_{max}	0.148, 0.875
θ range (°)	$1.92 \le \theta \le 25.80$
range of *h*; *k*; *l*	$-7 \le h \le 7, -7 \le k \le 7, -25 \le l \le 25$
number of measured reflections	7552
number of independent reflections	832
number of observed reflections	538
number of parameters	46
refinement	SHELXL97, full matrix least squares, against F^2
R_{int}	0.084
R_1	0.032
wR_2 ($I > 3\sigma$)	0.056
S (all *I*)	0.99
$\Delta\rho_{max}$, $\Delta\rho_{min}$ (e$^-$ Å^{-3})	1.57, –1.49
twin fractions	0.83, 0.17

Table 9.5: Wyckoff sites and atomic coordinates for $LaAgAs_2$

atom	Wyckoff site	*x*	*y*	*z*
La1	4*d*	¼	0.5150(2)	0.6142(1)
La2	4*d*	¼	0.0161(2)	0.8806(1)
Ag1	4*c*	½	0.2351(2)	¼
Ag2	4*c*	½	0.7317(2)	¼
As1	4*d*	¼	0.5169(4)	0.8369(1)
As2	4*d*	¼	0.0156(4)	0.6642(1)
As3	8*e*	0.5323(2)	0.2170(2)	0.0016(2)

Table 9.6: Coefficients U_{ij} of the tensors of the anisotropic displacement parameter (Å^2) for $LaAgAs_2$

atom	U_{11}	U_{22}	U_{33}	U_{12}	U_{13}	U_{23}
La1	0.0039(7)	0.0031(5)	0.0047(5)	0	0	0.0014(5)
La2	0.0036(7)	0.0037(5)	0.0052(5)	0	0	0.0004(5)
Ag1	0.010(2)	0.006(1)	0.009(1)	0	0.0006(7)	0
Ag2	0.006(2)	0.0083(9)	0.010(1)	0	0.0001(7)	0
As1	0.005(1)	0.0035(8)	0.0066(9)	0	0	0.0003(9)
As2	0.005(1)	0.0033(8)	0.0078(9)	0	0	0.0013(9)
As3	0.0061(5)	0.0070(4)	0.0062(5)	0.0001(4)	–0.0006(7)	0.0009(7)

Table 9.7: Selected interatomic distances (Å) of $LaAgAs_2$

La1–As1 $^{i, ii}$	3.081(1)
La1–As2	3.091(3)
La1–As2 ^{iii}	3.098(3)
La1–As3 $^{iv, v}$	3.260(2)
La1–As3 $^{vi, vii}$	3.288(2)
La1–Ag2 $^{viii, ix}$	3.531(1)
La1–Ag1 $^{viii, ix}$	3.539(1)
La2–As1 ^{x}	3.047(3)
La2–As2 $^{i, ii}$	3.052(1)
La2–As1	3.056(3)
La2–As3 $^{xi, xii}$	3.110(2)
La2–As3 $^{xiii, xiv}$	3.261(2)
La2–Ag1 $^{xi, xii}$	3.452(1)
La2–Ag2 $^{viii, ix}$	3.455(1)
Ag1–As2 $^{xi, xv}$	2.746(2)
Ag1–As1 $^{viii, xvi}$	2.753(2)
Ag1–Ag2	2.887(2)
Ag1–Ag1 $^{xvii, xviii}$	2.900(1)
Ag1–Ag2 ^{x}	2.926(2)
Ag2–As2 $^{viii, xvi}$	2.752(2)
Ag2–As1 $^{viii, xvi}$	2.755(2)
Ag2–Ag2 $^{xvii, xviii}$	2.900(1)
Ag2–Ag1 ^{iii}	2.926(2)
As3–As3 ^{xvii}	2.526(2)
As3–As3 ^{xix}	2.552(2)

symmetry codes: (i) = x+1/2, y, $-z$+3/2; (ii) = x–1/2, y, $-z$+3/2; (iii) = x, y+1, z; (iv) = x–1/2, y, $-z$+1/2; (v) = $-x$+1, y, $-z$+1/2; (vi) = $-x$+1/2, $-y$+1, z+1/2; (vii) = x, $-y$+1, z+1/2; (viii) = $-x$+1, $-y$+1, $-z$+1; (ix) = x–1/2, $-y$+1, $-z$+1; (x) = x, y–1, z; (xi) = $-x$+1, $-y$, $-z$+1; (xii) = x–1/2, $-y$, $-z$+1; (xiii) = x, y, z+1; (xiv) = $-x$+1/2, y, z+1; (xv) = $-x$+1/2, $-y$, z–1/2; (xvi) = $-x$+1/2, $-y$+1, z–1/2; (xvii) = $-x$+3/2, y, z; (xviii) = $-x$+1/2, y, z; (xix) = $-x$+1, $-y$, $-z$

$CeAgAs_2$

Table 9.8: Crystallographic and refinement data of $CeAgAs_2$

chemical formula	$CeAgAs_2$
formula weight (g mole^{-1})	397.83
space group	*Pmca*
a (Å)	5.771(2)
b (Å)	5.775(2)
c (Å)	21.081(4)
V (Å^3)	702.6(2)
Z	8
ρ_x (g cm^{-3})	7.55
crystal size (mm^3)	0.083 × 0.046 × 0.028
radiation, λ	Mo *K*α, 0.71073 Å
diffractometer	IPDS I
T_{min}, T_{max}	0.226, 0.346
θ range (°)	$3.53 \le \theta \le 25.85$
range of *h*; *k*; *l*	$-7 \le h \le 7, -7 \le k \le 7, -24 \le l \le 24$
number of measured reflections	7336
number of independent reflections	762
number of observed reflections	552
number of parameters	46
refinement	SHELXL97, full matrix least squares, against F^2
R_{int}	0.105
R_1	0.033
wR_2 ($I > 3\sigma$)	0.066
S (all *I*)	1.09
$\Delta\rho_{max}$, $\Delta\rho_{min}$ (e$^-$ Å^{-3})	1.59, –1.80
twin fractions	0.61, 0.39

Table 9.9: Wyckoff sites and atomic coordinates for $CeAgAs_2$

atom	Wyckoff site	*x*	*y*	*z*
Ce1	4*d*	¼	0.5130(2)	0.6135(1)
Ce2	4d	¼	0.0141(2)	0.8821(1)
Ag1	4*c*	½	0.2372(2)	¼
Ag2	4*c*	½	0.7341(2)	¼
As1	4*d*	¼	0.5136(3)	0.8386(1)
As2	4*d*	¼	0.0142(3)	0.6623(1)
As3	8*e*	0.5283(2)	0.2216(2)	0.0009(2)

Table 9.10: Coefficients U_{ij} of the tensors of the anisotropic displacement parameter (Å^2) for $CeAgAs_2$

atom	U_{11}	U_{22}	U_{33}	U_{12}	U_{13}	U_{23}
Ce1	0.0049(7)	0.0042(6)	0.0097(8)	0	0	–0.0007(4)
Ce2	0.0047(7)	0.0037(7)	0.0088(8)	0	0	–0.0007(4)
Ag1	0.009(2)	0.008(1)	0.012(2)	0	0.0011(7)	0
Ag2	0.008(2)	0.010(1)	0.011(1)	0	0.0012(7)	0
As1	0.004(1)	0.005(1)	0.012(1)	0	0	–0.0004(8)
As2	0.007(1)	0.004(1)	0.009(1)	0	0	–0.0007(8)
As3	0.0083(5)	0.0089(5)	0.0095(7)	0.0003(4)	–0.0006(8)	–0.0007(8)

Table 9.11: Selected interatomic distances (Å) of $CeAgAs_2$

Ce1–As1 [i, ii]	3.057(1)
Ce1–As2	3.059(2)
Ce1–As2 [iii]	3.072(2)
Ce1–As3 [iv, v]	3.207(3)
Ce1–As3 [vi, vii]	3.250(3)
Ce1–Ag2 [viii, ix]	3.521(1)
Ce1–Ag1 [viii, ix]	3.528(1)
Ce2–As1 [x]	3.032(2)
Ce2–As1	3.027(2)
Ce2–As2 [i, ii]	3.033(1)
Ce2–As3 [xi, xii]	3.094(3)
Ce2–As3 [xiii, xiv]	3.208(3)
Ce2–Ag1 [xi, xii]	3.455(1)
Ce2–Ag2 [viii, ix]	3.457(1)
Ag1–As2 [xi, xv]	2.758(2)
Ag1–As1 [viii, xvi]	2.764(2)
Ag1–Ag2	2.869(2)
Ag1–Ag1 [xvii, xviii]	2.885(1)
Ag1–Ag2 [x]	2.905(2)
Ag2–As2 [viii, xvi]	2.759(2)
Ag2–As1 [viii, xvi]	2.759(2)
Ag2–Ag2 [xvii, xviii]	2.885(1)
Ag2–Ag1 [iii]	2.905(2)
As3–As3 [xvii]	2.559(2)
As3–As3 [xix]	2.581(2)

symmetry codes: (i) = x+1/2, y, $-z$+3/2; (ii) = x–1/2, y, $-z$+3/2; (iii) = x, y+1, z; (iv) = x–1/2, y, $-z$+1/2; (v) = $-x$+1, y, $-z$+1/2; (vi) = $-x$+1/2, $-y$+1, z+1/2; (vii) = x, $-y$+1, z+1/2; (viii) = $-x$+1, $-y$+1, $-z$+1; (ix) = x–1/2, $-y$+1, $-z$+1; (x) = x, y–1, z; (xi) = $-x$+1, $-y$, $-z$+1; (xii) = x–1/2, $-y$, $-z$+1; (xiii) = x, y, z+1; (xiv) = $-x$+1/2, y, z+1; (xv) = $-x$+1/2, $-y$, z–1/2; (xvi) = $-x$+1/2, $-y$+1, z–1/2; (xvii) = $-x$+3/2, y, z; (xviii) = $-x$+1/2, y, z; (xix) = $-x$+1, $-y$, $-z$

$PrAgAs_2$

Table 9.12: Crystallographic and refinement data of $PrAgAs_2$

chemical formula	$PrAgAs_2$
formula weight (g mole^{-1})	398.62
space group	*Pnma*
a (Å)	4.017(1)
b (Å)	4.062(1)
c (Å)	21.027(4)
V (Å^3)	343.1(2)
Z	4
ρ_x (g cm^{-3})	7.72
crystal size (mm^3)	0.049 × 0.041 × 0.006
radiation, λ	Mo $K\alpha$, 0.71073 Å
diffractometer	IPDS I
T_{min}, T_{max}	0.245, 0.790
θ range (°)	$2.91 \le \theta \le 25.72$
range of h; k; l	$-4 \le h \le 4$, $-4 \le k \le 4$, $-25 \le l \le 25$
number of measured reflections	3568
number of independent reflections	398
number of observed reflections	300
number of parameters	27
refinement	SHELXL97, full matrix least squares, against F^2
R_{int}	0.087
R_1	0.033
wR_2 ($I > 3\sigma$)	0.075
S (all I)	1.04
$\Delta\rho_{max}$, $\Delta\rho_{min}$ (e$^-$ Å^{-3})	2.26, –2.06
twin fractions	0.95, 0.05

Table 9.13: Wyckoff sites, atomic coordinates and coefficients U_{ij}* of the tensors of the anisotropic displacement parameter (Å^2) for $PrAgAs_2$

atom	site	x	y	z	U_{11}	U_{22}	U_{33}	U_{23}
Pr	4*c*	¼	0.2257(2)	0.1157(1)	0.0080(6)	0.0041(5)	0.0054(4)	0.0001(3)
Ag	4*c*	¼	0.7241(3)	0.2502(1)	0.0126(8)	0.0069(6)	0.0097(6)	–0.0011(4)
As1	4*c*	¼	0.2244(3)	0.3388(1)	0.009(1)	0.0028(7)	0.0068(8)	–0.0001(5)
As2	4*c*	¼	0.7018(4)	0.0015(8)	0.011(1)	0.0078(7)	0.0060(8)	0.0002(6)

* $U_{12} = U_{23} = 0$

Table 9.14: Selected interatomic distances (Å) of $PrAgAs_2$

Pr–As1 $^{i, ii}$	3.008(1)	Pr–Ag ^{vii}	3.485(2)
Pr–As1 $^{iii, iv}$	3.016(2)	Ag–As1 $^{i, ii}$	2.745(1)
Pr–As2	3.083(2)	Ag–As1	2.755(2)
Pr–As2 $^{v, vi}$	3.194(2)	Ag–As1 ^{viii}	2.757(2)
Pr–As2 ^{vii}	3.209(2)	Ag–Ag1 $^{i, ii, iii, iv}$	2.856(0)
Pr–Ag $^{iii, iv}$	3.461(1)	As2–As2 $^{v, vi}$	2.593(2)
Pr–Ag	3.477(2)		

symmetry codes: (i) = $-x$, $y-1/2$, $-z+1/2$, (ii) = $-x+1$, $y-1/2$, $-z+1/2$, (iii) = $-x+1$, $y+1/2$, $-z+1/2$, (iv) = $-x$, $y+1/2$, $-z+1/2$, (v) = $-x$, $-y+1$, $-z$, (vi) = $-x+1$, $-y+1$, $-z$, (vii) = x, $y-1$, z, (viii) = x, $y+1$, y

$NdAgAs_2$

Table 9.15: Crystallographic and refinement data of $NdAgAs_2$

chemical formula	$NdAgAs_2$
formula weight (g mole^{-1})	401.95
space group	*Pnma*
a (Å)	4.032(1)
b (Å)	4.032(1)
c (Å)	20.977(4)
V (Å^3)	341.0(2)
Z	4
ρ_x (g cm^{-3})	7.83
crystal size (mm^3)	0.045 × 0.028 × 0.027
radiation, λ	Mo $K\alpha$, 0.71073 Å
diffractometer	IPDS I
T_{min}, T_{max}	0.343, 0.446
θ range (°)	$2.90 \le \theta \le 25.75$
range of h; k; l	$-4 \le h \le 4$, $-4 \le k \le 4$, $-23 \le l \le 24$
number of measured reflections	3491
number of independent reflections	387
number of observed reflections	321
number of parameters	27
refinement	SHELXL97, full matrix least squares, against F^2
R_{int}	0.060
R_1	0.022
wR_2 ($I > 3\sigma$)	0.052
S (all I)	1.11
$\Delta\rho_{max}$, $\Delta\rho_{min}$ (e$^-$ Å^{-3})	2.00, –1.48
twin fractions	0.54, 0.46

Table 9.16: Wyckoff sites, atomic coordinates and coefficients U_{ij}* of the tensors of the anisotropic displacement parameter (Å^2) for $NdAgAs_2$

Atom	site	x	y	z	U_{11}	U_{22}	U_{33}	U_{23}
Nd	4*c*	¼	0.2278(3)	0.1154(1)	0.0120(9)	0.0047(7)	0.0045(4)	0.0002(3)
Ag	4*c*	¼	0.7263(3)	0.2499(4)	0.014(1)	0.011(1)	0.0078(5)	–0.0001(9)
As1	4*c*	¼	0.2274(4)	0.3396(1)	0.012(2)	0.005(2)	0.0071(7)	–0.0001(5)
As2	4*c*	¼	0.7045(4)	0.0010(3)	0.012(1)	0.0115(9)	0.0052(8)	–0.004(1)

* $U_{12} = U_{23} = 0$

Table 9.17: Selected interatomic distances (Å) of $NdAgAs_2$

Nd–As1 [i, ii]	3.004(2)	Nd–Ag [vii]	3.471(7)
Nd–As2	3.075(6)	Ag–As1	2.754(6)
Nd–As1 [iii, iv]	3.002(2)	Ag–As1 [iii, vi]	2.754(6)
Nd–As2 [v, vi]	3.179(6)	Ag–Ag [i, ii, iii, iv]	2.851(0)
Nd–As2 [vii]	3.196(6)	Ag–As1 [viii]	2.761(6)
Nd–Ag	3.464(7)	As2–As2 [v, vi]	2.605(2)
Nd–Ag [i, ii]	3.470(7)		

symmetry codes: (i) = $-x$, $y-1/2$, $-z+1/2$, (ii) = $-x+1$, $y-1/2$, $-z+1/2$, (iii) = $-x+1$, $y+1/2$, $-z+1/2$, (iv) = $-x$, $y+1/2$, $-z+1/2$, (v) = $-x$, $-y+1$, $-z$, (vi) = $-x+1$, $-y+1$, $-z$, (vii) = x, $y-1$, z, (viii) = x, $y+1$, y

$SmAgAs_2$

Table 9.18: Crystallographic and refinement data of $SmAgAs_2$

chemical formula	$SmAgAs_2$
formula weight (g mole^{-1})	408.06
space group	*Pnma*
a (Å)	3.995(1)
b (Å)	4.013(1)
c (Å)	20.872(1)
V (Å^3)	333.1(2)
Z	4
ρ_x (g cm^{-3})	8.14
crystal size (mm^3)	0.108 × 0.095 × 0.004
radiation, λ	Mo $K\alpha$, 0.71073 Å
diffractometer	IPDS I
T_{min}, T_{max}	0.188, 0.932
θ range (°)	$2.94 \le \theta \le 25.71$
range of h; k; l	$-4 \le h \le 4$, $-4 \le k \le 4$, $-25 \le l \le 25$
number of measured reflections	3477
number of independent reflections	392
number of observed reflections	302
number of parameters	27
refinement	SHELXL97, full matrix least squares, against F^2
R_{int}	0.053
R_1	0.023
wR_2 ($I > 3\sigma$)	0.045
S (all I)	1.10
$\Delta\rho_{max}$, $\Delta\rho_{min}$ (e$^-$ Å^{-3})	1.91, –1.41
twin fractions	0.53, 0.47

Table 9.19: Wyckoff sites, atomic coordinates and coefficients U_{ij}* of the tensors of the anisotropic displacement parameter (Å^2) for $SmAgAs_2$

atom	site	x	y	z	U_{11}	U_{22}	U_{33}	U_{23}
Sm	4*c*	¼	0.2377(3)	0.1149(1)	0.004(1)	0.010(1)	0.0071(3)	–0.0004
Ag	4*c*	¼	0.7388(4)	0.2500(3)	0.013(2)	0.009(2)	0.0108(4)	–0.0003(7)
As1	4*c*	¼	0.2383(5)	0.3411(1)	0.006(3)	0.007(3)	0.0086(6)	–0.0009(7)
As2	4*c*	¼	0.7255(6)	0.0017(4)	0.019(2)	0.019(2)	0.0057(8)	0.000(1)

* $U_{12} = U_{23} = 0$

Table 9.20: Selected interatomic distances (Å) of $SmAgAs_2$

Sm–As1 [i, ii]	2.974(2)	Sm–Ag	3.453(5)
Sm–As1 [iii, iv]	2.977(2)	Ag–As1 [iii, iv]	2.750(4)
Sm–As2	3.059(7)	Ag–As1 [viii]	2.757(5)
Sm–As2 [v]	3.122(7)	Ag–As1	2.760(5)
Sm–As2 [vi, vii]	3.143(6)	Ag–Ag [i, ii, iii, iv]	2.831(1)
Sm–Ag [i, ii]	3.446(5)	As2–As2 [vi, vii]	2.696(3)
Sm–Ag [v]	3.448(5)		

symmetry codes: (i) = –*x*+1, *y*+1/2, –*z*+1/2, (ii) = –*x*, *y*+1/2, –*z*+1/2, (iii) = –*x*, *y*–1/2, –*z*+1/2, (iv) = –y+1, *y*–1/2, –*z*+1/2, (v) = *x*, *y*–1, *z*, (vi) = –*x*, –*y*+1, –*z*, (vii) = –*x*+1, –*y*+1, –*z*, (viii) = *x*, *y*+1, *z*

$GdAgAs_2$

Table 9.21: Crystallographic and refinement data of $GdAgAs_2$

chemical formula	$GdAgAs_2$
formula weight (g mole^{-1})	414.96
space group	*Pnma*
a (Å)	3.973(1)
b (Å)	3.976(1)
c (Å)	20.84(1)
V (Å^3)	329.28(7)
Z	4
ρ_x (g cm^{-3})	8.37
crystal size (mm^3)	0.180 × 0.160 × 0.017
radiation, λ	Mo $K\alpha$, 0.71073 Å
diffractometer	IPDS II
T_{min}, T_{max}	0.030, 0.458
θ range (°)	$2.93 \le \theta \le 33.35$
range of h; k; l	$-6 \le h \le 6$, $-6 \le k \le 6$, $-32 \le l \le 28$
number of measured reflections	6539
number of independent reflections	769
number of observed reflections	678
number of parameters	27
refinement	SHELXL97, full matrix least squares, against F^2
R_{int}	0.050
R_1	0.030
wR_2 ($I > 3\sigma$)	0.074
S (all I)	1.07
$\Delta\rho_{max}$, $\Delta\rho_{min}$ (e$^-$ Å^{-3})	1.95, –2.31
twin fractions	0.44, 0.56

Table 9.22: Wyckoff sites, atomic coordinates and coefficients U_{ij}* of the tensors of the anisotropic displacement parameter (Å^2) for $GdAgAs_2$

atom	site	x	y	z	U_{11}	U_{22}	U_{33}	U_{23}
Gd	4*c*	¼	0.2297(2)	0.1144(1)	0.0112(4)	0.0088(3)	0.0122(2)	0.0000(2)
Ag	4*c*	¼	0.7295(2)	0.2498(2)	0.0153(5)	0.0128(4)	0.0168(3)	–0.0003(3)
As1	4*c*	¼	0.2299(2)	0.3420(1)	0.0133(7)	0.0080(5)	0.0137(4)	0.0004(2)
As2	4*c*	¼	0.7087(2)	0.0016(2)	0.0128(5)	0.0117(3)	0.0117(4)	–0.0003(6)

* $U_{12} = U_{23} = 0$

Table 9.23: Selected interatomic distances (Å) of $GdAgAs_2$

Gd–As1 $^{i, ii}$	2.953(1)	Gd–Ag1 $^{i, ii}$	3.458(3)
Gd–As1 $^{iii, iv}$	2.954(1)	Ag–As1 $^{iii, iv}$	2.759(2)
Gd–As2	3.026(2)	Ag–As1	2.765(3)
Gd–As2 ^{v}	3.134(3)	Ag–As1 ^{viii}	2.767(2)
Gd–As2 $^{vi, vii}$	3.138(2)	Ag–Ag $^{i, ii, iii, iv}$	2.811(0)
Gd–Ag	3.451(3)	As2–As2 $^{vi, vii}$	2.589(1)
Gd–Ag ^{v}	3.452(3)		

symmetry codes: (i) = $-x+1$, $y+1/2$, $-z+1/2$, (ii) = $-x$, $y+1/2$, $-z+1/2$, (iii) = $-x$, $y-1/2$, $-z+1/2$, (iv) = $-y+1$, $y-1/2$, $-z+1/2$, (v) = x, $y-1$, z, (vi) = $-x$, $-y+1$, $-z$, (vii) = $-x+1$, $-y+1$, $-z$, (viii) = x, $y+1$, z

$TbAgAs_2$

Table 9.24: Crystallographic and refinement data of $TbAgAs_2$

chemical formula	$TbAgAs_2$
formula weight (g mole^{-1})	416,63
space group	*Pnma*
a (Å)	3.956(1)
b (Å)	3.955(1)
c (Å)	20.841(3)
V (Å^3)	324.6(1)
Z	4
ρ_x (g cm^{-3})	8.52
crystal size (mm^3)	0.085 × 0.060 × 0.003
radiation, λ	Mo $K\alpha$, 0.71073 Å
diffractometer	IPDS I
T_{min}, T_{max}	0.238, 0.940
θ range (°)	$1.96 \le \theta \le 25.66$
range of h; k; l	$-4 \le h \le 4$, $-4 \le k \le 4$, $-25 \le l \le 25$
number of measured reflections	3392
number of independent reflections	384
number of observed reflections	284
number of parameters	26
refinement	SHELXL97, full matrix least squares, against F^2
R_{int}	0.090
R_1	0.034
wR_2 ($I > 3\sigma$)	0.068
S (all I)	1.03
$\Delta\rho_{max}$, $\Delta\rho_{min}$ (e$^-$ Å^{-3})	2.52, –2.09
twin fractions	0.54, 0.46

Table 9.25: Wyckoff sites, atomic coordinates and coefficients U_{ij}* of the tensors of the anisotropic displacement parameter (Å^2) for $TbAgAs_2$

atom	site	x	y	z	U_{11}	U_{22}	U_{33}	U_{23}
Tb	4*c*	¼	0.2321(5)	0.1141(1)	0.008(2)	0.001(1)	0.0022(4)	0.0005(5)
Ag	4*c*	¼	0.7291(7)	0.2502(5)	0.011(3)	0.006(2)	0.0067(6)	0.001(1)
As1	4*c*	¼	0.2307(8)	0.3429(1)	0.001(4)	0.007(3)	0.0031(8)	–0.000(1)
As2	4*c*	¼	0.2307(8)	0.0016(5)	0.005(3)	0.007(2)	0.002(1)	–0.001(2)

* $U_{12} = U_{23} = 0$

Table 9.26: Selected interatomic distances (Å) of $TbAgAs_2$

Tb–As1 $^{i, ii}$	2.940(3)	Tb–Ag $^{i, ii}$	3.441(8)
Tb–As1 $^{iii, iv}$	2.932(3)	Ag–As1 $^{iii, iv}$	2.764(7)
Tb–As2	3.003(9)	Ag–As1	2.754(8)
Tb–As2 ^{v}	3.117(9)	Ag–As1 ^{viii}	2.763(8)
Tb–As2 $^{vi, vii}$	3.119(9)	Ag–Ag $^{i, ii, iii, iv}$	2.797(1)
Tb–Ag	3.440(9)	As2–As2 $^{vi, vii}$	2.582(4)
Tb–Ag ^{v}	3.453(8)		

symmetry codes: (i) = $-x+1$, $y+1/2$, $-z+1/2$, (ii) = $-x$, $y+1/2$, $-z+1/2$, (iii) = $-x$, $y-1/2$, $-z+1/2$, (iv) = $-y+1$, $y-1/2$, $-z+1/2$, (v) = x, $y-1$, z, (vi) = $-x$, $-y+1$, $-z$, (vii) = $-x+1$, $-y+1$, $-z$, (viii) = x, $y+1$, z

$PrAuAs_2$

Table 9.27: Crystallographic and refinement data of $PrAuAs_2$

chemical formula	$PrAuAs_2$
formula weight (g mole^{-1})	487.72
space group	*Pmca*
a (Å)	5.766(2)
b (Å)	5.757(2)
c (Å)	20.458(4)
V (Å^3)	679.1(2)
Z	8
ρ_x (g cm^{-3})	9.54
crystal size (mm^3)	0.144 × 0.128 × 0.018
radiation, λ	Mo *K*α, 0.71073 Å
diffractometer	IPDS I
T_{min}, T_{max}	0.041, 0.267
θ range (°)	$1.99 \le \theta \le 25.80$
range of *h*; *k*; *l*	$-7 \le h \le 7, -7 \le k \le 7, -25 \le l \le 25$
number of measured reflections	7130
number of independent reflections	787
number of observed reflections	604
number of parameters	45
refinement	SHELXL97, full matrix least squares, against F^2
R_{int}	0.053
R_1	0.031
wR_2 ($I > 3\sigma$)	0.077
S (all *I*)	1.10
$\Delta\rho_{max}$, $\Delta\rho_{min}$ (e$^-$ Å^{-3})	3.92, –2.05
twin fractions	0.41, 0.59

Table 9.28: Wyckoff sites and atomic coordinates for $PrAuAs_2$

atom	Wyckoff site	*x*	*y*	*z*
Pr1	4*d*	¼	0.5145(2)	0.6159(1)
Pr2	4*d*	¼	0.0158(2)	0.8797(4)
Au1	4*c*	½	0.2345(1)	¼
Au2	4*c*	½	0.7310(2)	¼
As1	4*d*	¼	0.5153(4)	0.8398(1)
As2	4*d*	¼	0.0156(4)	0.6616(1)
As3	8*e*	0.5302(2)	0.2218(2)	0.0009(2)

Table 9.29: Coefficients U_{ij} of the tensors of the anisotropic displacement parameter (Å^2) for $PrAuAs_2$

atom	U_{11}	U_{22}	U_{33}	U_{12}	U_{13}	U_{23}
Pr1	0.0028(9)	0.0024(8)	0.0029(7)	0	0	0.0004(5)
Pr2	0.0026(9)	0.0019(8)	0.0030(8)	0	0	0.0004(5)
Au1	0.014(1)	0.0121(7)	0.0105(8)	0	0.0003(4)	0
Au2	0.014(1)	0.0122(6)	0.0112(8)	0	0.0009(4)	0
As1	0.006(1)	0.004(1)	0.008(1)	0	0	0.0006(7)
As2	0.005(1)	0.004(1)	0.008(1)	0	0	0.0006(7)
As3	0.0052(7)	0.0046(6)	0.0040(7)	–0.0010(5)	–0.0015(9)	–0.0006(8)

Table 9.30: Selected interatomic distances (Å) of $PrAuAs_2$

Pr1–As2	3.020(3)
Pr1–As1 $^{i, ii}$	3.022(1)
Pr1–As2 ^{iii}	3.033(3)
Pr1–As3 $^{iv, v}$	3.187(3)
Pr1–As3 $^{vi, vii}$	3.233(3)
Pr1–Au2 $^{viii, ix}$	3.406(1)
Pr1–Au1 $^{viii, ix}$	3.419(1)
Pr2–As1	2.989(3)
Pr2–As1 ^{x}	2.995(3)
Pr2–As2 $^{i, ii}$	3.004(1)
Pr2–As3 $^{xi, xii}$	3.073(3)
Pr2–As3 $^{xiii, xiv}$	3.189(3)
Pr2–Au1 $^{xi, xii}$	3.346(1)
Pr2–Au2 $^{viii, ix}$	3.353(1)
Au1–As2 $^{xi, xv}$	2.724(2)
Au1–As1 $^{viii, xvi}$	2.743(2)
Au1–Au2	2.858(1)
Au1–Au1 $^{xvii, xviii}$	2.883(6)
Au1–Au2 ^{x}	2.899(1)
Au2–As1 $^{viii, xvi}$	2.731(2)
Au2–As2 $^{viii, xvi}$	2.734(2)
Au2–Au2 $^{xvii, xviii}$	2.883(6)
Au2–Au1 ^{iii}	2.899(1)
As3–As3 ^{xvii}	2.535(3)
As3–As3 ^{xix}	2.578(3)

symmetry codes: (i) = x+1/2, y, $-z$+3/2; (ii) = x–1/2, y, $-z$+3/2; (iii) = x, y+1, z; (iv) = x–1/2, y, $-z$+1/2; (v) = $-x$+1, y, $-z$+1/2; (vi) = $-x$+1/2, $-y$+1, z+1/2; (vii) = x, $-y$+1, z+1/2; (viii) = $-x$+1, $-y$+1, $-z$+1; (ix) = x–1/2, $-y$+1, $-z$+1; (x) = x, y–1, z; (xi) = $-x$+1, $-y$, $-z$+1; (xii) = x–1/2, $-y$, $-z$+1; (xiii) = x, y, z+1; (xiv) = $-x$+1/2, y, z+1; (xv) = $-x$+1/2, $-y$, z–1/2; (xvi) = $-x$+1/2, $-y$+1, z–1/2; (xvii) = $-x$+3/2, y, z; (xviii) = $-x$+1/2, y, z; (xix) = $-x$+1, $-y$, $-z$

$NdAuAs_2$

Table 9.31: Crystallographic and refinement data of $NdAuAs_2$

chemical formula	$NdAuAs_2$
formula weight (g mole^{-1})	491.05
space group	*Pnma*
a (Å)	4.058(1)
b (Å)	4.059(1)
c (Å)	20.435(4)
V (Å^3)	336.6(2)
Z	4
ρ_x (g cm^{-3})	9.69
crystal size (mm^3)	0.212 × 0.199 × 0.012
radiation, λ	Mo $K\alpha$, 0.71073 Å
diffractometer	IPDS I
T_{min}, T_{max}	0.013, 0.393
θ range (°)	$1.99 \le \theta \le 25.63$
range of h; k; l	$-4 \le h \le 4$, $-4 \le k \le 4$, $-24 \le l \le 24$
number of measured reflections	3453
number of independent reflections	373
number of observed reflections	346
number of parameters	24
refinement	SHELXL97, full matrix least squares, against F^2
R_{int}	0.079
R_1	0.034
wR_2 ($I > 3\sigma$)	0.087
S (all I)	1.07
$\Delta\rho_{max}$, $\Delta\rho_{min}$ (e$^-$ Å^{-3})	2.15, –2.68
twin fractions	0.52, 0.48

Table 9.32: Wyckoff sites, atomic coordinates and coefficients U_{ij}* of the tensors of the anisotropic displacement parameter (Å^2) for $NdAuAs_2$

atom	site	x	y	z	U_{11}	U_{22}	U_{33}	U_{23}
Nd	4*c*	¼	0.2279(3)	0.1177(1)	0.001(1)	0.003(1)	0.0047(7)	–0.0003(3)
Au	4*c*	¼	0.7253(2)	0.2504(2)	0.012(1)	0.0136(8)	0.0117(6)	0.0012(6)
As1	4*c*	¼	0.2276(3)	0.3400(1)		U_{iso} = 0.0029(5) **		
As2	4*c*	¼	0.7097(5)	0.0020(5)	0.012(1)	0.009(1)	0.004(1)	0.002(2)

* $U_{12} = U_{23} = 0$
** isotropic refinement

Table 9.33: Selected interatomic distances (Å) of $NdAuAs_2$

Nd–As1 [i, ii]	2.996(1)	Nd–Au [v]	3.393(4)
Nd–As1 [iii, iv]	2.998(1)	Au–As1	2.727(3)
Nd–As2	3.069(9)	Au–As1 [viii]	2.740(4)
Nd–As2 [v]	3.165(9)	Au–As1 [i, ii]	2.744(4)
Nd–As2 [vi, vii]	3.187(8)	Au–Au [i, ii, iii, iv]	2.870(1)
Nd–Au [iii, iv]	3.374(5)	As2–As2 [vi, vii]	2.650(3)
Nd–Au	3.381(4)		

symmetry codes: (i) = $-x+1, y+1/2, -z+1/2$, (ii) = $-x, y+1/2, -z+1/2$, (iii) = $-x, y-1/2, -z+1/2$, (iv) = $-y+1, y-1/2, -z+1/2$, (v) = $x, y-1, z$, (vi) = $-x, -y+1, -z$, (vii) = $-x+1, -y+1, -z$, (viii) = $x, y+1, z$

$SmAuAs_2$

Table 9.34: Crystallographic and refinement data of $SmAuAs_2$

chemical formula	$SmAuA_2$
formula weight (g mole^{-1})	497.16
space group	*Pnma*
a (Å)	4.019(1)
b (Å)	4.049(1)
c (Å)	20.331(4)
V (Å^3)	330.9(1)
Z	4
ρ_x (g cm^{-3})	9.98
crystal size (mm^3)	0.163 × 0.140 × 0.010
radiation, λ	Mo *K*α, 0.71073 Å
diffractometer	IPDS I
T_{min}, T_{max}	0.043, 0.796
θ range (°)	$2.00 \le \theta \le 25.76$
range of *h*; *k*; *l*	$-4 \le h \le 4$, $-4 \le k \le 4$, $-24 \le l \le 24$
number of measured reflections	3436
number of independent reflections	337
number of observed reflections	296
number of parameters	26
refinement	SHELXL97, full matrix least squares, against F^2
R_{int}	0.041
R_1	0.026
wR_2 ($I > 3\sigma$)	0.059
S (all *I*)	1.00
$\Delta\rho_{max}$, $\Delta\rho_{min}$ (e$^-$ Å^{-3})	1.71, –1.72

Table 9.35: Wyckoff sites, atomic coordinates and coefficients U_{ij}* of the tensors of the anisotropic displacement parameter (Å^2) for $SmAuAs_2$

atom	site	*x*	*y*	*z*	U_{11}	U_{22}	U_{33}	U_{23}
Sm	4*c*	¼	0.2272(2)	0.1175(1)	0.0079(5)	0.0027(4)	0.0055(4)	0.0001(2)
Au	4*c*	¼	0.7238(2)	0.2498(1)	0.0163(5)	0.0102(3)	0.0125(4)	–0.0001(2)
As1	4*c*	¼	0.2271(3)	0.3424(1)	0.0065(9)	0.0024(6)	0.0087(8)	0.0002(5)
As2	4*c*	¼	0.7061(3)	0.0013(1)	0.011(1)	0.0059(7)	0.0057(8)	–0.0012(5)

* $U_{12} = U_{23} = 0$

Table 9.36: Selected interatomic distances (Å) of $SmAuAs_2$

Sm–As1 [i, ii]	2.967(1)	Sm–Au [vii]	3.374(1)
Sm–As2	3.056(2)	Au–As1	2.754(2)
Sm–As1 [iii, iv]	2.967(1)	Au–As1 [iii, iv]	2.748(1)
Sm–As2 [v, vi]	3.154(1)	Au–Au [i, ii, iii, iv]	2.852(1)
Sm–As2 [vii]	3.167(3)	Au–As1 [viii]	2.774(2)
Sm–Au [i, ii]	3.364(1)	As2–As2 [v, vi]	2.613(2)
Sm–Au	3.358(1)		

symmetry codes: (i) = –*x*, *y*–1/2, –*z*+1/2, (ii) = –*x*+1, *y*–1/2, –*z*+1/2, (iii) = –*x*+1, *y*+1/2, –*z*+1/2, (iv) = –*x*, *y*+1/2, –*z*+1/2, (v) = –*x*, –*y*+1, –*z*, (vi) = –*x*+1, –*y*+1, –*z*, (vii) = *x*, *y*–1, *z*, (viii) = *x*, *y*+1, *y*

$GdCuAs_2$

Table 9.37: Crystallographic and refinement data of $GdCuAs_2$

chemical formula	$GdCuAs_2$
formula weight (g mole^{-1})	370.6
basic cell setting, super space group	monoclinic, $P12_1/m1(\alpha 0\gamma)00$ (No. 11.1)
a (Å)	3.904(1)
b (Å)	3.902(1)
C (Å)	9.908(2)
β (°)	90.05(3)
V (Å^3)	150.92(5)
Z	2
D_x (g cm^{-3})	8.1537
number of reflections for cell parameters	10083
θ range (°)	$3.01 \leq \theta \leq 33.53$
μ (mm^{-1})	50.253
temperature (K)	293(2)
crystal size (mm^3)	0.260 × 0.060 × 0.020
laue class	$2/m$
q	[0.035(6), 0, 0.479(5)]
diffractometer	Stoe IPDS II, graphite monochromator, Mo $K\alpha$
absorption correction method	analytical
T_{min}, T_{max}	0.128, 0.460
number of measured, independent and observed reflections	10072, 2080, 788
criterion for observed reflections	$I > 3\sigma(I)$
range of h; k; l; m	$-6 \leq h \leq 6$, $-5 \leq k \leq 6$, $-16 \leq l \leq 16$, $-1 \leq m \leq 1$
number of unique reflections (all / obs)	2056 / 764
number of main reflections (all / obs)	666 / 543
number of satellites (all / obs)	1390 / 221
R_{int}, R_σ	0.066, 0.016
refinement	JANA2000, full matrix least squares, against F^2
refined modulation wave	$1\cdot\mathbf{q}_1$
R_1, $wR_2(I > 3\sigma)$; R_1, wR_2 (overall)	0.039, 0.072, 0.097, 0.079
R_1, $wR_2(I > 3\sigma)$; R_1, wR_2 (all I) (main reflections)	0.033, 0.065, 0.040, 0.066
R_1, $wR_2(I > 3\sigma)$; R_1, wR_2, (all I) (satellites)	0.093, 0.190, 0.265, 0.237
S (all I)	1.25
number of reflections	2043
number of parameters	77
weighting scheme	$w = 1 / [\sigma^2(I) + 0.0004(I^2)]$
$\Delta\rho_{max}$, $\Delta\rho_{min}$ (e$^-$ Å^{-3})	1.32, –1.68
extinction method	B–C type 1 Gaussian isotropic [94]
extinction coefficient	0.144

Table 9.38: Wyckoff positions, atomic coordinates and coefficients U_{ii}* of the tensors of the anisotropic displacement parameters (Å^2) for $GdCuAs_2$ in the average structure in *Pmmn*

atom	Wyckoff site	*x*	*y*	*z*	U_{11}	U_{22}	U_{33}
Gd	2*a*	¼	¼	0.2385(1)	0.0133(2)	0.0106(3)	0.0182(2)
Cu	2*b*	¼	¾	0.4995(3)	0.0159(5)	0.0115(6)	0.0207(5)
As1	2*a*	¼	¼	0.6585(1)	0.0120(4)	0.0099(5)	0.0205(4)
As2	2*b*	¼	¾	–0.0048(2)	0.0325(6)	0.0089(5)	0.0174(4)

* $U_{12} = U_{13} = U_{23} = 0$

Table 9.39: Wyckoff positions and atomic coordinates of $GdCuAs_2$ in superspace group $P12_1/m1(\alpha 0 \gamma)00$

atom	Wyckoff site	occupation	*x*	*y*	*z*
Gd	2*e*	1	0.2475(3)	¼	0.23850(4)
Cu	2*e*	1	0.258(2)	¾	0.5001(2)
As1	2*e*	1	0.2541(8)	¼	0.65820(8)
As2	2*e*	1	–0.742(2)	¾	–0.0005(2)

Table 9.40: Isotropic displacement parameters (Å^2) and Fourier coefficients* of the modulation wave of $GdCuAs_2$ in superspace group $P12_1/m1(\alpha 0 \gamma)00$

atom	U_{iso}	*xsin*1	*zsin*1	*xcos*1	*zcos*1
Gd	0.0129(1)	0.0070(3)	0.0000(3)	0.0075(3)	0.0002(3)
Cu	0.0157(3)	0.0127(8)	0.0034(8)	–0.0002(7)	0.0000(7)
As1	0.0133(2)	0.0098(4)	0.0001(6)	–0.0053(4)	0.0000(6)
As2	0.0175(3)	0.0004(7)	–0.0003(7)	–0.0241(7)	0.0035(5)

* *xsin*1, *xcos*1, *zsin*1 and *zcos*1 correspond to atomic displacement waves along *x* and *z*, respectively.

Table 9.41: Selected interatomic distances (Å) of $GdCuAs_2$

	ave.	min.	max.
Gd–As1 $^{i, ii}$	2.948(4)	2.944(4)	2.952(4)
Gd–As1 $^{iii, iv}$	2.939(3)	2.936(3)	2.942(3)
Gd–As2 ^{v}	3.051(7)	2.988(6)	3.113(6)
Cu–Cu $^{ii, vi}$	2.806(5)	2.803(5)	2.809(5)
Cu–Cu $^{iv, vii}$	2.714(5)	2.709(5)	2.719(5)
Cu–As1	2.502(6)	2.482(6)	2.523(7)
Cu–As1 ^{viii}	2.502(6)	2.482(6)	2.523(7)
Cu–As1 ^{ii}	2.541(8)	2.515(8)	2.566(8)
Cu–As1 ^{iv}	2.468(8)	2.451(8)	2.484(8)
As2–As2 $^{ix, x}$	2.802(5)	2.671(5)	2.940(5)
As2–As2 $^{xi, xii}$	2.722(5)	2.593(5)	2.853(5)

symmetry codes: (i) = –*x*, –*y*, 1–*z*; (ii) = –*x*, 1–*y*, 1–*z*; (iii) = 1–*x*, –*y*, 1–*z*; (iv) = 1–*x*, 1–*y*, 1–*z*; (v) = –*x* ,–*y*, –*z*; (vi) = –*x*, 2–*y*, 1–*z*; (vii) = 1–*x*, 2–*y*, 1–*z*; (viii) = *x*, 1+*y*, +*z*; (ix) = –2–*x*, –1–*y*, –*z*; (x) = –2–*x*, –*y*, –*z*; (xi) = –1–*x*, –1–*y*, –*z*; (xii) = –1–*x*, –*y*, –*z*

$CeAuAs_2$

Table 9.42: Crystallographic and refinement data of $CeAuAs_2$

chemical formula	$CeAu_{0.986(2)}As_2$
formula weight (g mole^{-1})	484.2
basic cell setting, super space group	monoclinic, $P12_1/m1(\alpha 0\gamma)00$ (No. 11.1)
a (Å)	5.804(1)
b (Å)	5.814(1)
c (Å)	10.179(1)
β (°)	90.09(8)
V (Å^3)	343.5(1)
Z	4
D_x (g cm^{-3})	9.41
number of reflections for cell parameters	7206
θ range (°)	$2.79 \leq \theta \leq 33.48$
μ (mm^{-1})	74.55
temperature (K)	293(2)
crystal size (mm^3)	0.139 × 0.137 × 0.004
laue class	$2/m$
q	[0.08(1), 0, 0.39(1)]
diffractometer	Stoe IPDS II, graphite monochromator, Mo $K\alpha$
absorption correction method	analytical
T_{min}, T_{max}	0.015, 0.306
number of measured, independent and observed reflections	20909, 4314, 1523
criterion for observed reflections	$I > 3\sigma(I)$
range of h; k; l; m	$-9 \leq h \leq 9$, $-8 \leq k \leq 8$, $-16 \leq l \leq 14$, $-1 \leq m \leq 1$
number of unique reflections (all / obs)	4210, 1422
number of main reflections (all / obs)	1342, 1044
number of satellites (all / obs)	2868, 378
R_{int}, R_σ	0.0681, 0.0190
refinement	JANA2000, full matrix least squares, against F^2
refined modulation wave	$1\cdot\mathbf{q}$
R_1, $wR_2(I > 3\sigma)$; R_1, wR_2 (overall)	0.0349, 0.0747, 0.0905, 0.0813
R_1, $wR_2(I > 3\sigma)$; R_1, wR_2 (all I) (main reflections)	0.0297, 0.0645, 0.0383, 0.0655
R_1, $wR_2(I > 3\sigma)$; R_1, wR_2, (all I) (satellites)	0.0962, 0.1969, 0.3276, 0.2411
S (all I)	1.29
number of reflections	4210
number of parameters	131
weighting scheme	$w = 1 / [\sigma^2(I) + 0.0004(I^2)]$
$\Delta\rho_{max}$, $\Delta\rho_{min}$ (e$^-$ Å^{-3})	4.03, –3.66
extinction method	B–C type 1 Gaussian isotropic [94]
extinction coefficient	0.55(2)

Table 9.43: Wyckoff positions, atomic coordinates and coefficients U_{ii}* of the tensors of the anisotropic displacement parameters (Å^2) for $CeAuAs_2$ in the average structure in *Cmme*

atom	Wyckoff site	*x*	*y*	*z*	U_{11}	U_{22}	U_{33}
Ce	4*g*	0	¼	0.2350(1)	0.0105(4)	0.0139(7)	0.0136(7)
Au	4*b*	¼	0	½	0.0179(4)	0.0213(5)	0.0163(4)
As1	4*a*	0	¼	0.6788(2)	0.0112(7)	0.014(1)	0.014(1)
As3	4*g*	¼	0	0	0.040(1)	0.047(2)	0.009(1)

* $U_{12} = U_{13} = U_{23} = 0$

Table 9.44: Wyckoff positions, atomic coordinates and isotropic displacement parameters (Å^2) of $CeAuAs_2$ in superspace group $P12_1/m1(\alpha 0 \gamma)00$

atom	Wyckoff site	*x*	*y*	*z*	U_{iso}
Ce1	2*e*	0.4999(4)	¼	0.75979(4)	0.0122(1)
Ce2	2*e*	0.0005(4)	¼	0.23007(4)	0.0128(1)
Au	4*f*	0.24823(4)	–0.0005(2)	0.4995(1)	0.0188(7)
As1	2*e*	0.5005(6)	¼	0.3220(1)	0.0142(2)
As2	2*e*	–0.0021(6)	¼	0.6805(1)	0.0144(2)
As3	4*f*	0.2789(1)	–0.0033(6)	0.0002(3)	0.0209(2)

Table 9.45: Fourier coefficients* of the modulation wave of $CeAuAs_2$ in superspace group $P12_1/m1(\alpha 0 \gamma)00$

atom	*xsin*1	*ysin*1	*zsin*1	*xcos*1	*ycos*1	*zcos*1
Ce1	0.0057(3)	0	–0.0006(3)	–0.0043(3)	0	0.0002(2)
Ce2	0.0051(3)	0	0.000(2)	0.0039(3)	0	–0.0002(3)
Au	0.0076(1)	–0.0006(2)	–0.0001(1)	0.0003(3)	0.00014(6)	0.0001(2)
As1	0.0059(5)	0	–0.0016(5)	0.0033(5)	0	–0.0015(5)
As2	0.0062(5)	0	–0.0020(5)	–0.0029(5)	0	0.0011(5)
As3	0.0041(3)	–0.0010(6)	0.0001(3)	–0.0030(9)	–0.0140(2)	0.0004(3)

	o	*osin*1	*ocos*1
Au	0.986(2)	–0.022(6)	–0.031(4)

* *x*, *y*, *z* correspond to atomic displacement wave, *o* to the occupancy modulation wave

Table 9.46: Selected interatomic distances (Å) of $CeAuAs_2$

	ave.	min.	max.
Ce1 – As2 [i]	3.002(5)	2.975(5)	3.029(5)
Au1 – Au1 [ii]	2.882(2)	2.867(3)	2.896(3)
Au1 – Au1 [iii]	2.923(2)	2.915(3)	2.930(3)
Au1 – Au1 [iv]	2.901(2)	2.894(2)	2.908(2)
Au1 – Au1 [v]	2.913(2)	2.906(2)	2.920(2)
Au1 – As1	2.746(4)	2.713(5)	2.777(5)
Au1 – As1 [iii]	2.743(4)	2.726(4)	2.761(4)
Au1 – As2	2.764(4)	2.731(5)	2.796(5)
Au1 – As2 [ii]	2.737(4)	2.721(4)	2.753(4)
As3 – As3 [vi]	2.569(5)	2.529(7)	2.614(7)
As3 – As3 [iv]	2.866(6)	2.705(5)	3.031(5)
As3 – As3 [v]	2.947(6)	2.783(5)	3.109(5)

symmetry codes: (i) = 1+*x*, *y*, *z*; (ii) = –*x*, –*y*, 1–*z*; (iii) = 1–*x*, –*y*, 1–*z*; (iv) = *x*, –½–*y*, *z*; (v) = *x*, ½–*y*, *z*, (vi) = 1–*x*, –*y*, –*z*

Table 9.47: Distances (Å) in and between the As3 chains in different blocks of $CeAuAs_2$

	rectangles	four chains	five chains	six chains	seven chains
a_b	2.557 – 2.562	2.535 – 2.545	2.534 – 2.553	2.582 – 2.618	2.572 – 2.620
b_b	2.854 – 2.895	2.778 – 2.851	2.779 – 2.888	2.702 – 2.855	2.704 – 2.896
a_{nb}	– (one "chain")	3.269 – 3.275	3.264 – 3.274	3.221 – 3.232	3.222 – 3.237
b_{bc}	2.910 – 2.950	2.953 – 3.027	2.917 – 3.026	2.972 – 3.102	2.909 – 3.101

with *a* and *b* crystallographic directions (*b* in propagation direction of the chains), indices *b* = bonding, *nb* = non bonding, *bc* = between chains.

$GdAuAs_2$

Table 9.48: Crystallographic and refinement data of $GdAuAs_2$

chemical formula	$GdAu_{0.973(3)}As_2$
formula weight (g mole^{-1})	498.7
basic cell setting, super space group	monoclinic, $P12_1/m1(\alpha 0\gamma)00$ (No. 11.1)
a (Å)	3.957(1)
b (Å)	4.060(2)
c (Å)	10.135(2)
β (°)	90.01(3)
V (Å^3)	162.82(9)
Z	2
D_x (g cm^{-3})	10.278
number of reflections for cell parameters	6594
θ range (°)	$3.01 \leq \theta \leq 33.53$
μ (mm^{-1})	85.05
temperature (K)	293(2)
crystal size (mm^3)	0.305 × 0.0587 × 0.0025
laue class	$2/m$
q	[0.03(1), 0, 0.48(1)]
diffractometer	Stoe IPDS II, graphite monochromator, Mo $K\alpha$
absorption correction method	analytical
T_{min}, T_{max}	0.064, 0.807
number of measured, independent and observed reflections	9508, 2450, 1655
criterion for observed reflections	$I > 3\sigma(I)$
range of h; k; l; m	$-6 \leq h \leq 5$, $-6 \leq k \leq 6$, $-16 \leq l \leq 13$, $-1 \leq m \leq 1$
number of unique reflections (all / obs)	2434 / 1640
number of main reflections (all / obs)	1118 / 1039
number of satellites (all / obs)	1316 / 601
R_{int}, R_σ	0.077, 0.02
refinement	JANA2000, full matrix least squares, against F^2
refined modulation wave	$1\cdot\mathbf{q}_1$
R_1, $wR_2(I > 3\sigma)$; R_1, wR_2 (overall)	0.046, 0.103, 0.066, 0.106
R_1, $wR_2(I > 3\sigma)$; R_1, wR_2 (all I) (main reflections)	0.035, 0.079, 0.038, 0.079
R_1, $wR_2(I > 3\sigma)$; R_1, wR_2, (all I) (satellites)	0.107, 0.211, 0.179, 0.222
S (all I)	2.49
number of reflections	2428
number of parameters	80
weighting scheme	$w = 1 / [\sigma^2(I) + 0.0004(I^2)]$
$\Delta\rho_{max}$, $\Delta\rho_{min}$ (e$^-$ Å^{-3})	2.25, –2.50
extinction method	B–C type 1 Gaussian isotropic [94]
extinction coefficient	0.206

Table 9.49: Wyckoff positions, atomic coordinates and coefficients U_{ii}* of the tensors of the anisotropic displacement parameters (Å^2) for $GdAuAs_2$ in the average structure in *Pmmn*

atom	Wyckoff site	*x*	*y*	*z*	U_{11}	U_{22}	U_{33}
Gd	2*a*	¼	¼	0.2337(1)	0.0031(3)	0.0133(5)	0.0070(2)
Au	2*b*	¼	¾	0.4994(2)	0.0115(3)	0.0197(4)	0.0136(2)
As1	2*a*	¼	¼	0.6872(1)	0.0030(6)	0.0116(8)	0.0105(5)
As2	2*b*	¼	¾	0.0026(5)	0.0071(8)	0.038(1)	0.0054(6)

* $U_{12} = U_{13} = U_{23} = 0$

Table 9.50: Wyckoff positions and atomic coordinates of $GdAuAs_2$ in superspace group $P12_1/m1(\alpha 0 \gamma)00$

atom	Wyckoff site	occup.	*x*	*y*	*z*
Gd	2*e*	1	0.2484(4)	¼	0.23384(6)
Au	2*e*	0.973(3)	0.2495(4)	¾	0.5005(3)
As1	2*e*	1	0.243(2)	¼	0.6876(2)
As2	2*e*	1	0.251(2)	¾	–0.0018(6)

Table 9.51: Isotropic displacement parameters (Å^2) and Fourier coefficients* of the modulation wave of $GdAuAs_2$ in superspace group $P12_1/m1(\alpha 0 \gamma)00$

atom	U_{iso}	*xsin*1	*zsin*1	*xcos*1	*zcos*1
Gd	0.0128(3)	0.0113(4)	–0.0008(4)	–0.0127(4)	–0.0006(4)
Au	0.0197(3)	0.0213(3)	–0.0019(4)	–0.0001(4)	0.0004(3)
As1	0.0137(7)	0.0142(7)	–0.0013(9)	–0.0091(7)	0.0002(8)
As2	0.0187(7)	0.0003(9)	–0.0002(7)	–0.038(1)	0.002(2)

* *xsin*1, *xcos*1, *zsin*1 and *zcos*1 correspond to atomic displacement waves along *x* and *z*, respectively.

Table 9.52: Selected interatomic distances (Å) of $GdAuAs_2$

	ave.	min.	max.
Gd–As1 [i, ii]	2.923(5)	2.916(5)	2.930(5)
Gd–As1 [iii, iv]	2.966(5)	2.963(5)	2.970(5)
Au–Au [ii, v]	2.832(2)	2.826(2)	2.837(2)
Au–Au [iv, vi]	2.838(2)	2.832(2)	2.843(2)
Au–As1	2.777(7)	2.769(6)	2.785(7)
Au–As1 [vii]	2.777(7)	2.769(6)	2.785(7)
Au–As1 [ii]	2.727(8)	2.718(8)	2.735(8)
Au–As1 [iv]	2.768(8)	2.750(9)	2.787(9)
As2–As2 [viii, ix]	2.843(6)	2.641(5)	3.057(6)
As2–As2 [x, xi]	2.835(6)	2.631(5)	3.043(6)

symmetry codes: (i) = –*x*, –*y*, 1–*z*; (ii) = –*x*, 1–*y*, 1–*z*; (iii) = 1–*x*, –*y*, 1–*z*; (iv) = 1–*x*, 1–*y*, 1–*z*; (v) = –*x*, 2–*y*, 1–*z*; (vi) = 1–*x*, 2–*y*, 1–*z*; (vii) = *x*, 1+*y*, +*z*; (viii) = –*x*, 1–*y*, –*z*; (ix) = –*x*, 2–*y*, –*z*; (x) = 1–*x*, 1–*y*, –*z*, (xi) = 1–*x*, 2–*y*, –*z*

$TbAuAs_2$

Table 9.53: Crystallographic and refinement data of $TbAuAs_2$

chemical formula	$TbAu_{0.966(6)}As_2$
formula weight (g mole^{-1})	499.0
basic cell setting, super space group	monoclinic, $P12_1/m1(\alpha 0\gamma)00$ (No. 11.1)
a (Å)	3.993(1)
b (Å)	3.986(1)
c (Å)	10.080(2)
β (°)	90.0(3)
V (Å^3)	160.43(12)
Z	2
D_x (g cm^{-3})	10.300
number of reflections for cell parameters	7354
θ range (°)	$2.95 \leq \theta \leq 33.42$
μ (mm^{-1})	87.56
temperature (K)	293(2)
crystal size (mm^3)	$0.126 \times 0.120 \times 0.011$
laue class	$2/m$
q	[0.02(1), 0, 0.46(1)]
diffractometer	Stoe IPDS II, graphite monochromator, Mo $K\alpha$
absorption correction method	analytical
T_{min}, T_{max}	0.066, 0.892
number of measured, independent and observed reflections	9845, 2101, 1091
criterion for observed reflections	$I > 3\sigma(I)$
range of h; k; l; m	$-5 \leq h \leq 6$, $-5 \leq h \leq 6$, $-16 \leq l \leq 16$, $-1 \leq m \leq 1$
number of unique reflections (all / obs)	2092 / 1083
number of main reflections (all / obs)	686 / 642
number of satellites (all / obs)	1406 / 441
R_{int}, R_σ	0.059, 0.013
refinement	JANA2000, full matrix least squares, against F^2
refined modulation wave	$1\cdot\mathbf{q}_1$
R_1, $wR_2(I > 3\sigma)$; R_1, wR_2 (overall)	0.057, 0.131, 0.087, 0.135
R_1, $wR_2(I > 3\sigma)$; R_1, wR_2 (all I) (main reflections)	0.051, 0.125, 0.053, 0.126
R_1, $wR_2(I > 3\sigma)$; R_1, wR_2, (all I) (satellites)	0.099, 0.207, 0.223, 0.250
S (all I)	3.04
number of reflections	2087
number of parameters	80
weighting scheme	$w = 1 / [\sigma^2(I) + 0.0001(I^2)]$
$\Delta\rho_{max}$, $\Delta\rho_{min}$ (e$^-$ Å^{-3})	2.99, –2.87
extinction method	B–C type 1 Gaussian isotropic [94]
extinction coefficient	0.798

Table 9.54: Wyckoff positions, atomic coordinates and coefficients U_{ii}* of the tensors of the anisotropic displacement parameters (Å^2) for $TbAuAs_2$ in the average structure in *Pmmn*

atom	Wyckoff site	*x*	*y*	*z*	U_{11}	U_{22}	U_{33}
Tb	2*a*	¼	¼	0.2328(2)	0.014(4)	0.009(4)	0.0065(7)
Au	2*b*	¼	¾	0.502(1)	0.018(2)	0.023(3)	0.0135(9)
As1	2*a*	¼	¼	0.6887(3)	0.021(6)	0.002(5)	0.008(1)
As2	2*b*	¼	¾	–0.002(1)	0.045(7)	0.002(6)	0.004(2)

* $U_{12} = U_{13} = U_{23} = 0$

Table 9.55: Wyckoff positions and atomic coordinates of $TbAuAs_2$ in superspace group $P12_1/m1(\alpha 0 \gamma)00$

atom	Wyckoff site	occup.	*x*	*y*	*z*
Tb	2*e*	1	0.2519(9)	¼	0.23312(7)
Au	2*e*	0.966(6)	0.249(2)	¾	0.5006(2)
As1	2*e*	1	0.236(2)	¼	0.6899(2)
As2	2*e*	1	0.252(3)	¾	–0.0016(4)

Table 9.56: Isotropic displacement parameters (Å^2) and Fourier coefficients* of the modulation wave of $TbAuAs_2$ in superspace group $P12_1/m1(\alpha 0 \gamma)00$

atom	U_{iso}	*xsin*1	*zsin*1	*xcos*1	*zcos*1
Tb	0.0186(3)	0.0063(6)	–0.0001(4)	0.0066(5)	0.0001(4)
Au	0.0266(3)	0.0119(4)	–0.0003(3)	0.0001(5)	0.0000(6)
As1	0.0185(6)	0.008(2)	0.0024(8)	–0.005(2)	–0.0015(8)
As2	0.0250(8)	0.000(2)	–0.0005(8)	–0.020(2)	–0.001(2)

* *xsin*1, *xcos*1, *zsin*1 and *zcos*1 correspond to atomic displacement waves along *x* and *z*, respectively.

Table 9.57: Selected interatomic distances (Å) of $TbAuAs_2$

	ave.	min.	max.
Tb–As1 $^{i, ii}$	2.909(6)	2.902(6)	2.917(6)
Tb–As1 $^{iii, iv}$	2.976(6)	2.968(6)	2.983(6)
Au–Au $^{ii, v}$	2.829(5)	2.826(5)	2.832(5)
Au–Au $^{iv, vi}$	2.845(5)	2.843(5)	2.846(5)
Au–As1	2.805(7)	2.782(6)	2.827(6)
Au–As1 ^{vii}	2.805(7)	2.782(6)	2.827(6)
Au–As1 ^{ii}	2.71(2)	2.697(9)	2.728(9)
Au–As1 ^{iv}	2.80(2)	2.772(9)	2.832(9)
As2–As2 $^{viii, ix}$	2.85(2)	2.74(2)	2.96(2)
As2–As2 $^{x, xi}$	2.83(2)	2.72(2)	2.94(2)

symmetry codes: (i) = –*x*, –*y*, 1–*z*; (ii) = –*x*, 1–*y*, 1–*z*; (iii) = 1–*x*, –*y*, 1–*z*; (iv) = 1–*x*, 1–*y*, 1–*z*; (v) = –*x*, 2–*y*, 1–*z*; (vi) = 1–*x*, 2–*y*, 1–*z*; (vii) = *x*, 1+*y*, +*z*; (viii) = –*x*, 1–*y*, –*z*; (ix) = –*x*, 2–*y*, –*z*; (x) = 1–*x*, 1–*y*, –*z*, (xi) = 1–*x*, 2–*y*, –*z*

10 Acknowledgements

I am deeply indebted to Prof. Michael Ruck for entrusting me with this interesting and fruitful topic, his support and encouragement, suggestions and discussion.
I would like to express my gratitude to PD Thomas Doert for his continuous assistance, support, guidance and discussion.
I am thankful to my collaborators Volker Neu (IFW Dresden) for carrying out the magnetization experiments and their discussion, Mathias Dörr (Solid State Physics, TU Dresden) who was measuring the conductivity and Helge Rosner (MPI CPfS) who carried out the band structure calculations.
Jutta Krug and Gudrun Kadner are gratefully acknowledged for their continuous experimental support.
Mstr. Kehse is thanked for providing the quartz ampoules.
I thank Anja Bensch for measuring the X-ray powder diffractograms.
I acknowledge Peter Höhn (MPI CPfS) for providing equipment to produce pellets for conductivity measurements.
Gerlind Klemmt and Ilona Salzmann are thanked for administrative support.
I finally express my appreciation to my former colleagues PD Peer Schmidt, Christian Bartsch, Alexander Gerisch, Josch Getzschmann, Christian Graf, Andreas Heerwig, Daniel Köhler, Fabian Nitsche, Frauke Philipp, Bernhard Wahl and the other previous members of AK Ruck.

This work was part of Sonderforschungsbereich (SFB) 463 and founded by the Deutsche Forschungsgemeinschaft.

Versicherung

Hiermit versichere ich, daß ich die vorliegende Arbeit ohne unzulässige Hilfe Dritter und ohne Benutzung anderer als der angegebenen Hilfsmittel angefertigt habe; die aus fremden Quellen direkt oder indirekt übernommenen Gedanken sind als solche kenntlich gemacht. Die Arbeit wurde bisher weder im Inland noch im Ausland in gleicher oder ähnlicher Form einer anderen Prüfungsbehörde vorgelegt.

Die vorliegende Arbeit wurde am Institut für Anorganische Chemie der Technischen Universität Dresden unter wissenschaftlicher Betreuung von Herrn Prof. Dr. M. Ruck im Zeitraum von Dezember 2005 bis Juni 2009 angefertigt.
Es haben keine früheren erfolglosen Promotionsverfahren stattgefunden. Hiermit erkenne ich die Promotionsordnung der Fakultät Mathematik und Naturwissenschaften der Technischen Universität Dresden vom 17.07.2008 an.

Dresden, den 31. März 2009 Dieter Rutzinger